Quantifying the suppression of the (un)-obscured star formation in galaxy cluster cores at $0.2 \lesssim z \lesssim 0.9$

L. Rodríguez-Muñoz[1]⋆, G. Rodighiero[1], C. Mancini[1], P. G. Pérez-González[2,3],
T. D. Rawle[4], E. Egami[5], A. Mercurio[6], P. Rosati[7], A. Puglisi[1,8],
A. Franceschini[1], I. Balestra[9], I. Baronchelli[1,10], A. Biviano[11], H. Ebeling[12],
A. C. Edge[13], A. F. M. Enia[1], C. Grillo[14,15], C. P. Haines[16], E. Iani[1],
T. Jones[17,18], M. Nonino[11], I. Valtchanov[19], B. Vulcani[1], M. Zemcov[20]

[1] *Dipartimento di Fisica e Astronomia "G. Galilei", Università degli Studi di Padova, Vicolo dell'Osservatorio 3, I-35122, Italy*
[2] *Departamento de Astronomía y Astrofísica, Universidad Complutense de Madrid, Av. Complutense s/n, C.P. 28040, Madrid, Spain*
[3] *Centro de Astrobiología, Instituto Nacional de Técnica Aeroespacial, Carretera de Ajalvir km 4, Torrejón de Ardoz, Madrid, E-28850, Spain*
[4] *ESA/Space Telescope Science Institute (STScI), 3700 San Martin Drive, Baltimore, MD 21218, USA*
[5] *Steward Observatory, University of Arizona, 933 N. Cherry Ave, Tucson, AZ 85721, USA*
[6] *INAF-Osservatorio Astronomico di Capodimonte, via Moiariello 16, 80131 Napoli, Italy*
[7] *Dipartimento di Fisica e Scienze della Terra, Università degli Studi di Ferrara, via Saragat 1, 44122 Ferrara, Italy*
[8] *Laboratoire AIM-Paris-Saclay, CEA/DSM-CNRS-Université Paris Diderot, IRFU/Service d'Astrophysique, CEA Saclay,*
Orme des Merisiers, F-91191 Gif-sur-Yvette, France
[9] *University Observatory Munich, Scheinerstrasse 1, D-81679 Munich, Germany*
[10] *IPAC, Mail Code 314-6, Caltech, 1200 E. California Blvd., Pasadena, CA 91125, USA*
[11] *INAF-Osservatorio Astronomico di Trieste, via G. B. Tiepolo 11, I-34131, Trieste, Italy*
[12] *Institute for Astronomy, University of Hawaii, Honolulu, HI 96822, USA*
[13] *Centre for Extragalactic Astronomy, Department of Physics, Durham University, South Road, Durham DH1 3LE, UK*
[14] *Dark Cosmology Centre, Niels Bohr Institute, University of Copenhagen, Juliane Maries Vej 30, DK-2100 Copenhagen, Denmark*
[15] *Dipartimento di Fisica, Universita degli Studi di Milano, via Celoria 16, I-20133 Milano, Italy*
[16] *INAF - Osservatorio Astronomico di Brera, via Brera 28, I-20121 Milano, Italy*
[17] *Department of Physics and Astronomy, PAB, 430 Portola Plaza, Box 951547, Los Angeles, CA 90095-1547, USA*
[18] *Department of Physics, University of California Davis, 1 Shields Avenue, Davis, CA 95616, USA*
[19] *Herschel Science Centre, European Space Astronomy Centre, ESA, E-28691 Villanueva de la Cañada, Spain*
[20] *Center for Detectors, School of Physics and Astronomy, Rochester Institute of Technology, Rochester NY 14623, USA*

ABSTRACT

We quantify the star formation (SF) in the inner cores ($\mathcal{R}/R_{200} \leq 0.3$) of 24 massive galaxy clusters at $0.2 \lesssim z \lesssim 0.9$ observed by the *Herschel* Lensing Survey and the Cluster Lensing and Supernova survey with *Hubble*. These programmes, covering the rest-frame ultraviolet to far-infrared regimes, allow us to accurately characterize stellar mass-limited ($\mathcal{M}_* > 10^{10}\,M_\odot$) samples of star-forming cluster members (not)-detected in the mid- and/or far-infrared. We release the catalogues with the photometry, photometric redshifts, and physical properties of these samples. We also quantify the SF displayed by comparable field samples from the Cosmic Assembly Near-infrared Deep Extragalactic Legacy Survey. We find that in intermediate-z cluster cores, the SF activity is suppressed with respect the field in terms of both the fraction ($\mathcal{F}$) of star-forming galaxies (SFG) and the rate at which they form stars ($\mathcal{SFR}$ and $s\mathcal{SFR} = \mathcal{SFR}/\mathcal{M}_*$). On average, the $\mathcal{F}$ of SFGs is a factor ~ 2 smaller in cluster cores than in the field. Furthermore, SFGs present average $\mathcal{SFR}$ and $s\mathcal{SFR}$ typically ~ 0.3 dex smaller in the clusters than in the field along the whole redshift range probed. Our results favour long time-scale quenching physical processes as the main driver of SF suppression in the inner cores of clusters since $z \sim 0.9$, with shorter time-scale processes being very likely responsible for a fraction of the missing SFG population.

Key words: galaxies: clusters: general – galaxies: evolution – galaxies: star formation – catalogues

arXiv:1812.08804v1 [astro-ph.GA] 20 Dec 2018

1 INTRODUCTION

Galaxies appear to be distributed into two fairly distinct general groups (e.g., Kauffmann et al. 2003, Bell et al. 2004, Baldry et al. 2004, Haines et al. 2017): a population of relatively red, quiescent galaxies (i.e., where the star formation activity has already been quenched), which are characterized by spheroid-dominated morphologies; and a population of rather blue, star-forming galaxies (SFGs), with disk-dominated morphologies. Understanding the nature of the processes that make a galaxy a member of either category at any cosmological epoch is one of the longest standing unsolved problems in astrophysics.

The fraction of red/quiescent/early-type galaxies among the whole population scales with the stellar mass ($\mathcal{M}_*$) of the galaxies up to $z\sim4$ (e.g., Baldry et al. 2004, 2006), and with the density of the environments they inhabit at least up to $z\sim1$ (e.g., Dressler 1980, Lewis et al. 2002). Hence, different works have claimed that this *dichotomy* between (still) star-forming and quenched galaxies, should be driven (independently; Peng et al. 2010) by the impact on the evolution of galaxies of two kind of processes: those somehow related to the stellar mass of the galaxies they quench, and therefore, responsible for the so-called *mass quenching*; and those linked to physical processes taking place in high density environments, responsible for the so-called *environmental quenching*. The physical nature of these quenching processes and its evolution with redshift remains controversial.

A plethora of works have studied the star formation (SF) activity within galaxy clusters at different redshifts as to quantify the environmental influence on galaxy evolution (e.g., Dressler et al. 1997, Poggianti et al. 1999; Poggianti 2003, De Lucia et al. 2007, Saintonge et al. 2008, Finn et al. 2010, Vulcani et al. 2011). This large body of work gives evidence for a significant transformation of galaxy populations in clusters since z~1. Already three decades ago, Butcher & Oemler (1984, see also Butcher & Oemler 1978) found that the fraction of blue cluster members increases from zero in the local universe to ∼20% by z~0.4. This rapid evolution over the last 5 billion years can only be explained by the existence of a population of field SFGs entering the cluster environment, which eventually is capable of turning them into passively evolving systems. This scenario is also favoured by the standard hierarchical cosmological model, which predicts a peak in the rate of field galaxies entering the cluster environment at z~0.4 (Kauffmann 1995).

In clusters, SFGs are not only less numerous than in the field, but they seem to present also different properties with respect their isolated counterparts. For instance, rich environments host a high fraction of *post-starburst* (PSB; e.g., Poggianti et al. 2009, Muzzin et al. 2014, Paccagnella et al. 2017), and *jellyfish* galaxies (e.g., Smith et al. 2010, Poggianti et al. 2017). Also, first CO observations in z~0.4-0.5 by Jablonka et al. (2013) show that cluster members contain less molecular gas than field galaxies at the same redshift.

Works such as Patel et al. (2009), Vulcani et al. (2010), Haines et al. (2013), or Paccagnella et al. (2016) find a different distribution of star formation rate (SFR), and specific star formation rate ($s\mathcal{SFR}$; defined as the ratio between the $\mathcal{SFR}$ and the $\mathcal{M}_*$ of a galaxy) in the inner regions of clusters (i.e., within the virial radius, $\mathcal{R}_{\mathrm{virial}}$) with respect to the field, with values typically ∼0.2-0.3 dex smaller for the former. This offset translates into a shift in the tight relation between the $\mathcal{SFR}$ and $\mathcal{M}_*$ found for the star-forming field galaxies up to $z\sim4$ (e.g, Noeske et al. 2007, Rodighiero et al. 2011, Whitaker et al. 2012b, Schreiber et al. 2017). Such a correlation is commonly known as the *main sequence* (MS) of SFGs. The existence of the MS is interpreted as the proof for a typical mode in which the galaxies form stars (e.g., Renzini & Peng 2015). The tightness of the correlation (0.3 dex scatter; e.g., Whitaker et al. 2012b) is interpreted as a possible consequence of the short time-scale of the dominant quenching process (Peng et al. 2010) moving the field SFGs out of the MS. As a consequence, the displacement of the cluster members MS towards lower $\mathcal{SFR}$ values could imply that the dominant quenching mechanisms in rich environments are different (e.g., slow quenching mechanisms could populate the region below the MS with transition galaxies on their way to be turned off; Haines et al. 2015, Haines et al. 2013, Paccagnella et al. 2016). However, other works such as Peng et al. (2010), Finn et al. (2010), Wijesinghe et al. (2012), or Tyler et al. (2013) find the same $\mathcal{SFR}$ distribution in clusters as in the field at intermediate redshifts. These discrepancies appear to be due to a combination of different factors such as observational biases (e.g., $\mathcal{SFR}$ detection limit), different sample selection functions, and cluster-to-cluster differences (e.g., Geach et al. 2006, Alberts et al. 2016).

A variety of mechanisms have been proposed as the responsible for environmental quenching (see reviews by, e.g., Boselli & Gavazzi 2006 and Haines et al. 2007): gravitational interactions with the potential well of nearby galaxies or the cluster itself, also known as *harassment* (Moore et al. 1996); removal and thermal heating of the interstellar medium of the galaxies by the interaction with the intra-cluster medium (ICM), the so-called *ram-pressure stripping* (RPS; Gunn & Gott 1972, Poggianti et al. 2017); the removal of the hot gas reservoirs of the halo of galaxies, or *strangulation*, and subsequent halt of the supply of material needed to sustain the SF, leading up to the eventual *starvation* (Larson et al. 1980). These mechanisms shape the evolution of galaxies in different time-scales, probably with different efficiency depending on the properties of both galaxies and clusters, and the particular circumstances under which the infall takes place (see, e.g., Boselli & Gavazzi 2006, Berrier et al. 2009). Furthermore, it has also been proposed that the environmental impact on these SFGs starts in early stages of the infall if the accreted galaxies are bound up in small groups (*pre-processing*; e.g., Haines et al. 2015). Distinguishing among these mechanisms remains challenging, and relies on the detailed study and accurate quantification of the changes suffered by the SF processes and structural properties of the galaxies in rich environments.

Recently, a number of state-of-the-art surveys have targeted massive galaxy clusters at intermediate redshift with the main goal of exploring low-luminosity galaxies at high redshift taking advantage of the gravitational lensing phenomenon (e.g., *Hubble* Frontier Fields, Lotz et al. 2017). In this work, we aim at shedding light on the impact of environment on the star-forming activity in galaxies populating clusters by using these surveys to study the cluster inhabitants themselves.

We focus our analysis on 24 X-ray selected (i.e., with total masses $\sim$5 to $\sim$30$\times$10$^{14}M_\odot$) clusters targeted by the *Herschel* Lensing Survey (HLS; Egami et al. 2010), a far-infrared (FIR) and sub-millimetre survey using the ESA *Herschel* Space Observatory, and the Cluster Lensing and Supernova survey with Hubble (CLASH; Postman et al. 2012), a deep optical and near-infrared (NIR) *Hubble* Space Telescope program, as well as by other NIR and mid-infrared (MIR) *Spitzer* programs. The sample extends between $0.187 \leq z \leq 0.890$, thus, covering a particularly interesting cosmic epoch for the study of environmental quenching.

The wealth and quality of this optical-to-NIR photometric dataset allows us to identify cluster galaxies applying a methodology based on photometric redshifts to complement the spectroscopic membership assignment. Furthermore, combining the whole multi-wavelength data we can accurately quantify the average (un)-obscured SF hosted by $\mathcal{M}_*$-selected samples of cluster SFGs. The use of *Herschel* observations complementing optical and NIR data guarantees a proper quantification of the SF shrouded by dust.

Indeed, SFGs detected in the MIR and/or FIR (M-FIR) often have optical colours consistent with those of passively evolving galaxies and therefore, they are easily missed by studies limited to the optical or NIR regimes. Not quantifying the contribution of these obscured processes can lead to an under estimation of the true level of SF by a factor $\sim$10 (Duc et al. 2002). This can extremely affect high density environments studies where, despite the overall reduced SF activity observed, a population of dusty star-forming cluster galaxies has been detected at a wide range of redshifts (e.g., Duc et al. 2002, Fadda et al. 2000, Geach et al. 2006, Marcillac et al. 2007, Saintonge et al. 2008, Bai et al. 2009, Dressler et al. 2009, Haines et al. 2009, Rawle et al. 2010, Biviano et al. 2011, Popesso et al. 2011, Kocevski et al. 2011, Coppin et al. 2011, Rawle et al. 2012b, Alberts et al. 2014, Alberts et al. 2016).

Ultimately, we systematically quantify the suppression of the formation activity in galaxy cluster cores with respect the field. For this end, we consistently build reference field samples across the same redshift range by applying *the same* analysis to the optical-to-FIR publicly available photometry on three of the fields targeted by the Cosmic Assembly Near-infrared Deep Extragalactic Legacy Survey (CANDELS; Grogin et al. 2011, Koekemoer et al. 2011).

This article is organized as follows: Section 2 describes the cluster sample and corresponding data. Section 3 describes our approach to combining the different photometric data and building the multi-wavelength catalogue we use to derive photometric redshifts (Section 4) and physical properties of galaxies through a SED-fitting approach (Section 5). In Section 6, we detail our procedure to select cluster members using spectroscopic and photometric redshifts estimations. The final cluster members samples of SFGs are presented in Section 7 and further characterized in Section 8. The quantification of the SF activity in the core of these clusters is discussed in Section 9. Finally, an interpretation of our results is given in Section 10, and a summary and the main conclusions of this work are given in Section 11.

Throughout this work we assume a flat ΛCDM cosmology with H_0=70 km s^{-1}Mpc^{-1}, Ω_m=0.3, and Ω_Λ=0.7. Star-formation rates and stellar masses are based on a Salpeter (1955) initial mass function (IMF).

The catalogues of star-forming cluster members associated to this paper, including multi-wavelength photometry, photometric redshifts, and physical properties, can be downloaded from the public flavour of the RAINBOW Cosmological Database[1] (Pérez-González et al. 2008, Barro et al. 2011a,b).

2 GALAXY CLUSTERS SAMPLE & DATA

The *Herschel Lensing Survey* (HLS; Egami et al. 2010) is a large imaging survey of galaxy clusters in the far-infrared (FIR) and sub-millimetre using the ESA *Herschel Space Observatory* (Pilbratt et al. 2010). HLS provides deep PACS (Poglitsch et al. 2010) and SPIRE (Griffin et al. 2010) imaging (see Section 2.3) for a sample of 65 X-ray-luminous (i.e., massive) clusters of galaxies in the redshift range between $0.2 \lesssim z \lesssim 0.9$. The primary aim of HLS is to observe the most effective gravitational lenses available, probing beyond the confusion limit of the Herschel instruments to observe intrinsically faint, high-redshift sources (e.g., Rex et al. 2010; Rawle et al. 2010). However, the HLS is also a remarkable survey for the study of SF processes taking place within high density environments (e.g., Rawle et al. 2016, 2014). On the one hand, it targets a significant number of clusters, which avoids deriving misleading results due to cluster-to-cluster variations (e.g., Alberts et al. 2016). On the other hand, the clusters targeted by the HLS span over a redshift range in which these systems are thought to undergo a major evolution due to the transformation of infalling star-forming field galaxies into passive objects (e.g., Kauffmann 1995, Haines et al. 2015).

Among the fields targeted by the HLS, we focus our work on a subsample of 24 clusters (see Table 2) also observed by the *Cluster Lensing and Supernova survey with Hubble* (CLASH; Postman et al. 2012). CLASH is a Multi-Cycle Treasury Program with the aim of providing ultra-deep photometry of 25 X-ray selected, massive ($\sim$5 to $\sim$30 $\times$ 10^{14} $M_\odot$) galaxy clusters in a total of 16 passbands using HST ACS/WFC, WFC3/UVIS, and WFC3/IR (see Section 2.1 for details). CLASH clusters are drawn heavily from the Abell and MACS cluster catalogues (Abell 1958, Abell et al. 1989, Ebeling et al. 2001, Ebeling et al. 2007, Ebeling et al. 2010, Mann & Ebeling 2012).

The wealth of photometric and spectroscopic data available for this galaxy clusters sample, that we call CLASH+HLS, enables the accurate identification and characterization of their galaxy population (e.g., Annunziatella et al. 2016, Maier et al. 2016, Balestra et al. 2016). Indeed, CLASH+HLS clusters have been extensively studied in previous works. CLASH photometry together with spectroscopy from different surveys (see Section 2.4) have provided strong constraints on the cluster inner mass distributions and profiles (e.g., Zitrin et al. 2015, Biviano et al. 2013, Annunziatella et al. 2014). Also, their dynamical state and substructures have been analyzed through different techniques, such as the Sunyaev-Zel'dovich effect (SZ; Sunyaev & Zel'dovich 1972, Rumsey et al. 2016) and X-ray surface brightness analysis (see Rumsey et al. 2016 and references therein), as well as lensing (e.g., Zitrin et al. 2013, Grillo et al. 2015) and

---

[1] http://rainbowx.fis.ucm.es

Table 1. Description of the galaxy cluster sample. We display the following information: (1) Cluster ID; (2-3) Coordinates of the cluster centre as in Postman et al. (2012); (4) redshift Postman et al. 2012; (5) Velocity dispersion (we use the value $\sigma_{\rm cl}$=1600 km s^{-1} when no observational estimation was found in the literature); (6) Radius within which the mean density is 200 times the critical density at the redshift where the cluster is located ($\sim R_{\rm virial}$ according to the simulations of Evrard et al. 1996; we use R_{200}=2000 kpc, see for instance Umetsu et al. (2014), for those cases for which no precise value was found in the literature); (7) The SF activity of the BCG as quantified through the emission of the UV, corrected for extinction ($\mathcal{SFR}_{\rm BCG,UV,corr.}$; Donahue et al. 2015) and the emission in the FIR ($\mathcal{SFR}_{\rm BCG,TIR}$; Rawle et al. 2012a); (8) cool-core tracer $\mathcal{C}$ parameter as published by Donahue et al. (2016); (9) number of spectroscopic redshifts within the area covered by the CLASH catalogue ($\sim$0.0015 deg^2). Note: $^+$ 0.209 according to Mercurio et al. (2003); ^{a} Geller et al. (2014); ^{b} Mercurio et al. (2003); ^{c} Gómez et al. (2012); ^{d} Balestra et al. (2016); ^{e} Biviano et al. (2013); ^{f} Ebeling et al. (2007); ^{g} Annunziatella et al. (2016); ^{h} Newman et al. (2013); ^{i} Rosati et al. (2014); ^{j} Coe et al. (2012); ^{k} Karman et al. (2015); ^{l} Huchra et al. (2012); ^{m} Ebeling et al. (2014); ^{n} Treu et al. (2015) and Schmidt et al. (2014); ^{o} Ravindranath & Ho (2002); ^{p} Cohen & Kneib (2002); ^{q} Shectman et al. (1996); ^{r} Abazajian et al. (2009); ^{s} $\sigma_{\rm cl}$ and $\mathcal{R}_{200}$ derived using the value of the mass within $\mathcal{R}_{200}$ ($\mathcal{M}_{200}$) from Umetsu et al. (2014).

ID	RA [J2000]	Dec [J2000]	z	$\sigma_{\rm cl}$ [km s^{-1}]	R_{200} [kpc]	$\mathcal{SFR}_{\rm BCG,\,UVcorr.}/{\rm TIR}$ [$M_\odot {\rm yr}^{-1}$]	$\mathcal{C}$	$\#z_{\rm spec}$
(1)	(2)	(3)	(4)	(5)	(6)	(7)	(8)	(9)
A0383	02:48:03.40	-03:31:44.9	0.187	$931^{+59}_{59}{}^{a}$	$1220^{+10}_{-10}{}^{a}$	3.3±0.4 / 4.0±0.2	0.525	$37^{a,h}$
A0209	01:31:52.54	-13:36:40.4	0.206^+	$1394^{+88}_{-99}{}^{b}$	$2130^{+50}_{-50}{}^{g}$	1.2±1.1 / –	0.167	$73^{b,i,g}$
A2261	17:22:27.18	32:07:57.3	0.224	1524^{s}	1942^{s}	3.3±2.8 / –	0.331	5^{j}
RBS1748	21:29:39.94	00:05:18.8	0.234	1600	2000	2.9±0.4 / –	0.426	–
A0611	08:00:56.82	36:03:23.6	0.288	1316^{s}	$1760^{+97}_{-89}{}^{h}$	0.9±1.7 / –	0.335	23^{h}
MS2137	21:40:15.18	-23:39:40.7	0.313	1257^{s}	$1318^{+140}_{-107}{}^{h}$	5.6±0.7 / –	0.589	–
AS1063	22:48:43.96	-44:31:51.3	0.348	$1660^{+230}_{-150}{}^{c}$	2376^{s}	2.3±0.5 / –	0.194	$136^{i,k}$
MACS1931	19:31:49.66	-26:34:34.0	0.352	1339^{s}	1641^{s}	83.1±2.3 / –	0.545	–
MACS1115	11:15:51.90	01:29:55.1	0.355	1364^{s}	1668^{s}	6.4±0.5 / –	0.430	–
RXJ1532	15:32:53.78	30:20:58.7	0.363	1031^{s}	1278^{s}	48.6±2.6 / –	0.571	1^{l}
MACS1720	17:20:16.95	35:36:23.6	0.387	1296^{s}	1569^{s}	6.1±0.7 / –	0.417	–
MACS0416	04:16:09.39	-24:04:03.9	0.397	$996^{+12}_{-36}{}^{d}$	$1820^{+110}_{-110}{}^{d}$	3.5±0.8 / –	0.091	$219^{d,n,m}$
MACS0429	04:29:36.05	-02:53:06.1	0.399	1140^{s}	1385^{s}	20.1±2.1 / –	0.531	–
MACS1206	12:06:12.15	-08:48:03.4	0.440	$1087^{+53}_{-55}{}^{e}$	$1980^{+100}_{-100}{}^{e}$	6.8±3.0 / –	0.223	81^{e}
MACS0329	03:29:41.56	-02:11:46.1	0.450	1165^{s}	1386^{s}	31.0±2.4 / –	0.488	–
RXJ1347	13:47:30.59	-11:45:10.1	0.451	1710^{s}	1987^{s}	16.5±1.8 / –	0.506	$42^{o,p,q}$
MACS1311	13:11:01.67	-03:10:39.5	0.494	1600	2000	5.8±1.9 / –	0.488	–
MACS1149	11:49:35.69	22:23:54.6	0.544	$1840^{+120}_{-170}{}^{f}$	2352^{s}	2.1±0.7 / –	0.111	378^{m}
MACS0717	07:17:32.63	37:44:59.7	0.545	$1660^{+120}_{-130}{}^{f}$	2358^{s}	5.4±1.4 / –	0.055	$143^{l,m}$
MACS1423	14:23:47.76	24:04:40.5	0.545	$1300^{+120}_{-170}{}^{f}$	2000	16.7±1.2 / 46.5±0.8	0.555	96^{m}
MACS2129	21:29:26.06	-07:41:28.8	0.570	$1400^{+120}_{-180}{}^{f}$	2000	1.6±0.1 / –	0.211	85^{m}
MACS0647	06:47:50.27	70:14:55.0	0.584	$900^{+170}_{-200}{}^{f}$	1442^{s}	2.1±0.3 / –	0.242	–
MACS0744	07:44:52.82	39:27:26.9	0.686	$1101^{+130}_{-150}{}^{f}$	1521^{s}	8.5±3.1 / –	0.365	–
CLJ1226	12:26:58.37	33:32:47.4	0.890	1600	2000	2.7±1.5 / –	0.245	$9^{l,r}$

kinematics of galaxy populations (e.g., Girardi et al. 2015). Despite the X-ray selection, that generally favours highly relaxed clusters, the sample is found to be not homogeneously dynamically relaxed (Postman et al. 2012, Rumsey et al. 2016). Finally, a number of works have studied in detail the brightest cluster galaxies (BCG) of the CLASH+HLS systems. For instance, Donahue et al. (2015) and Donahue et al. (2016) carried out a study on the morphology and SF activity of these peculiar galaxies, using the rest-frame UV imaging provided by CLASH. Furthermore, they also characterized the intra cluster gas in the vicinity of the BCGs and beyond, by analysing the X-ray emission of the inner cluster cores. Complementary, Rawle et al. (2012a) studied the obscured SF activity undergone by the BCGs of the massive clusters observed by HLS, and its dependence with the X-ray gas cooling times for cool-core (CC) clusters[2].

In the following subsections, we describe the photometric and spectroscopic datasets available on the cluster fields

(see Table 2 & 3 for a summary of their main characteristics), as well as other ancillary data found in the literature.

2.1   *Hubble* optical and near-infrared photometry

In this work, we use the CLASH[3] photometric dataset published by Postman et al. (2012). This data release contains the photometry performed on the *HST* ACS/WFC (F435W, F475W, F606W, F625W, F775W, F814W, and F850LP), WFC3/UVIS (F225W, F275W, F336W, and F390W), and WFC3/IR (F105W, F110W, F125W, F140W, and F160W) deep imaging of 25 massive intermediate redshift clusters. Object detection and photometry is accomplished using SExtractor (Bertin & Arnouts 1996) in dual image mode using a weighted sum of the ACS/WFC and WFC3/IR images (see Postman et al. 2012 for details on the *HST* data reduction, catalogue build up, and main characteristics). These catalogues cover an area of $\sim$5 arcmin^2, limited by the WFC3/IR images ($\sim$2.0×2.3 arcmin^2), and therefore,

---

[2] Cool-core clusters are defined as those systems with X-ray cooling times <1 Gyr (Fabian 1994).

[3] https://archive.stsci.edu/prepds/clash/

Table 2. In this table we show an overview of the photometric bands used in this work: (1) name of the observing band and instrument; (2) effective wavelength of the filter; (3) median FWHM of the PSF in arcseconds; (4) name of the project to which the data belongs. (*) Spitzer Programs #17 (PI: Fazio), #83 (PI: Rieke), #545 (PI: Egami), #40652 (PI: Kocevski), #50393 (PI: Kocevski), #60034 (PI: Egami), #80168 (PI: Bouwens). ($^{+}$) Spitzer Programs #83 (PI: Rieke), #40652 (PI: Kocevski), #40872 (PI: Smith), #50393 (PI: Kocevski).

Band	λ_{eff}	FWHM	Project
(1)	(2)	(3)	(4)
WFC3-F225W	237.84 nm	$0''.08$	CLASH
WFC3-F275W	271.47 nm	$0''.08$	CLASH
WFC3-F336W	335.86 nm	$0''.07$	CLASH
WFC3-F390W	393.22 nm	$0''.07$	CLASH
ACS-F435W	436.33 nm	$0''.08$	CLASH
ACS-F475W	475.05 nm	$0''.08$	CLASH
ACS-F606W	596.11 nm	$0''.08$	CLASH
ACS-F625W	630.97 nm	$0''.08$	CLASH
ACS-F775W	770.59 nm	$0''.08$	CLASH
ACS-F814W	807.31 nm	$0''.09$	CLASH
ACS-F850LP	905.26 nm	$0''.09$	CLASH
WFC3-F105W	1.06 μm	$0''.13$	CLASH
WFC3-F110W	1.15 μm	$0''.13$	CLASH
WFC3-F125W	1.25 μm	$0''.14$	CLASH
WFC3-F140W	1.40 μm	$0''.14$	CLASH
WFC3-F160W	1.54 μm	$0''.15$	CLASH
IRAC-3.6 μm	3.56 μm	$2''.1$	*
IRAC-4.5 μm	4.50 μm	$2''.1$	*
IRAC-5.8 μm	5.74 μm	$2''.2$	*
IRAC-8.0 μm	7.93 μm	$2''.2$	*
MIPS-24 μm	23.84 μm	$5''$	+
PACS-100 μm	102.25 μm	$8''$	HLS
PACS-160 μm	165.59 μm	$12''$	HLS
SPIRE-250 μm	253.13 μm	$18''$	HLS
SPIRE-350 μm	355.87 μm	$25''$	HLS
SPIRE-500 μm	511.19 μm	$36''$	HLS

they mainly sample the very inner cluster cores. An angular distance of 2.0 arcmin corresponds to 375 kpc and 932 kpc for the lowest and largest redshifts in the sample, respectively. The total area covered, including the 24 clusters, is $\sim$135 arcmin^2. The exposure times of the frames vary between 2000 and 5000 s, reaching average (5σ) limiting AB magnitudes of $\sim$26. A summary of the properties of the dataset is shown in Table 2.

2.2 *Spitzer* near and mid-infrared photometry

A series of programs with *Spitzer* have covered all CLASH clusters with IRAC 3.6 and 4.5μm bands. Furthermore, 40% of them have also been observed with IRAC 5.8 and 8.0μm channels, and 50% has been covered by MIPS 24μm band. These data were extracted from the *Spitzer* Heritage archive [4]. *Spitzer* images reduction, source detection, and photometry were carried out as described in Pérez-González et al. (2005) and Pérez-González et al. (2008), for MIPS and IRAC, respectively. Briefly, the data reduction was carried out with MOPEX (Mosaicking and Point-source Extraction), the package provided by the *Spitzer* Science Center for reducing and analysing imaging data. In the case

[4] http://irsa.ipac.caltech.edu/applications/Spitzer/SHA

of IRAC, the source detection and photometry were carried out with SExtractor (Bertin & Arnouts 1996), using the same procedure as Huang et al. (2004). Photometry was performed using a small circular aperture, and an aperture correction was applied to get the total flux. IRAC beam sizes are 2.1, 2.1, 2.2, and 2.2$''$ respectively for increasing wavelengths. The average sensitivities reached at 5σ are 1.4, 1.5, 4.5, 4.2 μJy. In the case of MIPS images, characterized by a larger point-spread function, the photometry was extracted by PSF fitting. Several detection passes are used in order to make catalogues as complete as possible, in spite of the significant source confusion. The MIPS 24μm beam size is 5$''$. The average MIPS 24μm limiting flux at 5σ is 234 μJy. In Table 2 and 3 we summarize the properties of these photometric catalogues. We report the heterogeneous sensitivities reached by IRAC and MIPS imaging on the different CLASH clusters. In particular, MIPS 24μm limiting fluxes vary between 77 and 852 μJy.

2.3 *Herschel* far-infrared photometry

This study employs the PACS 100, 160μm, and SPIRE 250, 350, 500μm imaging provided by HLS for all the clusters. We use the catalogues created by the HLS team following the methodology presented by Pérez-González et al. (2010) and Rawle et al. (2010, 2016). Source catalogues and photometry in all bands were obtained with standard PSF fitting methodology, relying on a set of fixed IRAC and MIPS prior position catalogues. PACS imaging at 100 and 160μm has mean 5σ flux limits of 4.7 and 8.7 mJy, while in the three SPIRE bands, the typical 5σ limits are 19.4, 15.3, and 13.7 mJy, respectively for the 250, 350, and 500μm bands. The beam sizes for the five *Herschel* bands (sorted by increasing effective wavelength) are 8, 12, 18, 25, and 36$''$, respectively.

2.4 Spectroscopic Data

One of the programs with a greater contribution to our spectroscopic redshift sample is the spectroscopic survey carried out on the 13 southern CLASH clusters with the Visible Multi-Object Spectrograph (VIMOS; Le Fèvre et al. 2003) mounted on the Very Large Telescope (VLT), the so-called CLASH-VLT survey (CLASH-VLT Large Programme 186.A0.798; P.I.: P. Rosati; Rosati et al. 2014). We refer the reader to Biviano et al. (2013) and Balestra et al. (2016) for details on spectroscopic data, target selection, and performance statistics of the mentioned project. We also make use of spectroscopic redshift measurements from the Grism Lens Amplified Survey from Space (GLASS; Schmidt et al. 2014; Treu et al. 2015), a large *Hubble Space Telescope* program aimed at obtaining grism spectroscopy of the HFF. Besides these, we also gather spectroscopic redshifts from other surveys (see Table 1 for a complete list of the works included). Finally, we also retrieve redshifts through NASA/IPAD Extragalactic Database (NED), mainly from the 2MASS Redshift Survey (Huchra et al. 2012), and the Seventh Data Release of the Sloan Digital Sky Survey (Abazajian et al. 2009). In Section 4 we describe the properties of the final spectroscopic sample.

Table 3. Limiting fluxes (5σ) of the *Spitzer* and *Herschel* photometric catalogues used in this work.

	$\mathcal{F}_{\mathrm{lim}}$ [μJy]					$\mathcal{F}_{\mathrm{lim}}$ [mJy]				
	Spitzer/IRAC				*Spitzer*/MIPS	*Herschel*/PACS		*Herschel*/SPIRE		
Cluster	3.6μm	4.5μm	5.8μm	8.0μm	24μm	100μm	160μm	250μm	350μm	500μm
(1)	(2)	(3)	(4)	(5)	(6)	(7)	(8)	(9)	(10)	(11)
A0209	2.0	1.7	5.2	5.4	268.7	4.6	9.1	14.6	14.0	10.7
A0383	2.7	2.2	6.7	6.3	317.6	4.8	9.4	14.8	13.7	10.8
MACS0329	1.3	1.3	–	–	–	4.5	8.5	19.9	15.8	14.7
MACS0416	1.2	1.2	–	–	–	4.7	8.5	19.2	14.9	13.9
MACS0429	1.3	1.3	–	–	–	4.5	8.3	21.0	16.7	14.4
MACS0647	1.1	1.3	–	–	–	4.8	10.8	23.1	20.3	14.7
MACS0717	1.7	1.9	–	–	133.3	4.7	9.2	17.8	15.9	12.0
MACS0744	2.2	3.0	1.2	1.8	–	4.4	8.4	14.5	14.1	11.3
A0611	1.0	1.0	–	–	380.6	4.8	8.4	15.0	13.9	11.1
MACS1115	1.3	1.4	–	–	–	4.7	8.7	20.4	16.1	14.5
MACS1149	0.9	0.9	–	–	–	4.7	8.6	15.1	15.3	14.9
MACS1206	1.1	1.1	–	–	305.7	4.5	10.3	25.8	21.9	18.3
CLJ1226	3.6	3.6	2.0	1.8	131.7	6.5	11.3	22.2	18.3	18.6
MACS1311	1.2	1.4	–	–	–	4.7	8.4	20.1	15.6	14.2
RXJ1347	1.7	1.5	4.5	2.7	143.7	4.3	7.8	21.1	18.6	18.5
MACS1423	1.4	1.8	–	–	95.5	5.2	9.5	14.2	12.6	10.3
RXJ1532	1.2	1.2	–	–	180.3	4.8	8.4	18.3	14.5	13.5
MACS1720	0.9	0.8	–	–	–	4.7	8.7	19.6	14.9	13.0
A2261	1.9	1.9	5.8	4.6	108.5	4.6	8.9	20.0	16.1	14.0
MACS1931	3.6	2.7	–	–	851.9	4.5	8.7	19.5	15.2	13.4
MACS2129	1.9	1.7	1.1	1.6	112.6	5.2	13.7	33.5	28.3	29.2
RBS1748	1.2	1.2	–	–	311.8	4.5	9.4	15.3	14.5	11.4
MS2137	1.8	1.6	7.1	7.7	97.7	5.1	9.4	14.5	13.3	11.1
AS1063	2.2	1.7	6.6	6.0	76.9	4.8	7.7	14.7	14.6	10.9

3   MULTI-WAVELENGTH PHOTOMETRY

We merge the photometric datasets described in the previous section to obtain UV-to-FIR SEDs for all the sources in the catalogues released by CLASH. To this end, we use the RAINBOW Cosmological Database (Pérez-González et al. 2008, Barro et al. 2011a,b) and associated software package. We use CLASH catalogues as parent catalogues to take advantage of the high resolution of HST imaging. However, this requires taking special care of the inevitable blending of sources in bands with poorer resolution, as well as possible counterpart misidentification.

In the following subsections, we describe the strategy that we use for the build-up of our multi-wavelength photometric catalogue.

3.1   Cross-matching catalogues

Initially, RAINBOW searches for counterparts of our parent catalogue in the rest of the bands. In practice, each catalogue is cross-matched to the CLASH positions. RAINBOW takes into account possible astrometry offsets between the bands by re-aligning each pair of them using the positions of several sources in small $1'\times1'$ boxes around a given source. The search radii we use to find counterparts candidates are $1''.5$, $2''.5$, $2''.5$, $4''.0$, $9''.0$, $9''.0$, and $12''.0$ for IRAC, MIPS 24μm, PACS 100 and 160μm, and SPIRE 250, 350, and 500μm catalogues. These values are chosen in order to cope with the typical WCS offsets between different images, as well as uncertainties in the determination of the center for faint MIPS and *Herschel* sources. We note, however, that a comparison of the CLASH vs MIPS/*Herschel* coordinates for secure (i.e., bright) mid- and far-IR sources points out that the typ-

ical WCS uncertainty is $\sim0''.2$ for IRAC, $\sim0''.4$ for MIPS, $\sim0''.4$ for PACS, and $\sim1''.3$ for SPIRE. In Section 3.3 we take into account both the search radius and the WCS accuracy measurements to discuss how many *HST* counterparts we find for each M- and FIR source, and how we select the most likely among the former.

3.2   IRAC fluxes deblending

The IRAC photometry is recomputed on CLASH positions following a deconvolution method detailed in Barro et al. (2011a). The procedure is similar to that used in, e.g., Grazian et al. (2006), Wuyts et al. (2008), Williams et al. (2009), or Wang et al. (2010), and briefly consists on the convolution of the PSF of the higher resolution image to the IRAC PSF and a subsequent scaling of the flux of each source in a way that the total flux equals the emission of the blended source in the lower resolution image.

3.3   M- and FIR counterpart assignment

Given the larger beam sizes of the M/FIR bands, a simple cross-correlation of the optical/NIR and M/FIR catalogues frequently assigns the same M/FIR source to different optical/NIR counterparts (especially when using *HST* images). On average, the relaxed search radii we use to cross-match catalogues lead to the assignation of each MIPS 24μm, PACS, and SPIRE source to 2, 5, and 32 optical/NIR sources, respectively. However, within the WCS accuracy measurements there are, on average, 1 optical/NIR source for each detection in MIPS 24μm, PACS, and SPIRE 250μm and 250μm, and 2 optical/NIR sources for

each SPIRE 500μm source. These latter values are more informative of the level of uncertainty in our cross-matching procedure and reliability of the counterparts identification, as well as possible blending affecting the low resolution bands.

Due to the large difference between the resolution of CLASH and M/FIR bands, it is not advisable to apply a deblending procedure such as it was done on IRAC photometry. Instead, we limit our approach to the identification of the *most likely* counterpart, or dominant contributor to the M/FIR fluxes, among the multiple short wavelength counterparts assigned to the same M/FIR sources. The fact that the FIR catalogues are built using IRAC and MIPS 24μm priors guarantees a consistent framework to link the photometry across the whole wavelength range. Different studies have addressed the task of identifying counterparts of FIR/Sub-millimetre galaxies in shorter wavelengths (e.g., Alberts et al. 2013), avoiding using simply the shortest distance match with the aim of achieving a more physically driven identification. Our approach *steps through* the N-to-FIR wavelength range and evaluates which of the IR SEDs of the multiple candidates is most likely to be associated with the M/FIR detection.

We first set local and average SNR limits in the FIR bands. These limits are 2σ and 3σ for MIPS and *Herschel* bands (see Table 3, where we show the flux values corresponding to the 5σ detection in each band and cluster). The 2σ is used to maximize the information available to identify the FIR counterparts, however, we clarify that we do not consider MIPS 24μm fluxes below 3σ detections in the rest of the work. Then, we select as the optical/NIR counterpart of each MIPS 24μm source the brightest candidate in the reddest IRAC band available. Then, we shift this methodology to larger wavelength bands. We select as the optical/NIR counterpart of each PACS source the brightest candidate in MIPS 24μm. When MIPS is not available, we use the reddest IRAC band in which the source is detected. Finally, we select as the optical/NIR counterpart of each SPIRE source, the brightest candidate in the reddest PACS band available, if any. Otherwise, MIPS 24μm and IRAC bands are used. If different optical/NIR candidates present very similar fluxes (within 1σ) in the band that is used to identify the counterpart, we impose a criterion of minimum distance, and therefore, we select as the optical/NIR counterpart the galaxy with the closest position to the M/FIR source. In all cases described, the MIPS, PACS, and SPIRE fluxes of the CLASH sources that are not identified as real counterparts are flagged and they are not used subsequently. Therefore, each M/FIR source is assigned to a single optical/NIR source. We note that using IRAC as a tracer of PACS or SPIRE emitters can lead to spurious associations. This is because NIR and FIR trace different components and processes in the galaxies. In the clusters with MIPS coverage, the average fraction of *Herschel* sources' optical counterparts identified by their IRAC fluxes is 20% and 32% for PACS and SPIRE, respectively. These values increase, however, in those fields without MIPS photometry, reaching 91% and 49%, respectively. These cases are flagged for further check. After a thorough visual inspection of the output of our procedure, we detect only obvious mismatch cases in galaxies located in the border of the *HST*/WFC3 images. We have identified a number of galaxies suffering from over-deblending in the CLASH catalogues, which means that the photometry of these galaxies are divided into different sources. In these cases, the flux of the MIR and FIR catalogues are generally assigned to source corresponding to the central region of the galaxy.

4 PHOTOMETRIC REDSHIFTS

Photometric redshifts ($z_{\rm phot}$) are computed using the EAZY code (Brammer et al. 2008), specifically conceived for this task. EAZY is a template-fitting code based on χ^2 minimization between observed photometry and a set of 6 SED templates. Among them, 5 templates are generated following the Blanton & Roweis (2007) *non-negative matrix factorization* algorithm with PEGASE stellar population synthesis models (Fioc & Rocca-Volmerange 1997) and a calibration set of synthetic photometry derived from semi-analytic models. The last one is a dusty starburst model, and it is added to the set in order to compensate for the lack of dusty galaxies in the calibration photometric sample.

The achievable quality of photometric redshifts depends strongly on the quality of the photometric dataset itself, and the wavelength domain it covers (e.g., Pacifici et al. 2012). In particular, it benefits from high-quality photometry sampling strong continuum features (e.g., Lyman or Balmer breaks). In this sense, the 16 CLASH broadband photometric points enable high levels of accuracy in the photometric redshift estimation (Jouvel et al. 2014, Molino et al. 2017, Connor et al. 2017). In order to make use of the whole potential of our dataset, we fit not only the whole wavelength range covered by CLASH, but also the IRAC photometric points. Furthermore, for those clusters with available spectroscopic samples we perform a zero-point fine-tuning (following the methodology by Barro et al. 2011a,b) to account for mismatches between the CLASH colours and the SED-fitting template library colours, or other hypothetical systematic problems. The median absolute zero-points used are 3% and 5% for CLASH and IRAC bands, respectively.

4.1 Photometric redshifts quality

We assess the quality of the $z_{\rm phot}$ obtained for each cluster by comparing them against the available and reliable[5] $z_{\rm spec}$. We cross-correlate CLASH dataset with the spectroscopic catalogues using a radius of $0''.5$. The total reference spectroscopic sample is composed of 1034 spectroscopically confirmed galaxies within the area of the WFC3 imaging (i.e. the area covered by the photometric catalogues) over the 24 CLASH+HLS clusters we analyse. This sample is by definition inhomogeneous, as can be expected of the combination of studies designed with different scientific objectives and selection criteria. It extends between $0.1 < z \lesssim 9$, with the 90% of the galaxies at $z < 2$. Figure 1 displays the distribution of $z_{\rm spec}$ (empty histogram), and the distribution of magnitudes in the ACS/F814W band (empty histogram; nested panel).

---

[5] The *reliability* of the $z_{\rm spec}$ is given by the spectroscopic surveys in the form of a quality flag normally linked to the number and SNR of the spectral features identified on the spectrum, that are used to calculate the redshift.
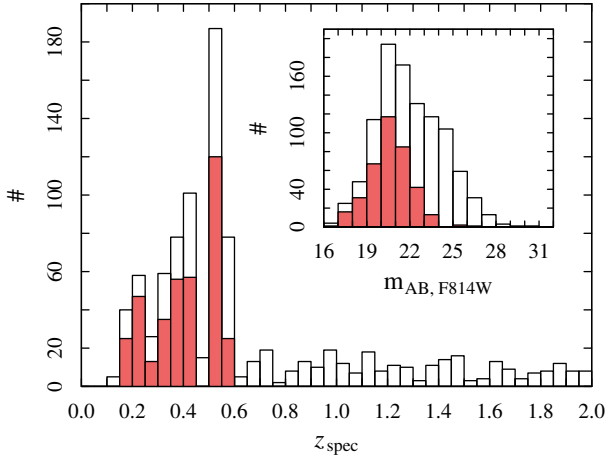
Figure 1. Distribution of $z_{\rm spec}$ for our spectroscopic sample (1034 galaxies; empty histogram). The distribution of the redshifts of the 378 spectroscopically confirmed cluster members is given in red. In this figure, we show the distribution up to z=2, which contains 90% of the sample. The nested panel shows the corresponding distribution of magnitudes in the ACS/F814W band.

A number of quantities have been used in the literature to quantify the behaviour of the data points in this diagram (see, e.g., Pelló et al. 2009), either in terms of scatter, as well as the presence of outliers and systematic offsets. In the last decade, the normalized median absolute deviation ($\sigma_{\rm NMAD}$; Hoaglin et al. 1983) of the difference between the $z_{\rm phot}$ and the $z_{\rm spec}$ ($\Delta z = z_{\rm phot} - z_{\rm spec}$) has been frequently used to characterize the scatter of the distribution of $z_{\rm phot}$ (e.g., Ilbert et al. 2009). A typical photometric redshift error distribution has tails that clearly depart from a pure Gaussian distribution, in addition to a relatively large fraction of outliers. The $\sigma_{\rm NMAD}$ estimator manages to achieve a stable estimate of the spread of the core of the $z_{\rm phot}$ distribution without being affected by the mentioned tails. It is defined as

$$\sigma_{\rm NMAD} = 1.48 \times {\rm median}\left(\frac{|\Delta z - {\rm median}\,(\Delta z)|}{1 + z_{\rm spec}}\right). \qquad (1)$$

Following the notation by Barro et al. (2011b), we consider the fraction of catastrophic outliers, η, defined as those cases for which

$$|\Delta z|/(1 + z_{\rm spec}) > 0.2. \qquad (2)$$

Finally, in order to characterize the systematic offsets of the photometric redshifts obtained, δ, we use the expression

$$\delta = \Delta z/(1 + z_{\rm spec}). \qquad (3)$$

When compared with the spectroscopic sample, our photometric redshift estimations present $\sigma_{\rm NMAD}$=0.04, and 8% of catastrophic outliers (see Figure 2). The outliers are typically either faint sources with noisy photometry in *HST* and/or IRAC bands (e.g., high redshift galaxies, objects located in the border of the CLASH catalogues) or galaxies for which the IRAC photometry seems to be contaminated by bright nearby objects. We do not identify systematic effects,
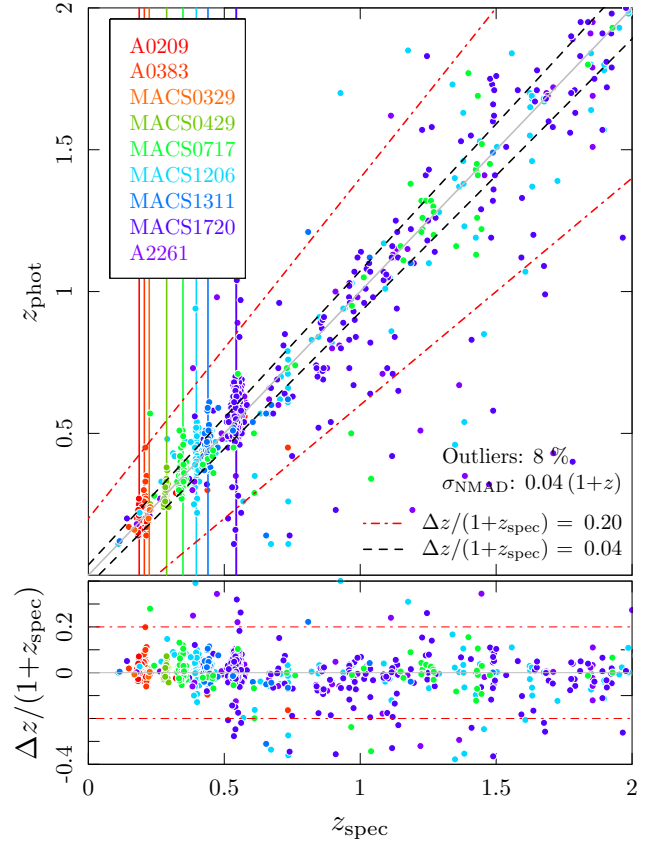

Figure 2. Evaluation of the $z_{\rm phot}$ quality. The black and red dashed lines show, respectively, the accuracy reached by our results considering the whole spectroscopic sample and the definition of outlier. The vertical lines mark the redshift of each cluster (Table 2).

with an average δ=−0.01. These values are comparable with those published by Jouvel et al. (2014) for CLASH clusters.

As we are using the $z_{\rm phot}$ to select cluster members, we also assess their quality using only a subsample of spectroscopic members. We follow the selection criteria used by Molino et al. (2017, see Section 4.2) in order to be able to compare our results with theirs. The cluster members reference spectroscopic sample is formed by galaxies for which the difference between its $z_{\rm spec}$ and the cluster redshift ($\Delta z_{\rm cl}$) fulfills $|\Delta z_{\rm cl}| \leq 0.01$. Also, in order to guarantee an optimal sampling of the optical and NIR SED, only galaxies detected at least on 14 CLASH bands are considered. Using these criteria we select 378 galaxies (see red histogram in Figure 1). In this case, our photometric redshift estimations present $\sigma_{\rm NMAD}$=0.03, and 2% of catastrophic outliers. These values are comparable with to those obtained by Molino et al. (2017): $\sigma_{\rm NMAD}$=0.02, and η<3%. Neither in this case we identify systematic effects, with an average deviation δ=0.01.

5 SPECTRAL ENERGY DISTRIBUTION FITTING WITH RAINBOW

In order to derive the physical properties of the galaxies found on CLASH+HLS fields, we apply a SED-fitting analysis to the entire dataset gathered and described in the previous sections. We use the RAINBOW Cosmological Database software package (Pérez-González et al. 2008; Barro et al. 2011a,b) to fit, on the one hand, the optical/NIR photometry (CLASH & IRAC), and on the other hand, the M/FIR photometry (MIPS & *Herschel*). In both cases, we fix the redshifts derived with EAZY or, when available, the $z_{\rm spec}$.

In particular, the optical/NIR fitting code performs a χ^2 minimization between the observed data and a set of semi-empirical template SEDs computed from spectroscopically confirmed galaxies modeled with PEGASE stellar population synthesis models (Fioc & Rocca-Volmerange 1997). In particular, we use the templates generated by Pérez-González et al. 2008 (see their Appendix B) assuming a single stellar population with a exponentially declining star formation history (SFH; $\mathcal{SFR}(t) \propto e^{-t/\tau}$) with a time-scale ($\tau$) varying between $1\,$Myr (instantaneous burst) and $100\,$Gyr (constant SFH) and an age that can take values between $1\,$Myr and $13.5\,$Gyr. We also assume a Salpeter (1955) IMF spanning stellar masses from 0.1 to 100 $M_\odot$, metallicity ($\mathcal{Z}$) values 0.005, 0.0.02, 0.2, 0.4, 1.0, 2.5, and 5.0 $\mathcal{Z}_\odot$, extinction between 0 and 5 mag, and a Calzetti et al. (2000) attenuation law. We complement the set of templates with QSO and AGN empirical templates drawn from Polletta et al. (2007) that account for the galaxies whose UV-to-NIR emission is domitated by an AGN. In the case of the M/FIR SED-fitting, the χ^2 minimization is performed between the observed photometry and the typical dust emission models by Chary & Elbaz (2001), Dale & Helou (2002), Rieke et al. (2009), and Draine & Li (2007).

5.1 Stellar masses

The $\mathcal{M}_*$ of each galaxy is estimated by RAINBOW from the average scale factor required to match the template monochromatic luminosities to the observed fluxes, weighted with the photometric errors. The random uncertainty of the $\mathcal{M}_*$ is derived from the dispersion in the mass-luminosity rations in the different bands. The average expected uncertainty in the estimations of $\mathcal{M}_*$ taking into account variations in $\mathcal{Z}$, SFH, or IMF are within 0.3 dex (Pérez-González et al. 2008).

5.2 Star formation rates

We take advantage of our rich dataset to analyse the SF activity undergone by the galaxies in these fields in terms of total $\mathcal{SFR}$ ($\mathcal{SFR}_{\rm TOT}$). Similarly to previous works (see Kennicutt & Evans 2012 and references therein), we consider that the total SF activity of a galaxy can be derived from the combination of (1) the UV luminosity emitted by young stars that is able to escape from the inter-stellar medium (ISM), and (2) the UV luminosity that is absorbed by the ISM and re-emitted in the M/FIR regime. We use the recipe of Bell et al. (2005), which is based on the calibration of

Kennicutt (1998):

$$\mathcal{SFR}_{\rm TOT} = \mathcal{SFR}_{\rm TIR} + \mathcal{SFR}_{\rm UV} \qquad (4)$$

$$\mathcal{SFR}_{\rm TIR}/M_\odot yr^{-1} = 1.8 \times 10^{-10} \mathcal{L}_{\rm TIR}/L_\odot \qquad (5)$$

$$\mathcal{SFR}_{\rm UV}/M_\odot yr^{-1} = 5.9 \times 10^{-10} \mathcal{L}_{2800}/L_\odot \qquad (6)$$

where $\mathcal{L}_{\rm TIR}$ is the integrated total IR luminosity and $\mathcal{L}_{2800}$ is the rest-frame monochromatic luminosity at 2800 Å (uncorrected for extinction).

We compute $\mathcal{L}_{\rm TIR}$ by integrating the best-fit Draine & Li (2007) dust emission templates between 8 to $1000\,\mu$m. As we mentioned previously, we use four different libraries of dust emission models in our analysis. The main differences between these models are the prominence of the PAHs and their dependence with the total IR luminosity, as well as the ratio between the mass of hot and cold dust. A discussion on these properties is beyond the scope of this paper, nevertheless, we use all these template sets to include the differences between the assumptions made by them in the uncertainty of the total IR luminosity. Therefore, the $\mathcal{L}_{\rm TIR}$ values given in this work are derived from the Draine & Li (2007) libraries, whereas the uncertainties are the RMS of the $\mathcal{L}_{\rm TIR}$ estimations using the 4 template libraries. We have checked that the differences between the luminosities given by the best fitting templates of each library are of the order of $\lesssim 20\%$.

We calculate $\mathcal{L}_{2800}$ interpolating the best fitted optical/NIR empirical template at 2800 Å(rest-frame). This wavelength is covered by observational data over the whole redshift range of interest.

Obviously, this formalism can only be used in the case of galaxies detected in the M/FIR. For those galaxies not detected by MIPS or *Herschel*, we compute $\mathcal{SFR}_{\rm TOT}$ by correcting the UV luminosities (i.e., $\mathcal{SFR}_{\rm UV}$) for dust attenuation ($\mathcal{A}_{\rm UV}$) following the expression

$$\mathcal{SFR}_{\rm TOT} = \mathcal{SFR}_{\rm UV,corr.} = \mathcal{SFR}_{\rm UV} \times 10^{0.4\,\mathcal{A}_{\rm UV}} \qquad (7)$$

where the $\mathcal{SFR}_{\rm UV}$ is obtained using Equation 6.

Meurer et al. (1999) demonstrate that local starburst galaxies exhibit a relatively tight, monotonic relation between the ratio between the UV and the TIR luminosity ($\mathcal{IRX}$) and the UV slope (β[6]). Through this relationship, they derive a relation between the extinction of the UV (in particular, the attenuation at 1600Å) and the β itself, providing a simple relation that can be applied to correct UV luminosities. However, this and other typical attenuation recipes based on the UV slope (e.g., Calzetti et al. 1994) are derived for extreme starburst galaxies, while the sources for which we need the correction (i.e. those not-detected in the M/FIR) are less extreme SFGs. Thus, using those expressions can lead to an overestimation of the extinction and an overcorrection of the UV luminosity. Therefore, we derive an extinction correction optimized for our work (see Appendix B).

In what follows, the values of the $\mathcal{SFR}_{\rm TOT}$ refer to the $\mathcal{SFR}_{\rm UV,corr.}$ (Equation 7, in which we use our own $\mathcal{A}_{\rm UV}$), except in those cases when the M/FIR is available, where

---

[6] The UV continuum slope is defined by assuming that the UV regime of the SED of a galaxy can be described by a power law ($\propto \lambda^\beta$; Calzetti et al. 1994, Meurer et al. 1999).
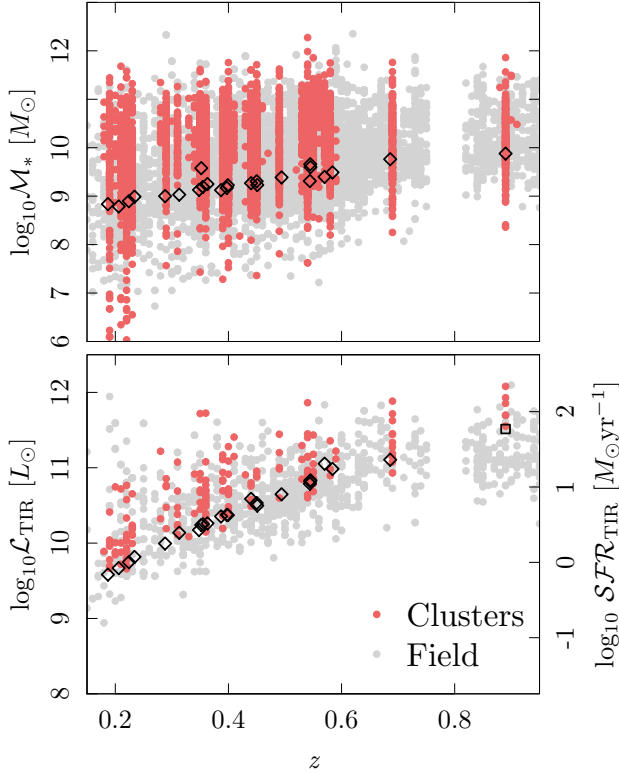
Figure 3. *Top panel*: Distribution of $\mathcal{M}_*$ of the cluster members and field galaxies samples (IRAC 4.5μm 3σ detection) with redshift. The mass limits obtained for each cluster as it is described in the text are marked with black diamonds. *Bottom panel*: Variation with redshift of the total infrared luminosities (left axis) and $\mathcal{SFR}_{\mathrm{TIR}}$ (right axis) of the parent samples of M-FIR detected sources. In the case of the field, we show the sample prior to the $\mathcal{SFR}_{\mathrm{TIR}}$ cuts described in the text. Black symbols indicate the $\mathcal{L}_{\mathrm{TIR}}$ and $\mathcal{SFR}_{\mathrm{TIR}}$ corresponding to the limiting flux of MIPS 24μm (squares) or PACS 100μm (diamonds). For each cluster only the deepest limit is represented. In both panels, red symbols indicate cluster galaxies, grey symbols indicate field galaxies. The number of field galaxies in this plot has been down-sampled to 30% of the original sample size, for visualization purposes.

we consider the addition of the $\mathcal{SFR}_{\mathrm{TIR}}$ and the $\mathcal{SFR}_{\mathrm{UV}}$ (Equation 4).

6   CLUSTER MEMBERS SELECTION

The most unambiguous way to identify cluster members relies on accurate spectroscopic redshifts. However, the acquisition of complete z_{spec} samples remains infeasible except for a relatively small and bright fraction of the galaxy population. Indeed, using photometric redshifts to estimate the distances to galaxies has become a fundamental aim of galaxy surveys conducted during recent years (e.g., Ilbert et al. 2009, Barro et al. 2011b). Although less accurate than spectroscopic ones, photometric redshifts provide a way to estimate distances for galaxies too faint for spectroscopy or samples too large to be practical for complete spectroscopic coverage. Given the incomplete and inhomogeneous spectroscopic coverage of our sample of clusters we are forced to

Table 4. Summary of some of the quantities used for the identification of cluster members and an evaluation of the technique: (1) Cluster ID; (2) number of spectroscopic members as defined by Equation 8; (3) σ_{NMAD} derived for the individual clusters; (4) number of σ_{NMAD} to be used in the integration of the $\mathcal{P}(z)$; (5) membership probability threshold; (6) completeness level (%); (7) fraction of interlopers (%).

ID	#z	σ_{NMAD}	n	$\mathcal{P}_{\mathrm{thr}}$	$\mathcal{K}$	$\mathcal{I}$
(1)	(2)	(3)	(4)	(5)	(6)	(7)
A0383	33	0.02	3	0.30	91	8
A0209	50	0.04	3	0.75	92	7
A0611	21	0.03	3	0.55	95	5
AS1063	71	0.06	1	0.15	87	10
MACS0416	84	0.09	2	0.75	86	13
MACS1206	51	0.06	3	0.85	88	11
RXJ1347	13	0.07	1	0.25	85	13
MACS1149	160	0.12	2	0.85	91	9
MACS0717	83	0.05	3	0.75	89	10
MACS2129	11	0.09	1	0.70	64	27

use criteria to select cluster members based either on z_{spec} or z_{phot}.

The spectroscopic cluster members are identified as those galaxies with z_{spec} within the redshift range defined by the redshift of the cluster, z_{cl}, and its velocity dispersion, σ_{cl}. In Table 1 we show the values we use and the corresponding references. In practice, we use the following criteria (see Cava et al. 2009):

$$|z_{\mathrm{cl}} - z_{\mathrm{spec}}| < 3 \times \sigma_{\mathrm{cl}} \times (1 + z_{\mathrm{cl}}) \qquad (8)$$

For those cases in which a z_{spec} is not available, our member selection relies on the redshift probability distribution, $\mathcal{P}(z)$, given by EAZY instead on the individual z_{phot} associated to each galaxy. This approach captures all the photometric redshift information, which can significantly reduce the impact of the catastrophic errors in the z_{phot}-z_{spec} plane (e.g., Fernández-Soto et al. 2002). This is of key importance to our work, as it translates into a smaller contamination with foreground and background sources in our cluster members selection. In particular, we use the method developed by Pelló et al. (2009) based exclusively on photometric redshift estimates. This approach modifies the technique presented by Brunner & Lubin (2000) in order to take advantage of the $\mathcal{P}(z)$. It calculates a probability of being a cluster member ($\mathcal{P}_{\mathrm{member}}$) integrating $\mathcal{P}(z)$ within a redshift range centred in the redshift of the cluster z_{cl} and with a width (Δz) related to the accuracy of the photometric redshifts (see Section 4.1).

$$\mathcal{P}_{\mathrm{member}} = \int_{z_{\mathrm{cl}}-\Delta z}^{z_{\mathrm{cl}}+\Delta z} \mathcal{P}(z) dz \qquad (9)$$

In our case, we use $\Delta z = n \times \sigma_{\mathrm{NMAD}} \times (1+z_{\mathrm{cl}})$. Applying this technique to those galaxies for which we have a reliable spectroscopic redshift we can calibrate the cluster member selection, which means to find a probability threshold ($\mathcal{P}_{\mathrm{thr}}$) over which a galaxy is considered to be a cluster member, given a certain n. Table 4 shows the values of n and $\mathcal{P}_{\mathrm{thr}}$ we find to maximize the completeness level ($\mathcal{K}$) and minimize the percentage of interlopers ($\mathcal{I}$) for those clusters with spectroscopic members. Table 4 also gives the values of $\mathcal{K}$ and $\mathcal{I}$ for each case. We reach $\mathcal{K}$>80% and $\mathcal{I}$<20% (limiting values used also by Pelló et al. 2009) for 9 out of the 10

clusters with more than 10 spectroscopic cluster members available. In the case of MACS2129, the cluster with fewer spectroscopic members available (11), we retrieve $\mathcal{K}$=64% and $\mathcal{I}$=27%. Still, the members sample we derive for it includes 73% of correct cluster members. For those clusters for which less than 10 spectroscopic redshifts were available, we use the average value of n, and the probability threshold derived for the other individual clusters: n=2, $\mathcal{P}_{\mathrm{thr}}$=0.5. The reader can find examples of the application of a similar selection procedure in the works by (e.g.) Eisenhardt et al. (2008), Vulcani et al. (2011), and Brodwin et al. (2013).

Thorough studies of SED-fitting code performance have identified and quantified their tendency to derive overconfident $\mathcal{P}(z)$. This means that the confidence intervals derived for the z_{phot} are too narrow. Given that we base our photometric cluster members identification on the $\mathcal{P}(z)$ provided by EAZY, we perform a simple check to evaluate the impact of this effect on our work. In practice, we check that the distribution of spectroscopic redshifts in the cluster is comparable with the distribution obtained combining the photometric redshifts $\mathcal{P}(z)$ (Sheth & Rossi 2010). Additionally, we perform the check described by Wittman et al. (2016) through which we find that the overconfidence of the $\mathcal{P}(z)$ we use can be corrected broadening it by applying a convolution with a σ=0.2 gaussian. We have checked that the impact of this effect on our work is negligible in the final selection of cluster members, given that broadening the $\mathcal{P}(z)$ leads to a different calibration of the membership determination method with smaller P_{thr}.

7 CLUSTER MEMBERS & FIELD REFERENCE SAMPLES

The main objective of our study is to compare the SF activity that takes place in the inner region of intermediate redshift clusters with the typical observed in lower density environments (i.e., field). In this section, we describe the different galaxy samples from which we derive the results of this work. In the rest of the article the samples are frequently subdivided in three increasing redshift bins ($0.2<z<0.4$, $0.4<z<0.6$, $0.6<z<0.9$). The two first bins are chosen to have equal number of clusters (11), while the last one includes only the two highest redshift ones. Furthermore, the samples are divided into three cluster-centric distance ($\mathcal{R}$) bins. The first bin ($\mathcal{R}/R_{200}<0.1$) is the only one available across the whole redshift range. The second one ($0.1<\mathcal{R}/R_{200}<0.2$) is visible in the two highest redshift bins. Finally, the third one ($0.2<\mathcal{R}/R_{200}<0.3$) is covered only in the highest redshift clusters. Table 5, 6, and 7 show the number counts and average properties of the various galaxy clusters subsamples. Table 8 displays the number counts and average properties of field galaxy samples.

7.1 Samples of cluster members

For each CLASH+HLS field, we build a general *cluster members sample* out of the previously described CLASH parent catalogues. We consider only sources with a $>3\sigma$ detection in IRAC 4.5μm band to avoid spurious and extremely faint systems, and fluxes larger than the average limiting fluxes

at 3σ level (see Table 3 for the limiting fluxes at 5σ detection level). Using the methodology described in Section 6, we select a total of 3121 cluster members distributed into the 24 clusters analysed. This number does not include the 259 galaxies for which the SED-fitting is not able to derive an accurate value of mass: those sources fitted with a template of an active galaxy and sources with fewer than 4 photometric data points.

Figure 3 represents the distribution with redshift of the $\mathcal{M}_*$ estimations derived through the SED-fitting (Section 5) for the cluster members parent sample. We also represent the $\mathcal{M}_*$ limits given the 3σ IRAC 4.5μm limit fluxes for each cluster (see Table 3). This conservative estimations are performed using the same set of templates described in Section 5 with solar metallicity, $\tau = 1\,\mathrm{Myr}$, and an age that corresponds to the age of the Universe at each redshift.

To create comparable galaxy samples at different redshifts, we focus our analysis on cluster members with $\log_{10}\mathcal{M}_*/M_\odot$>10. Our final cluster members sample contain 1518 galaxies.

We have performed a comparison between the cluster members we select using our approach and the members catalogues published by Connor et al. (2017) for all CLASH clusters. On average, 90^{+3}_{-7}% of the galaxies with $\log_{10}\mathcal{M}_*/M_\odot$>10 in each of our samples have a counterpart in their general catalogues. Among them, 87^{+9}_{-8}% are also considered cluster members by Connor et al. (2017). Finally, only a 6^{+14}_{-4}% of galaxies included in the cluster members catalogues of their publication are not included in our cluster members samples. Therefore, in this range of stellar masses the differences are within our estimated levels of completeness and contamination.

7.2 Samples of field galaxies

In order to build a reference sample to which compare the properties of the cluster members, we make use of the outstanding datasets available on three of the CANDELS fields (Grogin et al. 2011, Koekemoer et al. 2011). In particular, we focus on both the GOODS fields (Giavalisco et al. 2004; see Sections A1, A2) and COSMOS (Scoville et al. 2007; see Section A3).

Using an analogous approach to that described in Sections 3, 4, and 5, we create multi-wavelength catalogues and derive the photometric redshifts and physical properties (e.g., $\mathcal{M}_*$, $\mathcal{SFR}$) of the galaxies in CANDELS catalogues. Then, we apply the same spectroscopic and photometric redshift criteria to select a *field sample* corresponding to each cluster members sample in terms of redshift range. Then, for each field sample, we select only the galaxies with a $>3\sigma$ detection in IRAC 4.5μm band and a IRAC 4.5μm flux larger than the 3σ detection limit of each corresponding cluster sample. Figure 3 represents the distribution of the field samples in the $\mathcal{M}_*$-z plane.

The final field parent sample contains 7466 systems with $\log_{10}\mathcal{M}_*/M_\odot$>10. We exclude the 360 galaxies without a robust mass estimation (see previous section).

7.3 Samples of star-forming and passive galaxies

We divide the samples of field and cluster galaxies into star-forming and passive using the rest-frame $U-V$ *vs* $V-J$
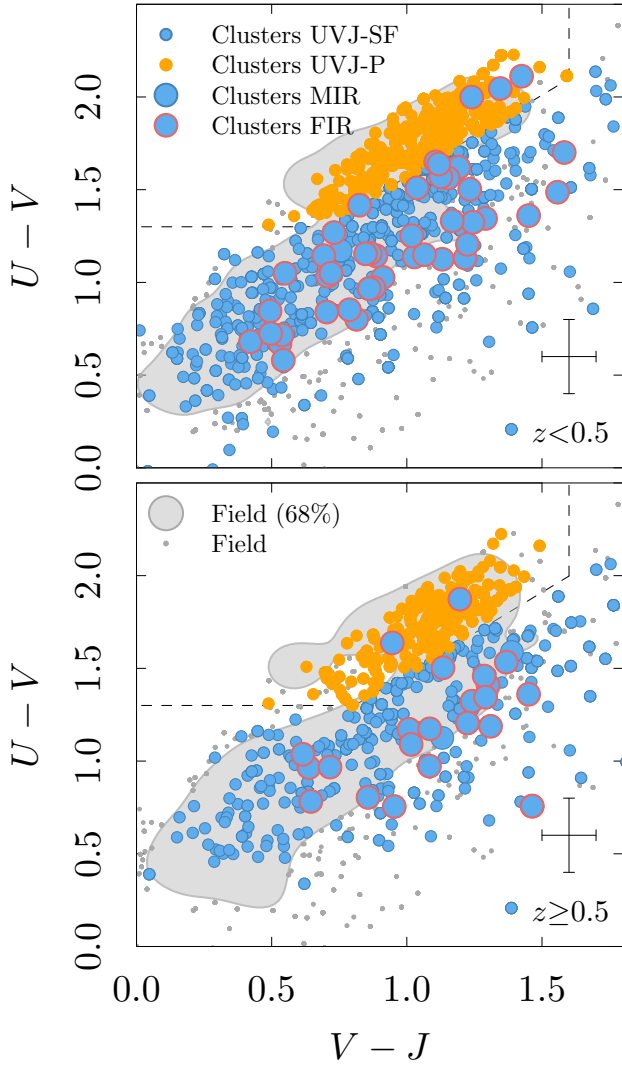
Figure 4. UVJ-diagram for the cluster members (circles) and field galaxies (grey contours and points) in two redshift bins (top panel $0<z<0.5$; bottom panel, $0.5<z<1.0$). Dashed lines mark the corresponding boundaries defined by Williams et al. (2009) to distinguish between quiescent and SFGs. The circles that represent those cluster members within the locus of the passive (star-forming) galaxies are coloured in orange (blue). The cluster members detected in the FIR are highlighted with larger blue circles and a red border.

Figure 5. $s\mathcal{SFR}_{\rm TOT}$ vs. $\mathcal{M}_*$ for the star-forming cluster members (blue points) and field galaxies (grey contours and points) in the two redshift bins in Figure 4. The cluster members detected in the FIR are highlighted with larger blue circles and a red border. The black lines represent the MS by Renzini & Peng (2015) scaled to the median redshift of the corresponding bin considering an evolution with redshift of the $s\mathcal{SFR}$ of the shape $(1+z)^{2.8\pm0.1}$ (Sargent et al. 2012).

colour-colour space (hereafter, UVJ-diagram). Different works (e.g., Wuyts et al. 2007, Williams et al. 2009) have evidenced the power of the UVJ-diagram to select *pure* samples of either quiescent and SFGs (e.g., Wuyts et al. 2007, Brammer et al. 2011, Whitaker et al. 2012a, Whitaker et al. 2015). In particular, we identify passive galaxies (hearafter, UVJ-P) following the recipes by Williams et al. (2009) for the redshift bins $0<z<0.5$ ($U-V>0.88\times V-J+0.69$, $U-V>1.3$, and $V-J<1.6$) and $0.5<z<1.0$ ($U-V>0.88\times V-J+0.59$, $U-V>1.3$, and $V-J<1.6$). Galaxies with rest-frame $U-V$ and $V-J$ behaving otherwise are classified as star-forming (hereafter, UVJ-SF). We perform Monte Carlo simulations to assess the reciprocal contamination between the two types
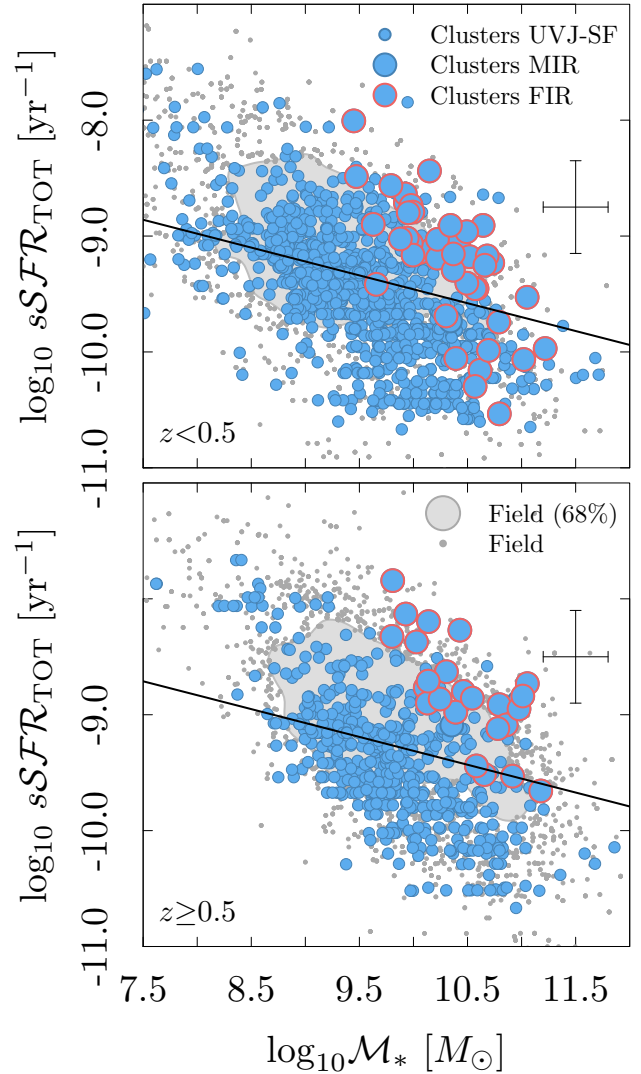
of galaxies considering the uncertainties in the synthetic photometry. We retrieve $\leq 1\%$ differences in the number counts of either category and sample. We find that in the clusters (field) samples, 25% (5%) of SFGs could be classified as passive given their error bars and 28% (22%) of passive galaxies could be classified as SFGs. We have checked that excluding the galaxies in the vicinities of the limits between the UVJ-P and the UVJ-SF loci do not change the results of our work significantly. This is probably due to the fact that these *transition* galaxies present similar properties on either side of the border.

In Figure 4, we show the UVJ-diagram for the cluster and field samples. As we can see, some galaxies detected in the FIR (i.e., presumably SFGs) are located in the region
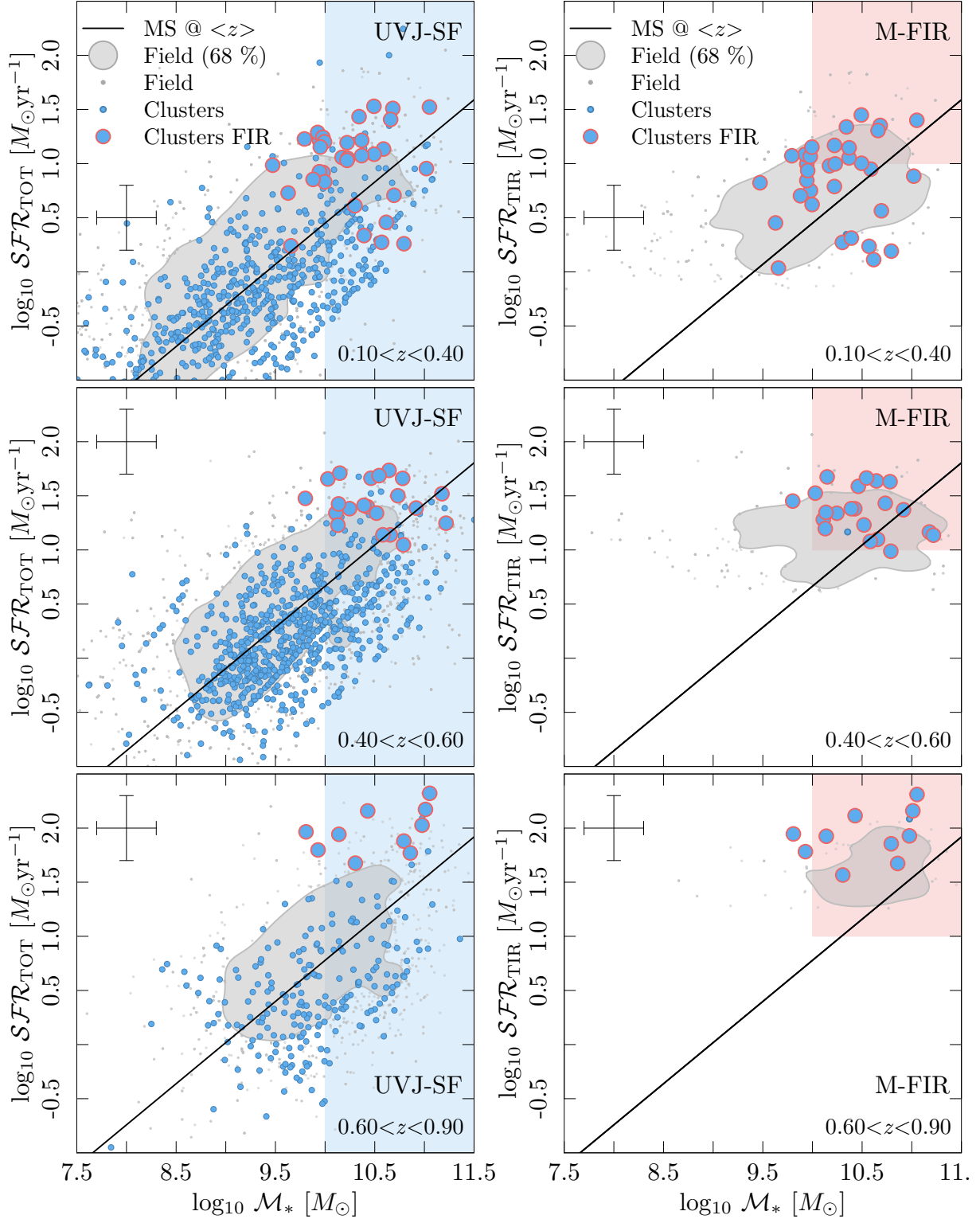
Figure 6. $\mathcal{SFR}_{\rm TOT}$ *vs* $\mathcal{M}_*$ relation for the star-forming cluster members in our study split up in three increasing z bins (top, middle, and bottom panels). On the (left-) right-hand panels, we include the (UVJ-SF) M-FIR galaxies across the whole mass range. The $\mathcal{SFR}_{\rm TOT}$ refers to the $\mathcal{SFR}_{\rm TIR}+\mathcal{SFR}_{\rm UV}$ for those galaxies M-FIR detected, and $\mathcal{SFR}_{UV,corr}$ otherwise. Blue points always represent the distribution of clusters members in both cases. Those galaxies detected in the FIR (i.e., *Herschel*) are shown with larger blue points highlighted with red borders. grey contours represent the distribution (68 confidence levels) of field galaxies. We also display the MS by Renzini & Peng (2015, black lines) scaled to the median redshift of the corresponding subsample of cluster members considering a trend of $s\mathcal{SFR}$ with redshift $\propto (1+z)^{2.8\pm0.1}$ (Sargent et al. 2012). The shaded areas represent the selection criteria used to build the final samples of UVJ-SF and M-FIR galaxies (i.e. they represent the cut in $\mathcal{M}_*$, and $\mathcal{SFR}_{\rm TIR}$).

	RGB	F814W	F160W	IRAC 3.6	IRAC 4.5	MIPS 24	PACS 100	PACS 160	SPIRE 250	SPIRE 350	SPIRE 500

CLASH0000032 A0383 0.190 $z_{\rm spec}$

CLASH0001653 A0209 0.210 $z_{\rm spec}$

CLASH0001783 A0209 0.200 $z_{\rm spec}$

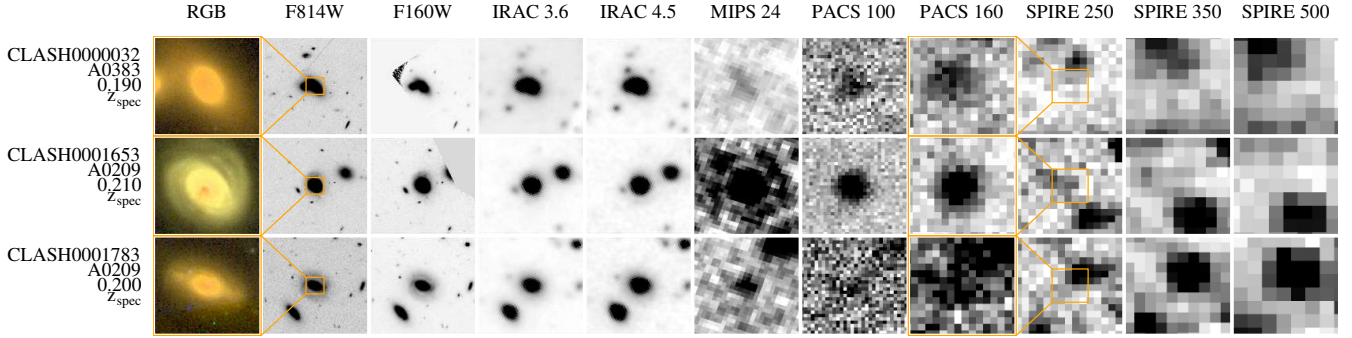**Figure 7.** Thumbnails of 3 cluster members from the M-FIR sample ordered by increasing redshift. From left to right we display a RGB image (5"×5") created using *HST*/ACS/F814W, F606W, and F435W, following the methodology by Lupton et al. (2004), 30"×30" postage stamps in the *HST*/ACS/F814W and *HST*/WFC3/F160W bands followed by *Spitzer*/IRAC and MIPS, and *Herschel*/PACS bands, and 90"×90" postage stamps in the *Herschel*/SPIRE bands, all ordered by increasing wavelength. When there is a difference in the sizes of two adjacent frames, we mark with an orange square the size of the smallest on the largest. On the left side we show the ID of the object, the name of the cluster, the redshift and either if it is photometric or spectroscopic. The thumbnails of the rest of the sample can be found as online material.

theoretically populated by passive galaxies. This contamination has been reported in the past (see, e.g., Domínguez Sánchez et al. 2016) and evidences the necessity of a correction of the aforementioned selection criteria. In the final UVJ-SF (UVJ-P) samples, we include (exclude) both the galaxies located in the SFGs locus of the UVJ-diagram and those detected in the M/FIR (see Section 7.4) independently of their position in the UVJ-diagram. This correction increases (decreases) 1% (1%) and 2% (5%) the number of star-forming (passive) galaxies in the cluster and field samples, respectively.

The UVJ-SF (UVJ-P) samples built in CLASH-HLS clusters and the field include 443 (1075) and 4649 (2817) $\log_{10}\mathcal{M}_*/M_\odot > 10$ galaxies, respectively.

An alternative methodology to select SFGs uses a threshold of $s\mathcal{SFR}$ under which a galaxy is considered to be passive (e.g., Kimm et al. 2009). In Figure 5, we represent the $s\mathcal{SFR}_{\rm TOT}$-$\mathcal{M}_*$ diagrams for the UVJ-SF samples in the redshift bins of Figure 4. We can see that our UVJ-SF selection criteria corresponds approximately to $\log_{10} s\mathcal{SFR}_{\rm TOT}/{\rm yr}^{-1} \gtrsim -10.5$.

On the left-hand half of Figure 6, we display the distribution of the UVJ-SF samples selected in the clusters and the field on the $\mathcal{SFR}_{\rm TOT}$-$\mathcal{M}_*$ plane. The blue shaded area illustrates the effective definition of the UVJ-SF samples considered in the rest of the work. For comparison, we also represent the MS defined by Renzini & Peng (2015, black line) scaled to the median redshift of the bin, assuming and evolution with redshift of the $s\mathcal{SFR}$ of the shape $(1 + z)^{2.8\pm0.1}$ (Sargent et al. 2012). We notice a systematic offset of the distribution of cluster SFGs towards lower $\mathcal{SFR}$ at fixed $\mathcal{M}_*$ (see also Figure 5). The quantification of this difference can be found in Section 9.3.

7.4 Samples of M- and/or FIR-detected galaxies

In order to build comparable samples of galaxies ($\log_{10}\mathcal{M}_*/M_\odot > 10$) detected in the M- and/or FIR (M-FIR samples), we perform the following steps. First, we select galaxies with at least a 3σ detection in one of the M- and/or

FIR bands available (i.e., MIPS 24μm, PACS 100 & 160μm, and SPIRE 250, 350 & 500μm), and flux larger than the limiting fluxes at 3σ level in the clusters (see Table 3 for the limiting fluxes at 5σ detection level). These galaxies are represented in the bottom panel of Figure 3. Then, we select only the 50 (1496) clusters (field) galaxies for which the estimated $\mathcal{SFR}_{TIR}$ is larger than the (conservative) $\mathcal{SFR}_{\rm TIR}$ limits obtained for each cluster (black symbols in the bottom panel of Figure 3). Figure 7 shows the thumbnails of the cluster members detected in the M- and/or FIR. Finally, we consider galaxies with $\mathcal{SFR}_{\rm TIR} > 10 M_\odot yr^{-1}$ to obtain a comparable set of samples of galaxies throughout the whole redshift range. This value is larger than the $\mathcal{SFR}_{\rm TIR}$ limits of our sample, except for the four furthest clusters. Our final *M-FIR samples* include 36 cluster members and 974 field galaxies. On the right-hand half of Figure 6, we display the distribution of these samples on the $\mathcal{SFR}_{\rm TIR}$-$\mathcal{M}_*$ plane. The red shaded area marks the $\mathcal{M}_*$ and $\mathcal{SFR}_{\rm TIR}$ cuts performed to define the samples.

It is worth mentioning that we perform a visual inspection of each cluster member selected as a M-FIR emitter. We exclude spurious MIPS 24μm sources without a counterpart in longer wavelengths (e.g., sources on Airy ring features), galaxies in the borders of the images that are selected as counterparts of M/FIR sources with coordinates outside the area covered by CLASH catalogues, or galaxies suffering from over-deblending in the CLASH catalogues.

Interestingly, we find 8 BCGs detected in the M/FIR out of 24 clusters, which corresponds to 33% of our sample. This percentage is consistent with the results of the study conducted by Rawle et al. (2012a) using HLS data on a sample of 68 massive galaxy clusters spread out in the redshift range between $0.08 < z < 1.00$. Their sample includes only 12 CLASH+HLS clusters. As expected, among the BCGs of these 12 systems, we detect traces of obscured SF in the same two, namely A0383 and MACS1423. We exclude BCGs from our samples given their unique SFH and in order to focus our results on the SF activity of the general cluster galaxy population.

The fraction of active galactic nuclei (AGN) among IR-

bright cluster members has been observed to increase rapidly from 3% up to 65% for galaxies with increasing $\mathcal{L}_{\mathrm{TIR}}$ values varying from $10^{11} L_\odot$ to $>10^{11.6} L_\odot$ in clusters within the redshift range $0.15 < z < 0.30$ (Haines et al. 2013). Given the SED-fitting methodology explained and sample selection, we exclude from our analysis the galaxies whose photometry was fitted to AGN templates.

The so-called luminous and ultra-luminous infrared galaxies (LIRGs and ULIRGs, respectively) display $\mathcal{L}_{\mathrm{TIR}}$ in the range of $10^{11} L_\odot < \mathcal{L}_{\mathrm{TIR}} < 10^{12} L_\odot$ and $\mathcal{L}_{\mathrm{TIR}} > 10^{12} L_\odot$, respectively, which correspond to $\mathcal{SFR}_{\mathrm{TIR}}$ from tens to thousands of $M_\odot \mathrm{yr}^{-1}$. Our M-FIR sample of cluster members includes 25 LIRGs and 1 ULIRGs (within CLJ1226, the highest redshift cluster) and our M-FIR sample of field galaxies includes 639 LIRGs, and 10 ULIRGs. These numbers correspond to comparable percentages of LIRGs and ULIRGs within the M-FIR samples in clusters and field.

Table 5. Number of galaxies selected with the different criteria used to build the final samples of star-forming cluster members ($\mathcal{R}/R_{200}<0.1$), and average SF activity indicators. In particular, we report: (1) ID of the corresponding field; (2) number of cluster members with a detection at a level $>3\sigma$ in IRAC 4.5μm and $\mathcal{M}_* > 10^{10}\mathrm{M}_\odot$; we show within parentheses the number of cluster members without the $\mathcal{M}_*$ cut; (3) number of galaxies selected as star-forming using the UVJ diagram and/or detected in the MIR and/or FIR ($\mathcal{M}_* > 10^{10}\mathrm{M}_\odot$), what we call the *UVJ-SF sample*; (4) cluster members with $\mathcal{M}_* > 10^{10}\mathrm{M}_\odot$ detected in the MIR and/or FIR with a $\mathcal{SFR}_\mathrm{TIR} >10\mathrm{M}_\odot\mathrm{yr}^{-1}$, what we call *M-FIR sample*; we show the total number without $\mathcal{SFR}_\mathrm{TIR}$ cut within parentheses; (5 & 6) fraction of *UVJ-SF* and M-FIR galaxies, respectively, obtained using as reference the number of cluster members with $\mathcal{M}_* > 10^{10}\mathrm{M}_\odot$; (7 & 8) median and quantiles 16$^\mathrm{th}$ and 84$^\mathrm{th}$ values of the $\mathcal{M}_*$ of the *UVJ-SF* and M-FIR samples respectively; (9) median and quantiles 16$^\mathrm{th}$ and 84$^\mathrm{th}$ values of the $\mathcal{SFR}_\mathrm{TOT}$ for the *UVJ-SF* sample obtained as the addition of the $\mathcal{SFR}_\mathrm{TIR}$ and the $\mathcal{SFR}_\mathrm{UV}$ when the former is available, and the $\mathcal{SFR}_\mathrm{UV,corr}$ in the rest of the cases; (10) median and quantiles 16$^\mathrm{th}$ and 84$^\mathrm{th}$ values of the $\mathcal{SFR}_\mathrm{TOT}$ for the M-FIR sample obtained as the addition of the $\mathcal{SFR}_\mathrm{TIR}$ and the $\mathcal{SFR}_\mathrm{UV}$; (11 & 12) median and quantiles 16$^\mathrm{th}$ and 84$^\mathrm{th}$ values of the $s\mathcal{SFR}_\mathrm{TOT}$ for the *UVJ-SF* and the M-FIR sample, respectively.

Cluster ID (1)	Members (2)	UVJ-SF (3)	M-FIR (4)	$\mathcal{F}_{UVJ-\mathrm{SF}}$ (5)	$\mathcal{F}_{\mathrm{M-FIR}}$ (6)	$\mathcal{M}_{*,UVJ-SF}$ (7)	$\mathcal{M}_{*,\mathrm{M-FIR}}$ (8)	$\mathcal{SFR}_{\mathrm{TOT},UVJ-SF}$ (9)	$\mathcal{SFR}_{\mathrm{TOT,M-FIR}}$ (10)	$s\mathcal{SFR}_{\mathrm{TOT},UVJ-SF}$ (11)	$s\mathcal{SFR}_{\mathrm{TOT,M-FIR}}$ (12)
a0383	11 (53)	2	0 (0)	0.17±0.11	–	$10.70^{+0.13}_{-0.12}$	–	$0.46^{+0.12}_{-0.11}$	–	$-10.24^{+0.01}_{-0.01}$	–
a0209	23 (72)	8	0 (1)	0.35±0.10	–	$10.65^{+0.39}_{-0.24}$	–	$0.68^{+0.43}_{-0.40}$	–	$-10.19^{+0.31}_{-0.09}$	–
a2261	30 (192)	7	0 (3)	0.23±0.08	–	$10.23^{+0.11}_{-0.02}$	–	$0.55^{+0.06}_{-0.24}$	–	$-9.73^{+0.06}_{-0.33}$	–
rbs1748	14 (48)	5	0 (0)	0.36±0.13	–	$10.28^{+0.13}_{-0.12}$	–	$0.06^{+0.14}_{-0.10}$	–	$-10.25^{+0.10}_{-0.04}$	–
a0611	18 (34)	6	0 (0)	0.33±0.11	–	$10.24^{+0.25}_{-0.13}$	–	$0.48^{+0.42}_{-0.55}$	–	$-9.85^{+0.61}_{-0.46}$	–
ms2137	6 (11)	2	0 (0)	0.33±0.19	–	$10.28^{+0.03}_{-0.03}$	–	$-0.18^{+0.02}_{-0.02}$	–	$-10.46^{+0.01}_{-0.01}$	–
as1063	28 (48)	15	1 (1)	0.54±0.09	0.04±0.04	$10.45^{+0.16}_{-0.23}$	10.37^{--}_{--}	$0.11^{+1.01}_{-0.31}$	1.21^{--}_{--}	$-10.29^{+0.59}_{-0.19}$	-9.15^{--}_{--}
macs1931	22 (47)	8	0 (0)	0.36±0.10	–	$10.25^{+0.37}_{-0.12}$	–	$0.48^{+0.70}_{-0.66}$	–	$-9.71^{+0.39}_{-0.72}$	–
macs1115	18 (31)	4	0 (0)	0.22±0.10	–	$10.31^{+0.14}_{-0.10}$	–	$0.01^{+0.24}_{-0.13}$	–	$-10.32^{+0.26}_{-0.15}$	–
rxj1532	14 (28)	4	0 (0)	0.29±0.12	–	$10.46^{+0.29}_{-0.28}$	–	$0.53^{+0.91}_{-0.29}$	–	$-9.89^{+0.82}_{-0.30}$	–
macs1720	15 (37)	4	0 (0)	0.27±0.11	–	$10.47^{+0.37}_{-0.32}$	–	$0.62^{+0.32}_{-0.24}$	–	$-9.83^{+0.06}_{-0.08}$	–
macs0416	34 (53)	12	1 (1)	0.35±0.08	0.03±0.03	$10.35^{+0.21}_{-0.18}$	10.43^{--}_{--}	$0.55^{+0.16}_{-0.20}$	1.40^{--}_{--}	$-9.85^{+0.12}_{-0.10}$	-9.03^{--}_{--}
macs0429	8 (21)	4	0 (0)	0.50±0.18	–	$10.42^{+0.50}_{-0.07}$	–	$0.86^{+0.45}_{-0.49}$	–	$-9.98^{+0.49}_{-0.09}$	–
macs1206	35 (73)	15	1 (1)	0.43±0.08	0.03±0.03	$10.52^{+0.09}_{-0.35}$	11.22^{--}_{--}	$0.67^{+0.45}_{-0.36}$	1.25^{--}_{--}	$-9.84^{+0.38}_{-0.39}$	-9.97^{--}_{--}
macs0329	13 (34)	8	0 (0)	0.62±0.13	–	$10.47^{+0.10}_{-0.22}$	–	$0.54^{+0.33}_{-0.19}$	–	$-9.88^{+0.22}_{-0.11}$	–
rxj1347	28 (44)	12	0 (0)	0.43±0.09	–	$10.27^{+0.62}_{-0.14}$	–	$0.32^{+0.62}_{-0.31}$	–	$-9.93^{+0.08}_{-0.35}$	–
macs1311	22 (42)	8	1 (1)	0.36±0.10	0.05±0.04	$10.40^{+0.12}_{-0.28}$	10.52^{--}_{--}	$0.68^{+0.61}_{-0.41}$	1.34^{--}_{--}	$-9.85^{+0.72}_{-0.42}$	-9.18^{--}_{--}
macs1149	42 (82)	20	0 (0)	0.48±0.08	–	$10.52^{+0.24}_{-0.26}$	–	$0.47^{+0.66}_{-0.46}$	–	$-9.92^{+0.29}_{-0.56}$	–
macs0717	57 (72)	8	0 (0)	0.14±0.05	–	$10.32^{+0.34}_{-0.28}$	–	$0.35^{+0.14}_{-0.14}$	–	$-9.97^{+0.28}_{-0.49}$	–
macs1423	26 (30)	7	1 (1)	0.27±0.09	0.04±0.04	$10.47^{+0.72}_{-0.31}$	10.78^{--}_{--}	$0.54^{+1.13}_{-0.45}$	1.66^{--}_{--}	$-10.00^{+0.27}_{-0.10}$	-9.12^{--}_{--}
macs2129	17 (18)	4	1 (1)	0.24±0.10	0.06±0.06	$10.24^{+0.27}_{-0.17}$	10.14^{--}_{--}	$0.58^{+0.56}_{-0.33}$	1.43^{--}_{--}	$-9.75^{+0.58}_{-0.26}$	-8.71^{--}_{--}
macs0647	17 (24)	7	0 (0)	0.41±0.12	–	$10.82^{+0.27}_{-0.58}$	–	$0.63^{+0.76}_{-0.09}$	–	$-10.08^{+0.45}_{-0.13}$	–
macs0744	20 (37)	9	0 (0)	0.45±0.11	–	$10.69^{+0.11}_{-0.30}$	–	$0.68^{+0.79}_{-0.09}$	–	$-9.76^{+0.57}_{-0.37}$	–
clj1226	33 (57)	18	0 (0)	0.55±0.09	–	$10.45^{+0.34}_{-0.39}$	–	$0.49^{+0.31}_{-0.28}$	–	$-10.08^{+0.34}_{-0.16}$	–
Total	551 (1188)	197	6 (10)								
Median		$0.2<z<0.4$ $\mathcal{R}/R_{200}<0.1$		$0.33^{+0.03}_{-0.10}$	–	$10.30^{+0.15}_{-0.03}$	10.37^{--}_{--}	$0.49^{+0.05}_{-0.37}$	1.21^{--}_{--}	$-10.19^{+0.34}_{-0.06}$	-9.15^{--}_{--}
		$0.4<z<0.6$ $\mathcal{R}/R_{200}<0.1$		$0.41^{+0.07}_{-0.16}$	$0.00^{+0.04}_{-0.00}$	$10.42^{+0.05}_{-0.02}$	$10.52^{+0.26}_{-0.09}$	$0.55^{+0.08}_{-0.01}$	$1.40^{+0.03}_{-0.06}$	$-9.93^{+0.08}_{-0.04}$	$-9.12^{+0.10}_{-0.06}$
		$0.6<z<0.9$ $\mathcal{R}/R_{200}<0.1$		$0.50^{+0.03}_{-0.03}$	–	$10.57^{+0.12}_{-0.12}$	–	$0.58^{+0.09}_{-0.09}$	–	$-9.92^{+0.16}_{-0.16}$	–

Table 6. As in Table 5, for the galaxies at $0.1<\mathcal{R}/R_{200}<0.2$.

Cluster ID (1)	Members (2)	UVJ-SF (3)	M-FIR (4)	$\mathcal{F}_{UVJ-\mathrm{SF}}$ (5)	$\mathcal{F}_{\mathrm{M-FIR}}$ (6)	$\mathcal{M}_{*,\,UVJ-\mathrm{SF}}$ (7)	$\mathcal{M}_{*,\,\mathrm{M-FIR}}$ (8)	$\mathcal{SFR}_{\mathrm{TOT},UVJ-\mathrm{SF}}$ (9)	$\mathcal{SFR}_{\mathrm{TOT,M-FIR}}$ (10)	$s\mathcal{SFR}_{\mathrm{TOT},UVJ-\mathrm{SF}}$ (11)	$s\mathcal{SFR}_{\mathrm{TOT,M-FIR}}$ (12)
a0383	10 (55)	1	0 (0)	0.10 ± 0.09	–	10.09_{--}	–	-0.19_{--}	–	-10.28_{--}	–
a0209	3 (20)	1	0 (1)	0.33 ± 0.27	–	10.59_{--}	–	1.13_{--}	–	-9.45_{--}	–
a2261	22 (140)	5	0 (1)	0.23 ± 0.09	–	$10.69^{+0.14}_{-0.37}$	–	$0.51^{+0.21}_{-0.36}$	–	$-10.22^{+0.21}_{-0.03}$	–
rbs1748	12 (53)	1	0 (1)	0.08 ± 0.08	–	11.02_{--}	–	0.95_{--}	–	-10.07_{--}	–
a0611	30 (64)	7	1 (2)	0.23 ± 0.08	0.03 ± 0.03	$10.37^{+0.09}_{-0.15}$	10.49_{--}	$0.59^{+0.48}_{-0.40}$	1.53_{--}	$-9.81^{+0.64}_{-0.46}$	-8.96_{--}
ms2137	13 (25)	3	1 (1)	0.23 ± 0.12	0.08 ± 0.07	$10.22^{+0.30}_{-0.12}$	10.66_{--}	$0.27^{+0.78}_{-0.14}$	1.41_{--}	$-9.95^{+0.47}_{-0.02}$	-9.25_{--}
as1063	24 (48)	6	0 (0)	0.25 ± 0.09	–	$10.35^{+0.13}_{-0.29}$	–	$-0.14^{+0.13}_{-0.21}$	–	$-10.47^{+0.04}_{-0.05}$	–
macs1931	27 (56)	3	0 (0)	0.11 ± 0.06	–	$10.38^{+0.12}_{-0.09}$	–	$0.24^{+0.14}_{-0.15}$	–	$-10.32^{+0.35}_{-0.02}$	–
macs1115	23 (54)	9	1 (1)	0.39 ± 0.10	0.04 ± 0.04	$10.41^{+0.33}_{-0.22}$	10.49_{--}	$0.76^{+0.29}_{-0.33}$	1.09_{--}	$-9.80^{+0.58}_{-0.29}$	-9.41_{--}
rxj1532	12 (31)	1	0 (1)	0.08 ± 0.08	–	10.22_{--}	–	1.03_{--}	–	-9.19_{--}	–
macs1720	26 (65)	8	1 (1)	0.31 ± 0.09	0.04 ± 0.04	$10.21^{+0.13}_{-0.28}$	11.05_{--}	$0.36^{+0.25}_{-0.40}$	1.52_{--}	$-9.83^{+0.24}_{-0.33}$	-9.53_{--}
macs0416	24 (63)	5	1 (1)	0.21 ± 0.08	0.04 ± 0.04	$10.64^{+0.25}_{-0.28}$	10.64_{--}	$0.74^{+0.62}_{-0.20}$	1.74_{--}	$-9.96^{+0.82}_{-0.19}$	-8.91_{--}
macs0429	12 (41)	5	0 (1)	0.42 ± 0.14	–	$10.51^{+0.14}_{-0.28}$	–	$0.04^{+0.41}_{-0.13}$	–	$-10.55^{+0.57}_{-0.01}$	–
macs1206	42 (86)	9	0 (0)	0.21 ± 0.06	–	$10.16^{+0.37}_{-0.12}$	–	$0.18^{+0.42}_{-0.38}$	–	$-10.08^{+0.43}_{-0.36}$	–
macs0329	27 (59)	6	0 (0)	0.22 ± 0.08	–	$10.28^{+0.13}_{-0.11}$	–	$0.37^{+0.35}_{-0.26}$	–	$-10.03^{+0.45}_{-0.13}$	–
rxj1347	29 (67)	2	0 (0)	0.07 ± 0.05	–	$10.67^{+0.38}_{-0.38}$	–	$1.19^{+0.16}_{-0.17}$	–	$-9.48^{+0.54}_{-0.55}$	–
macs1311	27 (61)	8	2 (2)	0.30 ± 0.09	0.07 ± 0.05	$10.33^{+0.32}_{-0.19}$	$10.44^{+0.20}_{-0.20}$	$1.04^{+0.44}_{-1.02}$	$1.61^{+0.07}_{-0.08}$	$-9.54^{+0.73}_{-0.78}$	$-8.84^{+0.27}_{-0.27}$
macs1149	70 (158)	16	3 (3)	0.23 ± 0.05	0.04 ± 0.02	$10.30^{+0.38}_{-0.15}$	$10.25^{+0.45}_{-0.08}$	$0.65^{+0.71}_{-0.36}$	$1.38^{+0.01}_{-0.10}$	$-9.67^{+0.66}_{-0.31}$	$-8.90^{+0.02}_{-0.43}$
macs0717	80 (107)	15	6 (6)	0.19 ± 0.04	0.07 ± 0.03	$10.45^{+0.47}_{-0.29}$	$10.47^{+0.29}_{-0.38}$	$1.14^{+0.24}_{-0.40}$	$1.30^{+0.25}_{-0.16}$	$-9.52^{+0.48}_{-0.42}$	$-9.27^{+0.58}_{-0.27}$
macs1423	17 (29)	2	0 (0)	0.12 ± 0.08	–	$10.07^{+0.04}_{-0.05}$	–	$0.57^{+0.13}_{-0.12}$	–	$-9.49^{+0.07}_{-0.08}$	–
macs2129	33 (38)	1	0 (0)	0.03 ± 0.03	–	10.21_{--}	–	0.94_{--}	–	-9.27_{--}	–
macs0647	27 (54)	14	1 (1)	0.52 ± 0.10	0.04 ± 0.04	$10.30^{+0.24}_{-0.22}$	10.46_{--}	$0.70^{+0.68}_{-0.18}$	1.66_{--}	$-9.50^{+0.33}_{-0.32}$	-8.80_{--}
macs0744	33 (56)	6	0 (0)	0.18 ± 0.07	–	$10.66^{+0.29}_{-0.33}$	–	$0.91^{+0.12}_{-0.02}$	–	$-9.75^{+0.53}_{-0.26}$	–
clj1226	38 (60)	15	0 (0)	0.39 ± 0.08	–	$10.32^{+0.26}_{-0.18}$	–	$0.46^{+0.46}_{-0.18}$	–	$-9.80^{+0.28}_{-0.25}$	–
Total	661 (1490)	149	17 (23)								
Median	$0.4<z<0.6$	$0.1<\mathcal{R}/R_{200}<0.2$		$0.21^{+0.12}_{-0.13}$	$0.00^{+0.05}_{-0.00}$	$10.30^{+0.15}_{-0.02}$	$10.46^{+0.01}_{-0.02}$	$0.70^{+0.24}_{-0.12}$	$1.61^{+0.06}_{-0.22}$	$-9.54^{+0.04}_{-0.42}$	$-8.90^{+0.06}_{-0.01}$
	$0.6<z<0.9$	$0.1<\mathcal{R}/R_{200}<0.2$		$0.29^{+0.07}_{-0.07}$	–	$10.49^{+0.17}_{-0.17}$	–	$0.68^{+0.23}_{-0.23}$	–	$-9.78^{+0.02}_{-0.02}$	–

Table 7. As in Table 5, for the galaxies at $0.2<\mathcal{R}/R_{200}<0.3$.

Cluster ID (1)	Members (2)	UVJ-SF (3)	M-FIR (4)	$\mathcal{F}_{UVJ-SF}$ (5)	$\mathcal{F}_{M-FIR}$ (6)	$\mathcal{M}_{*,UVJ-SF}$ (7)	$\mathcal{M}_{*,M-FIR}$ (8)	$\mathcal{SFR}_{TOT,UVJ-SF}$ (9)	$\mathcal{SFR}_{TOT,M-FIR}$ (10)	$s\mathcal{SFR}_{TOT,UVJ-SF}$ (11)	$s\mathcal{SFR}_{TOT,M-FIR}$ (12)
a0383	6 (14)	1	0 (1)	0.17±0.15	–	10.79^{--}_{--}	–	$0.26^{+0.00}_{-0.01}$	–	-10.53^{--}_{--}	–
a0209	0 (0)	0	0 (0)	–	–	–	–	–	–	–	–
a2261	0 (0)	0	0 (0)	–	–	–	–	–	–	–	–
rbs1748	0 (0)	0	0 (0)	–	–	–	–	–	–	–	–
a0611	5 (11)	2	0 (1)	0.40±0.22	–	$10.16^{+0.01}_{-0.00}$	–	$0.69^{+0.25}_{-0.26}$	–	$-9.48^{+0.25}_{-0.25}$	–
ms2137	10 (24)	1	0 (1)	0.10±0.09	–	10.07^{--}_{--}	–	1.13^{--}_{--}	–	-8.94^{--}_{--}	–
as1063	5 (10)	2	0 (0)	0.40±0.22	–	$10.64^{+0.30}_{-0.29}$	–	$0.31^{+0.37}_{-0.37}$	–	$-10.34^{+0.08}_{-0.07}$	–
macs1931	18 (33)	4	0 (0)	0.22±0.10	–	$10.18^{+0.08}_{-0.10}$	–	$0.19^{+0.34}_{-0.20}$	–	$-9.99^{+0.36}_{-0.20}$	–
macs1115	13 (30)	2	0 (0)	0.15±0.10	–	$10.15^{+0.09}_{-0.10}$	–	$0.13^{+0.20}_{-0.20}$	–	$-10.01^{+0.29}_{-0.30}$	–
rxj1532	9 (25)	0	0 (0)	–	–	–	–	–	–	–	–
macs1720	19 (49)	10	4 (4)	0.53±0.11	0.21±0.09	$10.44^{+0.31}_{-0.16}$	$10.36^{+0.17}_{-0.08}$	$0.70^{+0.63}_{-0.59}$	$1.31^{+0.16}_{-0.18}$	$-9.72^{+0.63}_{-0.75}$	$-9.10^{+0.13}_{-0.14}$
macs0416	9 (25)	3	0 (0)	0.33±0.16	–	$10.11^{+0.16}_{-0.02}$	–	$0.55^{+0.19}_{-0.19}$	–	$-9.80^{+0.35}_{-0.01}$	–
macs0429	12 (51)	6	0 (1)	0.50±0.14	–	$10.23^{+0.30}_{-0.12}$	–	$0.24^{+0.73}_{-0.43}$	–	$-9.85^{+0.28}_{-0.59}$	–
macs1206	17 (35)	4	0 (1)	0.24±0.10	–	$10.53^{+0.27}_{-0.32}$	–	$0.62^{+0.33}_{-0.27}$	–	$-9.86^{+0.06}_{-0.06}$	–
macs0329	27 (85)	6	0 (0)	0.22±0.08	–	$10.49^{+0.11}_{-0.38}$	–	$0.34^{+0.39}_{-0.11}$	–	$-9.81^{+0.13}_{-0.50}$	–
rxj1347	12 (29)	4	0 (0)	0.33±0.14	–	$10.29^{+0.39}_{-0.23}$	–	$0.37^{+0.30}_{-0.22}$	–	$-9.98^{+0.10}_{-0.05}$	–
macs1311	9 (27)	3	0 (0)	0.33±0.16	–	$10.40^{+0.48}_{-0.15}$	–	$0.59^{+0.14}_{-0.14}$	–	$-9.81^{+0.01}_{-0.35}$	–
macs1149	15 (48)	7	1 (1)	0.47±0.13	0.07±0.06	$10.39^{+0.39}_{-0.30}$	10.39^{--}_{--}	$0.51^{+0.43}_{-0.20}$	1.41^{--}_{--}	$-9.80^{+0.52}_{-0.50}$	-8.98^{--}_{--}
macs0717	13 (17)	0	0 (0)	–	–	–	–	–	–	–	–
macs1423	7 (12)	2	1 (1)	0.29±0.17	0.14±0.13	$10.34^{+0.14}_{-0.14}$	10.54^{--}_{--}	$1.23^{+0.31}_{-0.31}$	1.69^{--}_{--}	$-9.11^{+0.17}_{-0.17}$	-8.86^{--}_{--}
macs2129	17 (22)	3	0 (0)	0.18±0.09	–	$10.37^{+0.25}_{-0.22}$	–	$0.78^{+0.21}_{-0.48}$	–	$-9.95^{+0.45}_{-0.02}$	–
macs0647	12 (36)	5	0 (0)	0.42±0.14	–	$10.27^{+0.06}_{-0.23}$	–	$0.78^{+0.10}_{-0.22}$	–	$-9.31^{+0.10}_{-0.36}$	–
macs0744	32 (57)	17	2 (2)	0.53±0.09	0.06±0.04	$10.43^{+0.25}_{-0.20}$	$10.37^{+0.04}_{-0.05}$	$0.61^{+0.97}_{-0.29}$	$1.92^{+0.16}_{-0.17}$	$-9.79^{+0.63}_{-0.40}$	$-8.45^{+0.12}_{-0.12}$
clj1226	39 (62)	15	5 (5)	0.38±0.08	0.13±0.05	$10.60^{+0.38}_{-0.48}$	$10.98^{+0.05}_{-0.31}$	$1.24^{+0.84}_{-0.43}$	$2.09^{+0.14}_{-0.09}$	$-8.95^{+0.21}_{-0.76}$	$-8.84^{+0.30}_{-0.07}$
Total	306 (702)	97	13 (17)								
Median		$0.6<z<0.9$	$0.2<\mathcal{R}/R_{200}<0.3$	$0.46^{+0.05}_{-0.05}$	$0.09^{+0.02}_{-0.02}$	$10.51^{+0.08}_{-0.09}$	$10.67^{+0.3}_{-0.3}$	$0.93^{+0.31}_{-0.31}$	$2.00^{+0.09}_{-0.09}$	$-9.37^{+0.42}_{-0.42}$	$-8.64^{-0.19}_{-0.19}$

Table 8. As in Table 5, for the field samples.

Field ID (1)	Galaxies (2)	UVJ-SF (3)	M-FIR (4)	$\mathcal{F}_{UVJ-\mathrm{SF}}$ (5)	$\mathcal{F}_{\mathrm{M-FIR}}$ (6)	$\mathcal{M}_{*,\,UVJ-\mathrm{SF}}$ (7)	$\mathcal{M}_{*,\,\mathrm{M-FIR}}$ (8)	$\mathcal{SFR}_{\mathrm{TOT},UVJ-\mathrm{SF}}$ (9)	$\mathcal{SFR}_{\mathrm{TOT,M-FIR}}$ (10)	$s\mathcal{SFR}_{\mathrm{TOT},UVJ-\mathrm{SF}}$ (11)	$s\mathcal{SFR}_{\mathrm{TOT,M-FIR}}$ (12)
A0383	97 (528)	67	16 (43)	0.69±0.05	0.16±0.04	$10.47^{+0.44}_{-0.39}$	$10.60^{+0.28}_{-0.34}$	$0.79^{+0.47}_{-0.61}$	$1.37^{+0.36}_{-0.28}$	$-9.74^{+0.53}_{-0.59}$	$-9.34^{+0.71}_{-0.29}$
A0209	114 (648)	84	18 (57)	0.74±0.04	0.16±0.03	$10.47^{+0.49}_{-0.37}$	$10.60^{+0.31}_{-0.41}$	$0.76^{+0.42}_{-0.56}$	$1.24^{+0.57}_{-0.14}$	$-9.78^{+0.49}_{-0.59}$	$-9.37^{+0.70}_{-0.27}$
A2261	124 (635)	83	18 (52)	0.67±0.04	0.15±0.03	$10.47^{+0.42}_{-0.32}$	$10.52^{+0.39}_{-0.33}$	$0.75^{+0.43}_{-0.53}$	$1.24^{+0.57}_{-0.14}$	$-9.75^{+0.44}_{-0.53}$	$-9.31^{+0.64}_{-0.33}$
RBS1748	137 (657)	95	25 (65)	0.69±0.04	0.18±0.03	$10.47^{+0.43}_{-0.30}$	$10.49^{+0.42}_{-0.30}$	$0.80^{+0.44}_{-0.56}$	$1.26^{+0.55}_{-0.15}$	$-9.72^{+0.47}_{-0.56}$	$-9.28^{+0.59}_{-0.34}$
A0611	109 (598)	71	15 (43)	0.65±0.05	0.14±0.03	$10.40^{+0.46}_{-0.24}$	$10.47^{+0.15}_{-0.28}$	$0.81^{+0.52}_{-0.50}$	$1.35^{+0.30}_{-0.16}$	$-9.60^{+0.38}_{-0.62}$	$-9.09^{+0.31}_{-0.24}$
MS2137	139 (792)	74	15 (40)	0.53±0.04	0.11±0.03	$10.41^{+0.49}_{-0.25}$	$10.48^{+0.39}_{-0.24}$	$0.79^{+0.56}_{-0.46}$	$1.36^{+0.11}_{-0.19}$	$-9.71^{+0.47}_{-0.47}$	$-9.23^{+0.32}_{-0.13}$
AS1063	160 (789)	78	16 (43)	0.49±0.04	0.10±0.02	$10.38^{+0.44}_{-0.28}$	$10.50^{+0.33}_{-0.25}$	$0.85^{+0.36}_{-0.49}$	$1.33^{+0.14}_{-0.18}$	$-9.58^{+0.35}_{-0.58}$	$-9.15^{+0.16}_{-0.34}$
MACS1931	160 (462)	78	16 (46)	0.49±0.04	0.10±0.02	$10.38^{+0.44}_{-0.28}$	$10.50^{+0.33}_{-0.25}$	$0.85^{+0.36}_{-0.49}$	$1.33^{+0.14}_{-0.18}$	$-9.57^{+0.33}_{-0.59}$	$-9.15^{+0.16}_{-0.34}$
MACS1115	151 (674)	72	16 (38)	0.48±0.04	0.11±0.03	$10.38^{+0.44}_{-0.28}$	$10.50^{+0.33}_{-0.25}$	$0.85^{+0.36}_{-0.53}$	$1.33^{+0.14}_{-0.18}$	$-9.61^{+0.40}_{-0.57}$	$-9.15^{+0.16}_{-0.34}$
RXJ1532	181 (699)	95	22 (64)	0.52±0.04	0.12±0.02	$10.38^{+0.46}_{-0.27}$	$10.50^{+0.33}_{-0.23}$	$0.85^{+0.32}_{-0.41}$	$1.30^{+0.17}_{-0.17}$	$-9.54^{+0.30}_{-0.59}$	$-9.21^{+0.23}_{-0.21}$
MACS1720	224 (919)	107	31 (59)	0.48±0.03	0.14±0.02	$10.37^{+0.44}_{-0.27}$	$10.51^{+0.31}_{-0.35}$	$0.95^{+0.34}_{-0.54}$	$1.29^{+0.19}_{-0.19}$	$-9.49^{+0.38}_{-0.65}$	$-9.28^{+0.39}_{-0.28}$
MACS0416	220 (851)	106	31 (58)	0.48±0.03	0.14±0.02	$10.36^{+0.40}_{-0.26}$	$10.49^{+0.28}_{-0.33}$	$0.95^{+0.36}_{-0.55}$	$1.31^{+0.17}_{-0.21}$	$-9.45^{+0.35}_{-0.68}$	$-9.22^{+0.33}_{-0.20}$
MACS0429	220 (795)	106	31 (60)	0.48±0.03	0.14±0.02	$10.36^{+0.40}_{-0.26}$	$10.49^{+0.28}_{-0.33}$	$0.95^{+0.36}_{-0.52}$	$1.31^{+0.17}_{-0.21}$	$-9.42^{+0.32}_{-0.71}$	$-9.22^{+0.33}_{-0.20}$
MACS1206	250 (936)	155	36 (55)	0.62±0.03	0.14±0.02	$10.38^{+0.44}_{-0.26}$	$10.54^{+0.33}_{-0.31}$	$0.89^{+0.38}_{-0.46}$	$1.31^{+0.31}_{-0.18}$	$-9.46^{+0.29}_{-0.69}$	$-9.18^{+0.25}_{-0.24}$
MACS0329	270 (972)	173	43 (68)	0.64±0.03	0.16±0.02	$10.36^{+0.45}_{-0.25}$	$10.51^{+0.34}_{-0.29}$	$0.91^{+0.35}_{-0.48}$	$1.31^{+0.20}_{-0.20}$	$-9.44^{+0.29}_{-0.65}$	$-9.19^{+0.25}_{-0.23}$
RXJ1347	270 (1066)	176	47 (84)	0.65±0.03	0.17±0.02	$10.36^{+0.46}_{-0.25}$	$10.56^{+0.31}_{-0.33}$	$0.90^{+0.37}_{-0.46}$	$1.31^{+0.25}_{-0.18}$	$-9.44^{+0.27}_{-0.67}$	$-9.22^{+0.26}_{-0.20}$
MACS1311	408 (1218)	256	67 (83)	0.63±0.02	0.16±0.02	$10.39^{+0.50}_{-0.27}$	$10.53^{+0.41}_{-0.29}$	$0.95^{+0.36}_{-0.50}$	$1.30^{+0.18}_{-0.21}$	$-9.45^{+0.32}_{-0.63}$	$-9.21^{+0.22}_{-0.36}$
MACS1149	470 (1414)	296	72 (72)	0.63±0.02	0.15±0.02	$10.48^{+0.48}_{-0.35}$	$10.56^{+0.39}_{-0.30}$	$1.00^{+0.38}_{-0.55}$	$1.34^{+0.16}_{-0.13}$	$-9.60^{+0.51}_{-0.56}$	$-9.21^{+0.27}_{-0.48}$
MACS0717	469 (970)	297	80 (80)	0.63±0.02	0.17±0.02	$10.49^{+0.50}_{-0.35}$	$10.60^{+0.48}_{-0.38}$	$1.02^{+0.36}_{-0.52}$	$1.35^{+0.19}_{-0.13}$	$-9.52^{+0.44}_{-0.63}$	$-9.22^{+0.29}_{-0.47}$
MACS1423	470 (1036)	297	69 (69)	0.63±0.02	0.15±0.02	$10.48^{+0.48}_{-0.35}$	$10.61^{+0.41}_{-0.34}$	$1.00^{+0.38}_{-0.55}$	$1.35^{+0.16}_{-0.12}$	$-9.59^{+0.50}_{-0.57}$	$-9.21^{+0.27}_{-0.48}$
MACS2129	539 (1462)	333	41 (41)	0.62±0.02	0.08±0.01	$10.48^{+0.48}_{-0.33}$	$10.66^{+0.40}_{-0.27}$	$1.02^{+0.38}_{-0.57}$	$1.49^{+0.23}_{-0.07}$	$-9.55^{+0.49}_{-0.64}$	$-9.06^{+0.17}_{-0.46}$
MACS0647	484 (1218)	311	54 (54)	0.64±0.02	0.11±0.01	$10.48^{+0.48}_{-0.33}$	$10.55^{+0.38}_{-0.26}$	$1.04^{+0.38}_{-0.60}$	$1.45^{+0.26}_{-0.09}$	$-9.55^{+0.56}_{-0.64}$	$-9.03^{+0.20}_{-0.29}$
MACS0744	860 (1706)	533	113 (113)	0.62±0.02	0.13±0.01	$10.43^{+0.40}_{-0.30}$	$10.71^{+0.31}_{-0.31}$	$1.14^{+0.43}_{-0.52}$	$1.61^{+0.27}_{-0.13}$	$-9.29^{+0.37}_{-0.66}$	$-9.03^{+0.29}_{-0.32}$
CLJ1226	940 (1576)	706	82 (82)	0.75±0.01	0.09±0.01	$10.51^{+0.46}_{-0.38}$	$10.77^{+0.44}_{-0.37}$	$1.32^{+0.42}_{-0.60}$	$1.94^{+0.14}_{-0.10}$	$-9.20^{+0.42}_{-0.67}$	$-8.86^{+0.43}_{-0.32}$
Total	7466 (22621)	4649	974 (1469)								
			$0.2<z<0.4$	$0.53^{+0.16}_{-0.04}$	$0.14^{+0.02}_{-0.03}$	$10.40^{+0.07}_{-0.02}$	$10.50^{+0.00}_{-0.00}$	$0.81^{+0.04}_{-0.01}$	$1.33^{+0.00}_{-0.03}$	$-9.62^{+0.05}_{-0.10}$	$-9.23^{+0.07}_{-0.05}$
		Median	$0.4<z<0.6$	$0.63^{+0.01}_{-0.06}$	$0.15^{+0.02}_{-0.02}$	$10.38^{+0.09}_{-0.02}$	$10.53^{10.54}_{10.50}$	$0.95^{+0.00}_{-0.05}$	$1.31^{+0.00}_{-0.00}$	$-9.46^{+0.01}_{-0.08}$	$-9.21^{+0.00}_{-0.01}$
			$0.6<z<0.9$	$0.69^{+0.04}_{-0.04}$	$0.11^{+0.02}_{-0.02}$	$10.47^{+0.04}_{-0.04}$	$10.73^{+0.03}_{-0.03}$	$1.23^{+0.09}_{-0.09}$	$1.77^{+0.16}_{-0.16}$	$-9.24^{+0.05}_{-0.05}$	$-9.07^{+0.02}_{-0.02}$

8 STELLAR MASS DISTRIBUTIONS

As a step prior to the evaluation of the SF within cluster cores and how it compares to the SF in the field, we explore the stellar mass function (SMF) of the samples presented in the previous section. The SMF is a fundamental observable for the study of the evolution of galaxy populations. Furthermore, overlooking hypothetical differences in the SMF of field and cluster samples can lead to a misinterpretation of the physics behind the level of SF quantified in the following sections.

In the top panels of Figure 8, we display the SMF for clusters and field galaxies ($\log_{10}\mathcal{M}_*/M_\odot > 10$) divided into bins of redshift. We include only galaxies at $\mathcal{R} < 0.1R_{200}$, i.e., the $\mathcal{R}$ range homogeneously covered along the whole redshift range. We exclude the BCGs in our analysis. We correct for different cluster richnesses by randomly re-sampling the galaxy population of each cluster using the average sample size of each redshift bin. Then, to render the field and cluster samples statistically comparable, we re-sample each field drawing randomly the number of galaxies in the corresponding cluster sample. The uncertainties are estimated from the combination of 500 bootstraps. Then, we model the data by fitting a Schechter function (Schechter 1976) to the SMF. The form of the function is

$$\Phi(\mathcal{M}_*)\, d\mathcal{M}_* = \Phi^* \left(\frac{\mathcal{M}_*}{\mathcal{M}^*}\right)^\alpha e^{-\frac{\mathcal{M}_*}{\mathcal{M}^*}} \frac{d\mathcal{M}_*}{\mathcal{M}^*}, \qquad (10)$$

with $\mathcal{M}^*$ being the characteristic mass, α the low-mass slope, and Φ^* the normalization. The normalization is evaluated by requiring that the integral of the Schechter function over the stellar mass range considered equals the fraction of galaxies in the sample fitted with respect the total sample. In Table 9 we report the best-fit parameters. The function provides overall reasonable fits, although we report a quite large scatter of the data points for some of the samples. This is probably due to the limited number counts we work with. In the bottom panels of Figure 8, we display the fraction of UVJ-P and UVJ-SF galaxies in each stellar mass bin. The plots are not perfectly symmetric because we do not fix the median value of each mass bin. We do not represent the stellar mass distribution of the M-FIR sample because its size is not statistically significant for this analysis. The median value of stellar mass corresponding to each sample is marked in the upper panels of the same figure (see also Table 9).

We compare the best-fitting Schechter parameters with those published recently by van der Burg et al. (2018) for cluster and field galaxies at $0.5 < z < 0.7$. We focus our comparison on their inner $\mathcal{R}$ bin ($\mathcal{R}/R_{200} \lesssim 0.4$). Their $\log_{10}\mathcal{M}^*$ are $11.01^{+0.02}_{-0.02}$, $11.01^{+0.01}_{-0.02}$, and $10.70^{+0.04}_{-0.04}$ for the whole population, the quiescent, and the star-forming samples of the clusters, respectively, and $11.18^{+0.02}_{-0.02}$, $11.06^{+0.02}_{-0.02}$, and $10.89^{+0.05}_{-0.05}$ for the same subsamples in the field. We assume a 0.2 dex conversion from Chabrier (Chabrier 2003) to Salpeter IMF (Conroy et al. 2009). Our results for the clusters and field between $0.4 < z < 0.6$ are compatible with theirs except in the case of the cluster UVJ-P sample, for which we derive $\log_{10}\mathcal{M}^* = 11.22^{+0.06}_{-0.06}$, and the field UVJ-SF and UVJ-P populations, for which we derive larger values: $\log_{10}\mathcal{M}^* = 11.30^{+0.09}_{-0.09}$, and $11.32^{+0.13}_{-0.13}$, respectively. Regarding α, they retrieve $-0.91^{+0.02}_{-0.02}$, $-0.83^{+0.03}_{-0.02}$, and $-1.02^{+0.06}_{-0.06}$ for the whole population, the quiescent, and the star-forming

samples of the clusters, and $-1.20^{+0.02}_{-0.02}$, $-0.55^{+0.03}_{-0.03}$, and $-1.33^{+0.03}_{-0.03}$ for the field. In this case, our results are compatible with theirs within the error bars.

In the first two redshift bins, there are no large differences between the SMF of the whole population of galaxies in the field and the clusters, with values of the slope and the knee of the Schechter function within the 1σ errors (see Table 9). This result has been found in previous works at intermediate and high redshift (e.g., Vulcani et al. 2012, Vulcani et al. 2013, van der Burg et al. 2013, Nantais et al. 2016). On the contrary, the highest redshift bin displays large differences between the cluster and the field best-fit Schechter functions. We claim these differences are mainly due to a poor sampling of the cluster SMF. In fact, data points in the stellar mass range including 80% of the stellar mass of both cluster and field samples are compatible within the error bars.

We report hints of a different behaviour of the SMFs of field and clusters and their evolution with z when we split the galaxy populations in UVJ-SF and UVJ-P. At the lowest redshift, the UVJ-P SMF appears to present a steeper α than the field, which is not obvious in the second redshift bin. This makes the UVJ-P SMF present a shape apparently more similar to the field UVJ-SF stellar mass distributions (excluding normalization differences). Balogh et al. (2001) also find that while in the field environment the SMF of SFGs has much steeper faint-end slope than that for passive galaxies, in the clusters, the passive galaxies have also a steep faint-end. Annunziatella et al. (2014) find that for the $z = 0.44$ (our second redshift bin) cluster MACS1206 (also included in our sample), the SMF of SFGs is significantly steeper than the SMF of passive galaxies at the faint end. This is in agreement with our best-fitting SMFs in the intermediate redshift bin. Furthermore, they find a smaller slopes SMF for passive cluster galaxies in the inner core of clusters ($\mathcal{R}/R_{200} \lesssim 0.25$), than in the outskirts.

However, these differences are not significant in most cases. The best-fitting values of α and $\log_{10}\mathcal{M}^*$ for the UVJ-SF and UVJ-P samples in the clusters and in the field are overall compatible within the error bars. The only significant difference appears in the value of the $\log_{10}\mathcal{M}^*$ for the UVJ-SF samples in the lowest redshift bin: $10.55^{+0.06}_{-0.06}$ and $11.11^{+0.05}_{-0.05}$ for the clusters and the field, respectively. Other works have also reported the lack of significant differences between the SMF of star-forming and passive galaxies in different environments (i.e., Vulcani et al. 2013). The UVJ-SF and UVJ-P SMF evolution with redshift is also mild in terms of the best-fitting Schechter parameters α and $\log_{10}\mathcal{M}^*$, and considering our resolution.

In the first two redshift bins, we find that the galaxy population in massive clusters is clearly dominated by quiescent galaxies all the way down to $\mathcal{M}_* = 10^{10}M_\odot$, which is in agreement with (e.g.) van der Burg et al. (2018). The largest mass bins are dominated by stochasticity given the small number of galaxies included. Peng et al. (2010) predicts that the SMFs of passive and SFGs should cross (crossing mass) at $\log_{10}\mathcal{M}_*/M_\odot \approx 10.4$ and 9.6 for central ("field") and satellites, respectively, at low redshift. In our work, the crossing mass for the cluster SMFs shows up at $\log_{10}\mathcal{M}_*/M_\odot \approx 10$ in the second redshift bin. In the third redshift bin, the contribution of UVJ-SF and UVJ-P samples to the whole population of clusters is $\approx 50\%$, with type

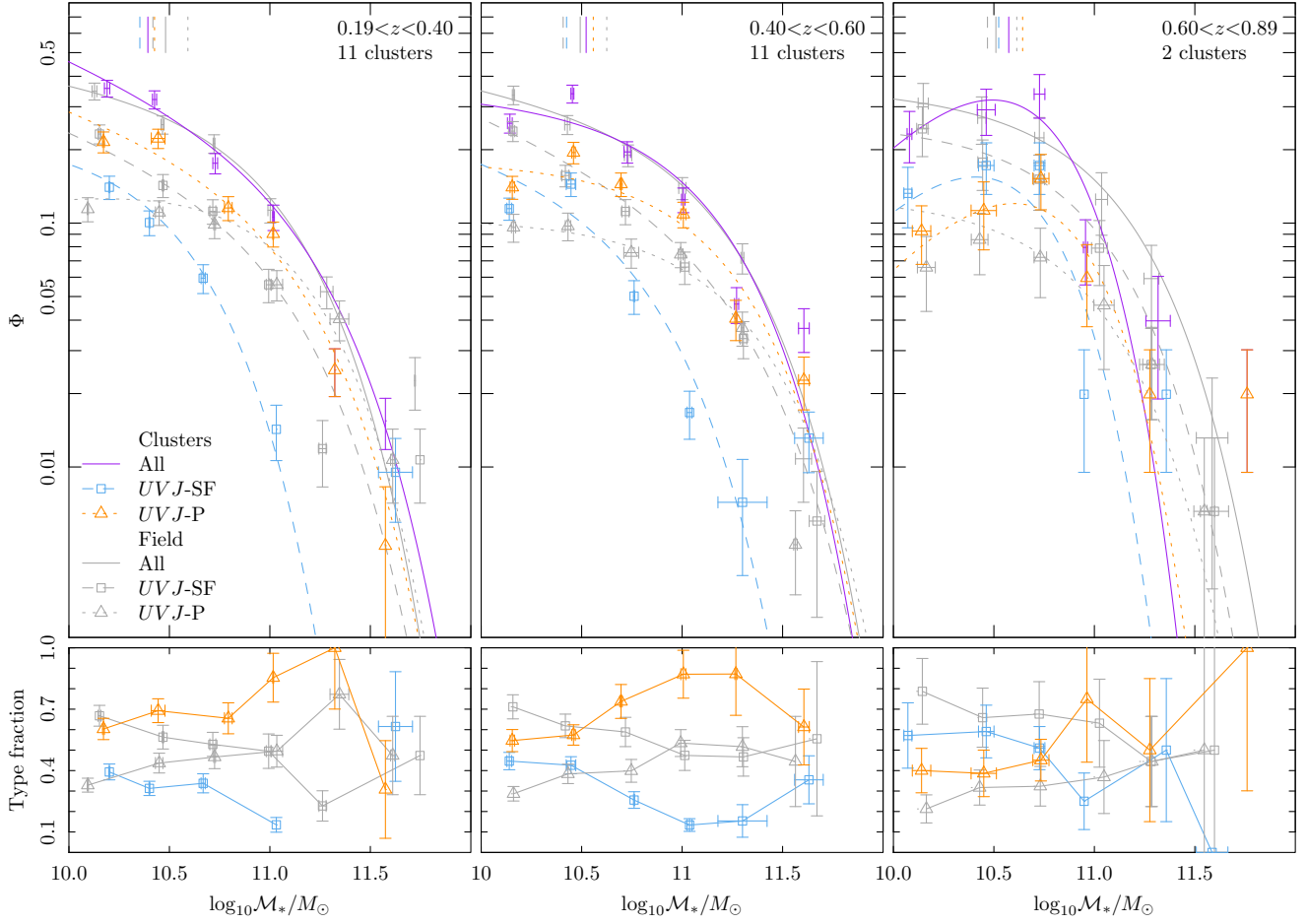**Figure 8.** *Top panels*: Stellar mass distribution within $\mathcal{R}/R_{200}<0.1$ for cluster and field galaxies ($\log_{10}\mathcal{M}_*/M_\odot>10$) divided in bins of redshift. On the upper part of each panel, we mark the median stellar mass of every sample. *Bottom panels*: Relative fraction of UVJ-P and UVJ-SF galaxies as a function of stellar mass.

Table 9. We report: Median $\log_{10}\mathcal{M}_*$ (and 1σ intervals), best-fitting Schechter parameters (and 1σ intervals) and reduced χ^2 for the different samples.

		Sample	$\langle\log_{10}\mathcal{M}_*/M_\odot\rangle$	$\log_{10}\mathcal{M}^*/M_\odot$	α	Φ^*	χ^2
$0.19<z<0.40$	Cluster	All galaxies	$10.39^{+0.48}_{-0.22}$	$11.22^{+0.56}_{-0.54}$	$-1.3^{+0.3}_{-0.3}$	$0.08^{+0.08}_{-0.08}$	1.81
		UVJ-SF	$10.35^{+0.30}_{-0.19}$	$10.55^{+0.06}_{-0.06}$	$-1.0^{+0.6}_{-0.2}$	$0.10^{+0.01}_{-0.01}$	5.52
		UVJ-P	$10.43^{+0.49}_{-0.25}$	$11.14^{+0.13}_{-0.13}$	$-1.3^{+0.1}_{-0.1}$	$0.06^{+0.03}_{-0.03}$	7.18
	Field	All galaxies	$10.48^{+0.48}_{-0.38}$	$11.05^{+0.12}_{-0.12}$	$-1.1^{+0.1}_{-0.1}$	$0.13^{+0.04}_{-0.04}$	5.69
		UVJ-SF	$10.42^{+0.47}_{-0.31}$	$11.11^{+0.05}_{-0.05}$	$-1.3^{+0.5}_{-0.5}$	$0.05^{+0.00}_{-0.00}$	5.61
		UVJ-P	$10.59^{+0.47}_{-0.49}$	$11.09^{+0.18}_{-0.18}$	$-0.9^{+0.2}_{-0.2}$	$0.07^{+0.02}_{-0.02}$	5.41
$0.40<z<0.60$	Cluster	All galaxies	$10.52^{+0.47}_{-0.33}$	$11.15^{+0.30}_{-0.30}$	$-1.0^{+0.3}_{-0.3}$	$0.13^{+0.09}_{-0.09}$	3.90
		UVJ-SF	$10.42^{+0.35}_{-0.28}$	$10.83^{+0.90}_{-0.90}$	$-1.2^{+0.4}_{-0.4}$	$0.06^{+0.05}_{-0.05}$	11.47
		UVJ-P	$10.56^{+0.47}_{-0.30}$	$11.22^{+0.06}_{-0.06}$	$-1.0^{+0.5}_{-0.5}$	$0.08^{+0.00}_{-0.00}$	6.23
	Field	All galaxies	$10.49^{+0.52}_{-0.35}$	$11.22^{+0.02}_{-0.02}$	$-1.2^{+0.1}_{-0.1}$	$0.11^{+0.01}_{-0.01}$	6.35
		UVJ-SF	$10.41^{+0.53}_{-0.28}$	$11.30^{+0.09}_{-0.09}$	$-1.4^{+0.1}_{-0.1}$	$0.04^{+0.01}_{-0.01}$	1.49
		UVJ-P	$10.63^{+0.49}_{-0.41}$	$11.32^{+0.13}_{-0.13}$	$-1.0^{+0.5}_{-0.5}$	$0.05^{+0.01}_{-0.01}$	6.07
$0.60<z<0.89$	Cluster	All galaxies	$10.57^{+0.31}_{-0.38}$	$10.49^{+0.26}_{-0.26}$	$0.0^{+0.2}_{-0.2}$	$0.39^{+0.07}_{-0.07}$	1.71
		UVJ-SF	$10.52^{+0.27}_{-0.42}$	$10.41^{+2.60}_{-2.60}$	$0.0^{+0.8}_{-0.8}$	$0.18^{+0.46}_{-0.46}$	12.29
		UVJ-P	$10.64^{+0.32}_{-0.39}$	$10.60^{+0.07}_{-0.07}$	$0.0^{+0.5}_{-0.5}$	$0.14^{+0.02}_{-0.02}$	9.60
	Field	All galaxies	$10.51^{+0.46}_{-0.35}$	$11.11^{+0.05}_{-0.05}$	$-1.0^{+0.1}_{-0.1}$	$0.14^{+0.02}_{-0.02}$	1.22
		UVJ-SF	$10.47^{+0.44}_{-0.34}$	$11.00^{+0.50}_{-0.50}$	$-1.0^{+0.5}_{-0.5}$	$0.10^{+0.01}_{-0.01}$	7.86
		UVJ-P	$10.64^{+0.50}_{-0.37}$	$11.00^{+0.29}_{-0.29}$	$-1.0^{+0.2}_{-0.2}$	$0.05^{+0.03}_{-0.03}$	0.58

fractions comparable within the error bars. This is comparable with the UVJ-P and UVJ-SF type fractions derived by Nantais et al. (2016) for $z\sim1.5$. Regarding the field, lower mass bins ($\log_{10}\mathcal{M}_*/M_\odot$<10.6, 10.9, and 10.9 for the first, second, and third redshift bins, respectively) are dominated by star-forming galaxies, whereas the contribution of UVJ-P and UVJ-SF galaxies tend to converge and even to be inverse towards higher mass bins. Other previous studies (e.g., Quadri et al. 2012, Nantais et al. 2016, Papovich et al. 2018) have claimed a rapid increase in the number density of low- and intermediate-mass ($\log\mathcal{M}_*/M_\odot$<10–10.6) quiescent galaxies in denser environments since $z\approx1.5$. Moutard et al. (2018) and Mortlock et al. (2015) also find evidence for a higher number density of quiescent low-mass galaxies in denser environments in our same redshift range. However, our $\mathcal{M}_*$ completeness levels hampers the analysis of a possible evolution of the distribution of stellar mass at such low values.

It is worth noting that numerous works (e.g., Annunziatella et al. 2016) find that passive cluster galaxies are better fitted by a double Schechter function, revealing the existence of two sub-populations of red cluster members thought to have followed distinct evolutionary paths. On the one hand, a population of high mass galaxies thought to be quenched by processes scaling with stellar mass, and on the other hand, a population of low-mass galaxies quenched by environmental processes (Peng et al. 2010). These composite SMF of red passive galaxies have also been observed in the field in works such as, e.g., Drory et al. (2009) and Baldry et al. (2012). However, the evidence for these double Schechter functions (i.e., an upturn at low stellar masses) is only visible at $\log_{10}\mathcal{M}_*/M_\odot\lesssim10$ (Drory et al. 2009), below the mass limit of our work.

9   QUANTIFICATION OF STAR FORMATION PROCESSES WITHIN CLUSTER CORES

In this section, we present a quantification of the SF activity hosted by cluster members and field galaxies with $\log_{10}\mathcal{M}_*/M_\odot$>10, as traced by the UV and the M- and FIR.

9.1   Star-forming galaxy fraction

Figure 9 (left hand panel) shows the fraction ($\mathcal{F}$) of UVJ-SF and M-FIR galaxies ($\mathcal{F}_{UVJ-SF}$ and $\mathcal{F}_{M-FIR}$, respectively; Section 7.4) in the clusters ($\mathcal{R}/R_{200}$<0.1) and in the field. Error bars are obtained using the margin of error of a percentage[7] assuming a standard normal distribution. On the right panel, we show the median $\mathcal{F}$ and quantiles 16th and 84th (in the shape of error bars) in the same redshift bins of Figure 6. We also include with larger symbols the fractions obtained at $0.1<\mathcal{R}/R_{200}<0.2$ and $0.2<\mathcal{R}/R_{200}<0.3$, at the corresponding redshift bins. In all cases, the median and quantiles are obtained using the bootstrap methodology.

To quantify the trends of $\mathcal{F}$ with redshift, we fit to

the data points (fraction for each individual cluster within $\mathcal{R}/R_{200}$<0.1) a function with the shape $\alpha(1+z)^\beta$, where α corresponds to the value of $\mathcal{F}$ at z=0, and β describes its evolution with redshift (with larger values of β meaning a steeper trend). This methodology is also applied by (e.g.) Haines et al. (2013) and Alberts et al. (2014). The corresponding curves and 1σ confidence intervals (generated using Monte Carlo simulations) are over-plotted in Figure 9 with a coloured line and a shaded area around it, respectively. Table 10 shows the α and β values of the best-fit. In the case of the M-FIR samples, we fit only the clusters with a $\mathcal{SFR}_{TIR}$ limit below $10 M_\odot \text{yr}^{-1}$ (z<0.570) to derive the redshift trend.

The first information we can derive from Figure 9 is that, as expected, the $\mathcal{F}$ within clusters is much smaller than in the field for both UVJ-SF and M-FIR samples. On average, $\mathcal{F}_{UVJ-SF}$ in clusters seems to be approximately 1/2 the value in the field. The $\mathcal{F}_{M-FIR}$ in clusters drop down to values not significantly different to zero. Assuming the same fraction of M-FIR galaxies among the SFGs in clusters and field, the expected average $\mathcal{F}_{M-FIR}$ for the former would be $\sim$5%, which seems reasonably consistent with our results. Therefore, we cannot say there is a smaller fraction of highly star-forming galaxies ($\mathcal{SFR}_{TIR}$>$10 M_\odot \text{yr}^{-1}$) and/or dusty systems in the inner cores of clusters at intermediate redshifts.

Figure 9 also displays different evolutions of $\mathcal{F}$ for clusters and field with z. The latter displays mild increasing trends for $\mathcal{F}_{UVJ-SF}$ and $\mathcal{F}_{M-FIR}$, which vary with β=0.2±0.3 β=0.2±0.5, respectively. $\mathcal{F}$ remains $\sim$60% for the UVJ-SF samples between z=0.19-0.89. Flat/mild trends for the fraction of the star-forming population of galaxies in the field at intermediate redshifts (z<1) are also found by Brammer et al. 2011 and Darvish et al. 2017. In particular, the latter gives 70% of fraction of SFGs which is comparable with our results, although there is a larger offset between these numbers and the 40% given by the former. These differences are likely due to the sample selection criteria. The fraction of M-FIR galaxies remain also constant ($\sim$0.15) in the same redshift range. The decreasing trend of the data points at z>0.570 (not fitted) is due to the fact that the minimum $\mathcal{SFR}_{TIR}$ detectable for this clusters is larger than the value used to select M-FIR galaxies.

If we now focus on the clusters, we can see that, despite the cluster-to-cluster variations (which reach $\sim$0.3), we identify for both UVJ-SF and M-FIR samples a trend resembling the Butcher & Oemler (1984) effect, in which the fraction of SFGs in clusters is observed to increase with redshift. In this case, the trends are fitted with β=1.1 ± 0.6 and β=7.3 ± 5.8 for the UVJ-SF and M-FIR samples, respectively. The fraction of UVJ-SF galaxies within clusters increases from 28% at $z\sim0.2$ to 47% at $z\sim0.9$, while the fraction of M-FIR galaxies grows from 0% to 9% in the same period. These values are in agreement with previous studies. For instance, Haines et al. (2009) find that the fraction of massive galaxies with $\mathcal{L}_{TIR}$>$5\times10^{10}\mathcal{L}_\odot$ and $\mathcal{R}$<R_{200} varies from $\sim$3% at z=0.02 to $\sim$10% at z=0.3 with β=$5.7^{+2.1}_{-1.8}$. The fraction varies between $\sim$1% at z=0.15 and $\sim$4% at z=0.3 considering only $\mathcal{R}\lesssim0.3R_{200}$. Finally, the contribution of M-FIR galaxies to the whole SFGs population (UVJ-SF sample) remains $\sim$23% in the field, and varies from 0% to 19% in the clusters between $z\sim0.2$ and $z\sim0.9$. Martis et al.

---

[7] The confidence interval of a point sample estimate of the population proportion at 1σ can be derived considering a standard normal distribution with the expression $\sqrt{p(1-p)/n}$, where n is the size of the sample and p is the proportion. Both of them must satisfy the condition that $np \geq 5$ and $n(1-p) \geq 5$.
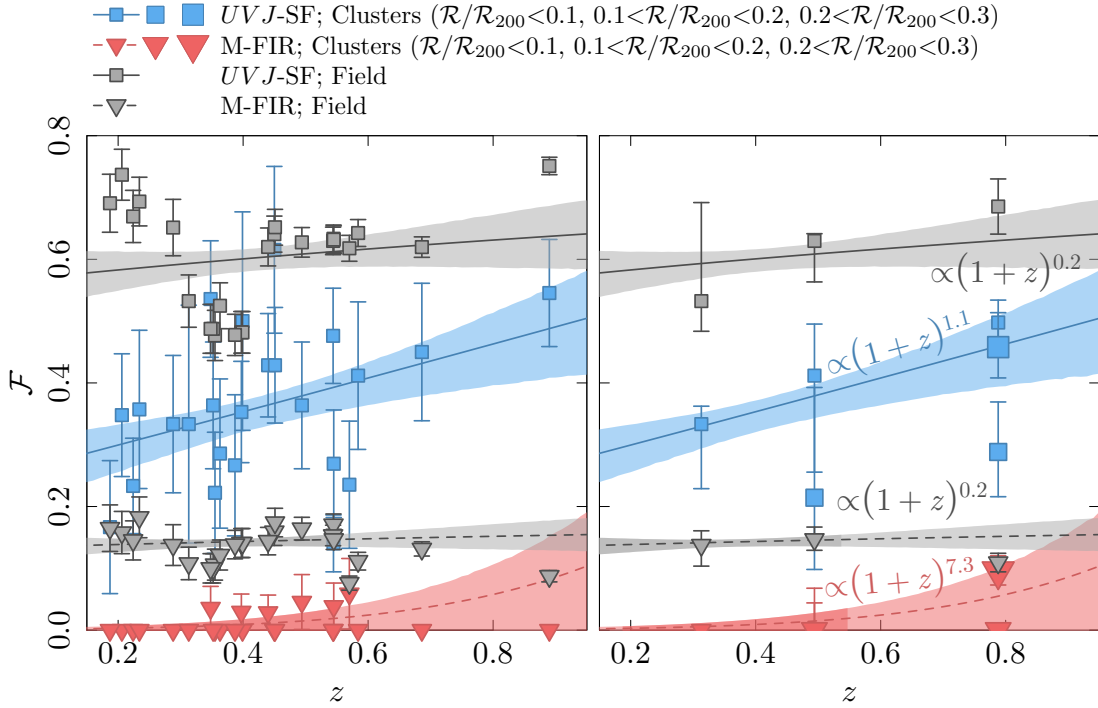
Figure 9. UVJ-SF and M-FIR fractions. In the left panel we consider only cluster members at $\mathcal{R}/R_{200}<0.1$. In the right-hand panels we show the average of the individual values at $\mathcal{R}/R_{200}<0.1$, $0.1<\mathcal{R}/R_{200}<0.2$, and $0.2<\mathcal{R}/R_{200}<0.3$, in three redshift bins ($0.2<z<0.4$, $0.4<z<0.6$, $0.6<z<0.9$). In both panels, we show the best fit of a trend with redshift of the shape $\alpha(1+z)^\beta$ and corresponding 1σ confidence intervals (continuous and dashed lines, and corresponding shaded areas, respectively). Darker red shaded areas represent the redshift range used for the fit of the M-FIR samples of clusters and field. For each cluster for which the M-FIR sample is empty, we represent the corresponding data point on the bottom-horizontal axis.

Table 10. Best-fitting parameters derived from the fit of the evolution with redshift of the $\mathcal{F}$, and median $\mathcal{SFR}_{\rm TOT}$ and $s\mathcal{SFR}_{\rm TOT}$ for all the UVJ-SF and M-FIR samples in the clusters and in the field. For the clusters we include the results only for $\mathcal{R}/R_{200}<0.1$. The function fitted is a power-law of the shape $\alpha(1+z)^\beta$. The units of β are $M_\odot{\rm yr}^{-1}$ and ${\rm yr}^{-1}$ in the case of the fit of $\mathcal{SFR}$ and $s\mathcal{SFR}$, respectively. The reduced χ^2 for each case are shown in the last column. The fits of the UVJ-SF samples are performed using the data points spread out the whole redshift range. In the case of the M-FIR we fit only reported redshift ranges.

Quantity	Environment	Subsample	z-range	α	β	χ^2
$\mathcal{F}$	Cluster ($\mathcal{R}/R_{200}<0.1$)	UVJ-SF	0.19-0.89	0.25±0.05	1.1±0.6	2.11
		M-FIR	0.19-0.57	0.00±0.00	7.3±5.8	0.19
	Field	UVJ-SF	0.19-0.89	0.56±0.06	0.2±0.3	7.27
		M-FIR	0.19-0.57	0.13±0.02	0.2±0.5	0.93
$\mathcal{SFR}_{\rm TOT}$	Cluster ($\mathcal{R}/R_{200}<0.1$)	UVJ-SF	0.19-0.89	1.82±0.71	1.3±1.0	21.75
		M-FIR	0.34-0.57	2.67±3.24	5.9±2.8	0.11
	Field	UVJ-SF	0.19-0.57	3.36±0.20	2.6±0.2	1.53
		M-FIR	0.19-0.57	18.10±1.37	0.4±0.2	0.29
$s\mathcal{SFR}_{\rm TOT}$	Cluster ($\mathcal{R}/R_{200}<0.1$)	UVJ-SF	0.19-0.89	$(0.67\pm0.22)\times10^{-10}$	1.2±0.9	50.37
		M-FIR	0.34-0.57	$(0.51\pm8.70)\times10^{-9}$	0.0±9.5	1.31
	Field	UVJ-SF	0.19-0.89	$(1.24\pm0.17)\times10^{-10}$	2.4±0.4	2.69
		M-FIR	0.19-0.57	$(4.56\pm0.60)\times10^{-10}$	0.8±0.4	0.60

(2016) reports very little evolution of the ratio of dusty and non-dusty star-forming galaxies as a function of stellar mass throughout this same redshift range.

The average values of $\mathcal{F}_{UVJ-{\rm SF}}$ and $\mathcal{F}_{\rm M-FIR}$ do not present a clear trend with $\mathcal{R}$. In fact, all of them are compatible with the curve fitted to the fractions at $\mathcal{R}/R_{200}<0.1$. However, the distribution of SFGs in these high density environments has been observed to increase with the projected cluster-centric radius by (e.g.) Alberts et al. 2016,

and Haines et al. 2015. This could be the result of a combination of factors such as cluster to cluster variations and an intrinsic negligible trend with redshift at $\mathcal{R}/R_{200}<0.3$.

9.2 Environmental quenching efficiency

The environmental quenching efficiency ($\mathcal{QE}_{\rm env}$; van den Bosch et al. 2008, Peng et al. 2010, Balogh et al. 2016) is

defined as

$$\mathcal{QE}_{\mathrm{env}} = (\mathcal{F}_{\mathrm{P,cluster}} - \mathcal{F}_{\mathrm{P,field}})/\mathcal{F}_{\mathrm{SF,field}}, \qquad (11)$$

where $\mathcal{F}_{\mathrm{P,cluster}}$ and $\mathcal{F}_{\mathrm{P,field}}$ are the fraction of passive galaxies in the cluster and field, respectively, and $\mathcal{F}_{\mathrm{SF,field}}$ is the fraction of SFGs in the field.

In Figure 10, we show the $\mathcal{QE}_{\mathrm{env}}$ in the cluster cores ($\mathcal{R}/R_{200}<0.1$) grouped in three redshift bins ($0.2<z<0.4$, $0.4<z<0.6$, $0.6<z<0.9$). We derive $\mathcal{QE}_{\mathrm{env}}$ values of $0.49^{+0.09}_{-0.08}$, $0.38^{+0.08}_{-0.07}$, and $0.30^{+0.07}_{-0.08}$ at $z\sim0.31$, 0.49, and 0.79, respectively. These values are smaller than those presented by Nantais et al. (2017) at $0.87<z<1.63$ for galaxies with $\log\mathcal{M}_*/\mathrm{M}_\odot \geq 10.3$. Our value of $\mathcal{F}_{UVJ-\mathrm{SF}}$ for clusters (field) in the highest redshift bin is $0.50^{+0.03}_{-0.03}$ ($0.69^{+0.04}_{-0.04}$) which leads to smaller values of the passive fraction than their $0.88^{+0.04}_{-0.03}$. Our results at $z\sim0.8$ are also smaller than other works such as Balogh et al. (2016) at redshift $z\sim1$ for the same values of stellar mass. It is worth noting that these works calculate the $\mathcal{QE}_{\mathrm{env}}$ within cluster-centric distances of $1\,\mathrm{Mpc}$ or R_{200}, while we focus on the inner cluster core, where the fraction of passive galaxies is expected to be larger.

The dependence of the $\mathcal{QE}_{\mathrm{env}}$ with stellar mass is under debate. While some works (e.g., Peng et al. 2010, van der Burg et al. 2018) claim environmental quenching to be independent of mass quenching, others (e.g., Lin et al. 2014, Kawinwanichakij et al. 2017) have detected an increasing trend of the $\mathcal{QE}_{\mathrm{env}}$ with stellar mass. The bottom panel of Figure 10 shows the values of $\mathcal{QE}_{\mathrm{env}}$ obtained for galaxies at $\mathcal{R}<0.1R_{200}$ in two stellar mass bins ($10.0<\log\mathcal{M}_*/\mathrm{M}_\odot<10.7$ and $10.7<\log\mathcal{M}_*/\mathrm{M}_\odot$). As we can see, only in the first redshift bin the $\mathcal{QE}_{\mathrm{env}}$ appears significantly larger for the more massive galaxies. This $\mathcal{QE}_{\mathrm{env}}$ appears larger also if we split the sample at lower masses, but the significance of the result decreases. Darvish et al. (2016) claims that environmental quenching efficiency is almost independent of stellar mass at $z<1$, except for galaxies with $\log\mathcal{M}_*/\mathrm{M}_\odot>10.9$, that high density environments could quench more efficiently.

9.3 Average $\mathcal{SFR}$ and $s\mathcal{SFR}$

A complementary quantification of the SF activity in clusters tackles the question whether beyond the decrease in $\mathcal{F}$ shown in Figure 9, the impact of the cluster environment modifies the distribution of the rates at which the remaining SFGs form stars. In Figure 11 (top and bottom left-hand panels), we display, as a function of redshift, the median $\mathcal{SFR}$ and $s\mathcal{SFR}$ of each cluster ($\mathcal{R}/R_{200}<0.1$) and field sample of UVJ-SF and M-FIR galaxies. The error bars are determined using the bootstrap technique to derive the 1σ confidence intervals, and thus, they represent the spread in the $\mathcal{SFR}$ and $s\mathcal{SFR}$ of each subsample, not the intrinsic error of the estimation of these parameters ($\sim0.3\,\mathrm{dex}$). In the corresponding right-hand panels we display the median values and confidence intervals in three redshift bins. We also include the median values obtained at $0.1<\mathcal{R}/R_{200}<0.2$ and $0.2<\mathcal{R}/R_{200}<0.3$, when possible.

To quantify the trends of the average $\mathcal{SFR}$ and $s\mathcal{SFR}$ with redshift, we again fit the median values (of the individual clusters) using a function of the shape $\alpha(1+z)^\beta$. Regarding the M-FIR samples, we only fit those data points corresponding to clusters at $z<0.57$ where at least a galaxy is de-
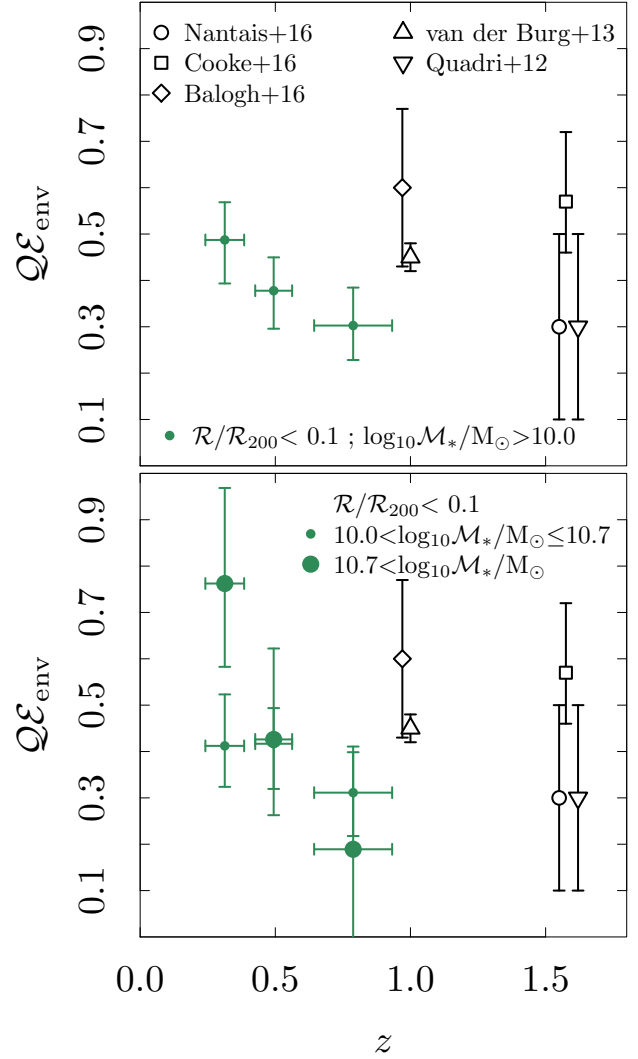

Figure 10. *Top panel*: Environmental quenching efficiency for galaxies with $\log\mathcal{M}_*/\mathrm{M}_\odot>10$ in three z bins. *Bottom panel*: Environmental quenching efficiency calculated for two mass bins ($10.0<\log\mathcal{M}_*/\mathrm{M}_\odot\leq10.7$ and $\log\mathcal{M}_*/\mathrm{M}_\odot>10.7$). In all cases, error bars are calculated propagating the errors of the fractions, which were obtained through bootstrap (500 realizations) in the initial cluster members and field galaxies samples. For comparison purposes, we include the $\mathcal{QE}_{\mathrm{env}}$ values given by Quadri et al. (2012), van der Burg et al. (2013), Balogh et al. (2016), Cooke et al. (2016), Nantais et al. (2016).

tected in the M- or FIR. Effectively, the fit is performed only between $0.34<z<0.57$ (darker shaded area in Figure 12). The best-fit parameters are shown in Table 10. We also include a corresponding 1σ confidence intervals of the fit (generated using Monte Carlo simulations) as a shaded area around each best-fit curve. The confidence intervals are not representative of the dispersion of the $\mathcal{SFR}$ and $s\mathcal{SFR}$ distributions, typically $\sim0.3\,\mathrm{dex}$.

Regarding the UVJ-SF samples, Figure 11 clearly shows an offset between the field and the clusters, with the latter displaying $\mathcal{SFR}$ and $s\mathcal{SFR}$ on average ~0.3 dex lower. This offset cannot be explained by the differences be-
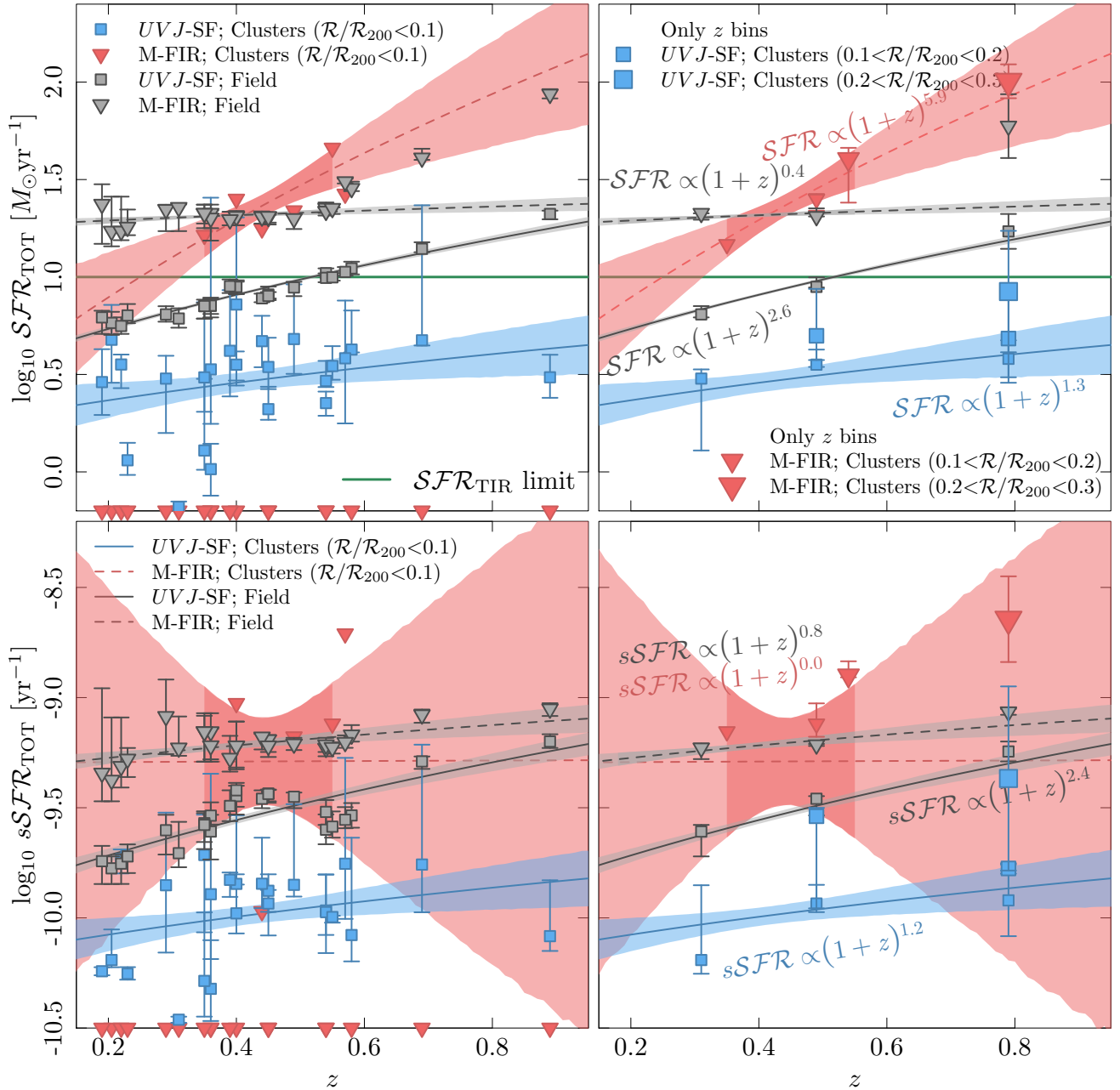
Figure 11. *Top panel*: median $\mathcal{SFR}$ for the UVJ-SF and M-FIR samples. *Bottom panel*: median $s\mathcal{SFR}_{\mathrm{TOT}}$ for the UVJ-SF and M-FIR samples. Representation as in Figure 9.

tween the mass distribution of field and clusters samples (see Section 8). This can be seen in Figure 5 and Figure 6, where the offsets in $\mathcal{SFR}$ and $s\mathcal{SFR}$ are visible at fixed $\mathcal{M}_*$.

Figure 11 also displays a clear increasing trend with z of the $\mathcal{SFR}$ for both field and cluster UVJ-SF samples (β=2.6±0.2 and β=1.3±1.0, respectively). The average $\mathcal{SFR}$ and $s\mathcal{SFR}$ do not show a strong differential evolution relative to the field but a systematic offset. Analogous trends are found for the $s\mathcal{SFR}$, with β=2.4±0.4 and β=1.2±0.9 for the field and the clusters, respectively. This also suggests that there is not a significant evolution of the

$\mathcal{M}_*$ distributions driving the variation in $s\mathcal{SFR}$, at least at $\log_{10}\mathcal{M}_*/M_\odot$>10. A hypothetical impact of the stellar mass distributions of the cluster and field samples would translate into a different behaviour of the variation of the average values of $\mathcal{SFR}$ and $s\mathcal{SFR}$ with environment, which is something we do not observe.

The high cut in $\mathcal{SFR}_{\mathrm{TIR}}$ we use to build the M-FIR galaxy samples translates into a mild increasing trend with z of the median value of the average $\mathcal{SFR}$ ($s\mathcal{SFR}$) for the M-FIR galaxies in the field, which varies with β=0.4±0.2 (β=0.8±0.4). Within the cluster cores, we derive field-like

values of $\mathcal{SFR}$ and $s\mathcal{SFR}$. Also, due to the mentioned $\mathcal{SFR}_{\mathrm{TIR}}$ constraint we are not able to explore whether the M-FIR samples behave in the same way as the UVJ-SF samples. The M-FIR galaxies with suppressed SF are simply missed by the selection function.

A number of works have also identified an offset between the average $\mathcal{SFR}$ ($s\mathcal{SFR}$) in the clusters and in the field (e.g., Patel et al. 2009, Vulcani et al. 2010, Haines et al. 2015, Haines et al. 2013, Paccagnella et al. 2016). Among them, Alberts et al. (2014) find that blue cluster galaxies ($\mathcal{M}_*{\geq}1.3{\times}10^{10}M_\odot$) present systematically lower average $s\mathcal{SFR}_{\mathrm{TIR}}$ up to $z{\sim}1.4$. Their results, derived through a stacking analysis on *Herschel*/SPIRE 250μm imaging of 270 massive galaxy clusters between $z{\sim}0.3$ and 1.5, quantify the average level of SF of the whole star-forming cluster galaxy population, rather than the typical rate of SF of FIR-detected galaxies. In fact, the average $s\mathcal{SFR}$ they retrieve for clusters at $z{\sim}0.5$ and $z{\sim}0.8$ ($\sim$-9.70 and $\sim$-9.50, respectively) are comparable with ours, as well as their 0.2-0.3 dex differences with the field. This systematic suppression of the level of star-forming activity within rich environments is created by the existence of a numerous population of transition galaxies located in the lower part of the well-studied MS of SFGs (e.g., Paccagnella et al. 2016, Coenda et al. 2018). Also, Haines et al. (2013) find a 0.2 dex suppression of the $s\mathcal{SFR}$ in SFGs with $\log_{10}\mathcal{M}_*/M_\odot{>}10$ and $\mathcal{SFR}{>}3\,M_\odot\mathrm{yr}^{-1}$ within $\mathcal{R}_{200}$ at $0.15{<}z{<}0.3$.

If we now focus on the trend with $\mathcal{R}$ in the two last redshift bins, we can see how the average $\mathcal{SFR}$ and $s\mathcal{SFR}$ increase significantly for UVJ-SF galaxies at $0.2{<}\mathcal{R}/R_{200}{<}0.3$, reaching field-like values. This is probably due to the fact that we are reaching the region slightly beyond $0.3R_{200}$, where most of the prototypes of galaxies violently interacting with the ICM are found (e.g., jellyfish galaxies, Poggianti et al. 2016; see Boselli & Gavazzi 2006 and references therein). The average values of $\mathcal{SFR}$ for the cluster M-FIR remain overall compatible with the field values. Instead, the $s\mathcal{SFR}$ depart from the field trend at larger $\mathcal{R}$. However, limited number counts of this sample do not allow to extract robust conclusions about this sample.

9.4 Star formation dependence on individual cluster properties: cool-core and BCG's star formation

In the previous subsections, we have analysed the SF properties of $\mathcal{M}_*$-limited samples of star-forming cluster members detected and undetected in the M- and/or FIR. Even though we are able to identify a trend of the SF indices with redshift, the scatter in the average properties is large. These cluster-to-cluster variations have been observed frequently in the past, and some works have attempted to quantify them (e.g., Alberts et al. 2016). This scatter is likely due to a combination of stochastic processes, such as galaxy mergers (probably, the limited area covered by our study worsens this effect), and differences in the properties of the clusters, such as the dynamical state (e.g., Stroe et al. 2015). In this section, we aim at exploring this latter.

Despite the fact of being selected to be largely relaxed, there is disagreement in the literature on the dynamical state of CLASH sample members (see Rumsey et al. 2016 and references therein). Given that we are focusing our study on the inner cores of clusters, we use as a proxy of the dynamical state of these systems the presence of a CC and the SF activity undergone by their BCGs. Rawle et al. (2012a) found these observables to be strongly correlated, which suggests that the SF activity of the BCGs is influenced by the cluster-scale cooling process. In fact, star-forming BCGs seem to be exclusively found in the centers of CC-clusters. However, the separation between cool- and not-cool-core clusters is challenging. In this work, we use as an indicator of the presence of this feature the parameter $\mathcal{C}$, as defined by Donahue et al. (2016), which is a measure of the concentration of the X-ray emission. More precisely, it gives the ratio between the light within a circular aperture with a 100 kpc radius and the total light enclosed within a circular aperture with a 500 kpc radius. For CC-clusters, $\mathcal{C}$ values are likely $>$0.4 (Donahue et al. 2016). Among the 24 CLASH+HLS clusters, 12 qualify this criterion. As we previously mentioned we find 8 M/FIR-emitter BCGs. Two of them already identified by Rawle et al. (2012a, the remaining 6 are not included in their sample). Among the 8, 7 are characterized by $\mathcal{C}>0.4$ ($\mathcal{C}_{\mathrm{AS1063}}=0.19{\pm}0.03$). In turn, the formation of a CC appears also to be linked to the dynamical states of the clusters, with relaxed clusters exhibiting more likely CC than un-relaxed systems. Although some works have identified distant clusters hosting a CC, their strength at $z{>}0.7$ appears significantly lower due to the expected higher cluster merger rate and their more immature evolutionary state (Santos et al. 2008).

Figure 12 displays, for both the UVJ-SF and the M-FIR samples ($\mathcal{R}/R_{200}{<}0.1$), the relation between the three quantities we use to analyze the SF activity in clusters (i.e., $\mathcal{F}$, $\mathcal{SFR}$, and $s\mathcal{SFR}$) and both the parameter $\mathcal{C}$ and the $\mathcal{SFR}_{\mathrm{UV}}$ of the BCGs extinction corrected ($\mathcal{SFR}_{\mathrm{UVcorr,BCG}}$) provided by Donahue et al. (2015). In order to remove the global trends with redshift of the average $\mathcal{F}$, $\mathcal{SFR}$ and $s\mathcal{SFR}$ that could have an impact on the results, we remove them by normalizing these quantities to the values predicted by the trends fitted for the clusters in the previous subsection at the corresponding redshifts. In each panel of Figure 12, we show the median in three bins of the corresponding x-axis parameter populated by the 33% of the clusters sample. Error bars represent the confidence intervals derived through a bootstrap methodology. In the case of the M-FIR samples, we show with highlighted triangles (black border) the median values of the clusters which contain at least 1 object. We use red triangles for the medians calculated considering upper-limits $\mathcal{SFR}=10M_\odot\mathrm{yr}^{-1}$ (our $\mathcal{SFR}_{\mathrm{TIR}}$ limit for the M-FIR samples) and $s\mathcal{SFR}_{\mathrm{TOT}}=3\times10^{-10}\mathrm{yr}^{-1}$ for those clusters where no M-FIR galaxy is found.

If we focus on the upper panels of Figure 12, we see that the bins of larger $\mathcal{C}$ are marginally dominated by less SFGs. However, the large error bars corresponding to the average of the M-FIR samples in the first $\mathcal{C}$ bin makes the trend not significant for this subsamples. In the middle and bottom panels, we do not find a clear correlation between the average $\mathcal{SFR}$ or the $s\mathcal{SFR}$ and either $\mathcal{C}$ or $\log_{10}\mathcal{SFR}_{\mathrm{UVcorr,BCG}}$.

10   DISCUSSION

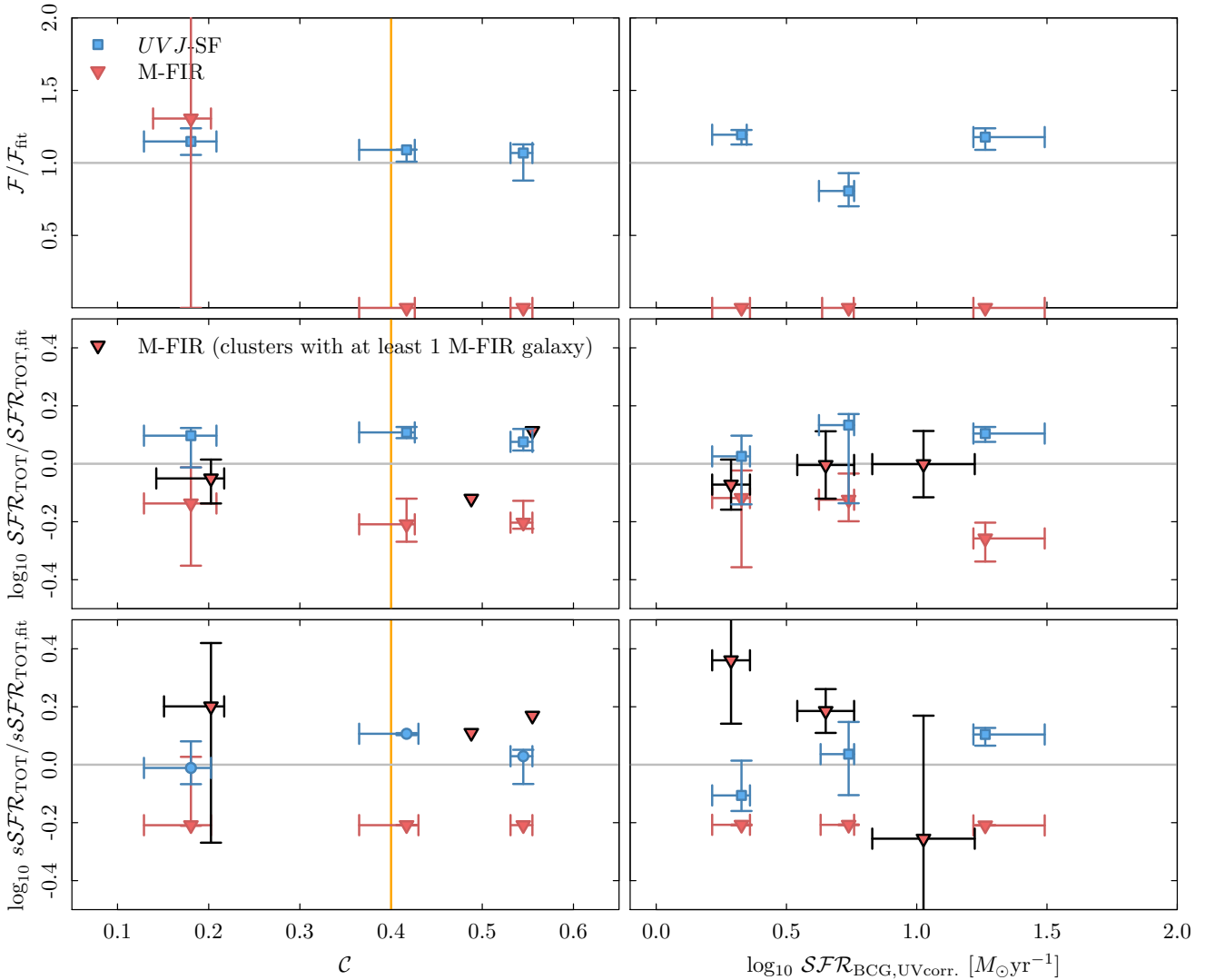It has long been claimed that galaxies quench more efficiently in clusters than in the field (e.g., Butcher & Oemler

Figure 12. Median values of the $\mathcal{F}$, $\mathcal{SFR}_{\rm TOT}$, and $s\mathcal{SFR}_{\rm TOT}$ (top, middle, and bottom panel, respectively) normalized to the values predicted by the cluster trends in Figure 9 and 11 at the corresponding redshifts *vs* the $\mathcal{C}$ coefficient given by Donahue et al. (2015) (indicator of the presence of a CC; left hand panels), and the $\mathcal{SFR}_{\rm UV}$ of the BCG (right panels; Donahue et al. (2015)) corrected for extinction. The vertical yellow line on the left-hand panels represent the value of $\mathcal{C}$ over which the CC are normally located Donahue et al. (2015). We present the averaged values in three equally populated bins of each x-axis parameter. Values derived for the UVJ-SF and M-FIR are shown with blue and red symbols, respectively. We use circles to represent the results including all the clusters. In the case of the clusters where no galaxy was selected in the M-FIR we use an average $\mathcal{SFR}_{\rm TOT}=10M_\odot{\rm yr}^{-1}$ (the $\mathcal{SFR}_{\rm TIR}$ limit of our study), and an average $\log_{10}s\mathcal{SFR}_{\rm TOT}=-9.5$. We use triangles to represent the averages found using only clusters with obscured SF activity in their core (at least 1 M-FIR detected galaxy).

1984, Gerke et al. 2007, Haines et al. 2009, Haines et al. 2013). The general interpretation of this suppression of SF is that environmental processes favour the removal of gas reservoirs from galaxies. In fact, this average deficit of gas in cluster members has been observationally confirmed in star-forming cluster spirals by, e.g., Jablonka et al. (2013). In agreement with this framework, our results clearly display a lack of SF activity in massive cluster cores with respect the field at intermediate redshifts in terms of both the fraction of SFGs and the rates at which they form stars.

The observed significant systematic ∼0.3 dex offsets between clusters and field average $\mathcal{SFR}$ and $s\mathcal{SFR}$ do not ap-

pear to be the result of differences in the SMF of the galaxy samples studied. Supporting this, Guglielmo et al. (2015) find that galaxies of a given mass have different star formation histories depending on their environment, and therefore, it is not the distributions of galaxy masses in clusters the origin of the observed dependence of the SF with the environment. Given that the population of star-forming galaxies within massive clusters at the intermediate redshifts probed is thought to be dominated by infalling field galaxies (Kauffmann 1995), if the quenching of these galaxies were dominated by the same processes that turn galaxies off in the field (leading to the global SF decline in the universe since $z\sim1$-

2; Madau & Dickinson 2014) the fraction of SFGs should decrease proportionally in both environments (Haines et al. 2009). Given the different evolution with redshift we derive for $\mathcal{F}_{UVJ-SF}$ in clusters and field, we can say that we are witnessing the imprint of the impact of environment on the evolution of cluster galaxies ($\mathcal{M}_* > 10^{10} \mathrm{M}_\odot$).

Our results appear to support the observed evolution of the environmental quenching efficiency (van den Bosch et al. 2008, Peng et al. 2010, Balogh et al. 2016), defined as the fraction of passive cluster galaxies which would be still star-forming if they were in the field (Nantais et al. 2017), with a major rise since $z\sim2$ (e.g., Butcher & Oemler 1984, Gerke et al. 2007, Haines et al. 2009, Haines et al. 2013, Alberts et al. 2016).

It is straightforward to wonder what are the processes intrinsic to high density environments that drive the aforementioned galaxy transformation. Some of the most commonly invoked are: *strangulation* (Larson et al. 1980), which consists on the removal of the loosely bound hot halo gas reservoirs by the ICM on long time-scales ($>1\,\mathrm{Gyr}$); the removal of the interstellar medium through interactions with the ICM on moderate/short time-scales ($\lesssim1\,\mathrm{Gyr}$) RPS (Gunn & Gott 1972, Steinhauser et al. 2016); either galaxy-galaxy or galaxy-cluster gravitational interactions, grouped together under the name *harassment* (Moore et al. 1996). The SFGs infalling into high density environments at $z\lesssim1$ are very likely influenced by a combination of these dynamical gas removal processes (see Boselli & Gavazzi 2006, Vulcani et al. 2016). Merger events are probably less frequent in cluster cores at these redshifts, where the high relative velocities hamper reaching the fraction of encounters observed in the field. However, there is growing evidence (e.g., Brodwin et al. 2013, Lotz et al. 2013, Santos et al. 2015, Alberts et al. 2016, Balogh et al. 2016) that at higher redshifts, mergers play the major role in quenching infalling SFGs due to high galaxy space densities and low relative velocities (e.g., Brodwin et al. 2011).

The small scatter ($\sim0.3\,\mathrm{dex}$) found for the MS of SFGs in field samples (e.g., Noeske et al. 2007, Renzini & Peng 2015) is usually interpreted as the consequence of a quenching mechanism that is capable of moving rapidly (0.1 Gyr time-scales) the galaxies out (downward) of the MS. For this reason, the downward offset of the MS found in our work and in other previous studies in clusters (e.g., Haines et al. 2013, Paccagnella et al. 2016) has frequently been interpreted as the imprint of different environmentally-driven quenching mechanisms that could turn off infalling SFGs slowly (e.g., Haines et al. 2013), thus, populating the region below the MS with galaxies on their way to be quenched. The work by Haines et al. (2015), based on the analysis of the actual orbits of infalling galaxies in the 75 most massive clusters in the Millennium Simulation (Springel et al. 2005) support the slow quenching scenario with time-scales ~ 0.7-2 Gyr. The most frequently proposed mechanism for slow quenching in high density environments is strangulation. In this evolving scenario, the decline in star formation is very likely due to *overconsumption* (McGee et al. 2014), the exhaustion of a gas reservoir through star formation and expulsion via modest outflows in the absence of cosmological accretion. Maier et al. (2016) also propose it as the explanation for the higher metallicities found in the accreted cluster galaxies of MACS0416. It has also been invoked to explain the increas-

ing distribution of SFGs with the projected cluster-centric radius (e.g., Alberts et al. 2016, Haines et al. 2015).

However, numerous studies have found observational evidence of rapid quenching mechanisms, such as RPS, that can remove the gas of an infalling galaxy in time-scales of the order of the cluster crossing time ($\lesssim1\,\mathrm{Gyr}$; e.g., Wetzel et al. 2013), playing a significant role building the populations of passive galaxies in clusters at different redshifts. Also, some models of galaxy strangulation (e.g., Boselli et al. 2016 and references therein) and numerical simulations (e.g., McGee et al. 2014) predict extremely long time-scales in order to reproduce the observed lack of SF activity in cluster members, while for instance Boselli et al. (2016) claim that only RPS is able to significantly quench SF activity in galaxies perturbed by high density environments. The contribution of RPS in the core of clusters is thought to be important given the high relative velocities and higher densities of the ICM (e.g., Gunn & Gott 1972). However, this phenomenon operates efficiently for extreme cases of infall in which the orbital velocity is particularly high and the galaxy inclination is perpendicular to the direction of motion (Abadi et al. 1999). Furthermore, RPS can present a fluctuating behaviour which means that galaxies suffering from stripping can present a wide range of properties, as observed by Vulcani et al. (2016) and Vulcani et al. (2017).

As an alternative to the slow/fast dichotomy frequently discussed, Wetzel et al. (2013) propose a delayed-then-rapid quenching scenario, in which the satellites $\mathcal{SFR}$s evolve unaffected for 2-4 Gyr after infall, and are eventually quenched rapidly, with an e-folding time of <0.8 Gyr. This scenario has been frequently embraced to conciliate the observations of smaller fractions of SFGs in clusters and values of $\mathcal{SFR}$ comparable to those in the field at the same redshift.

In addition, Wetzel et al. (2013) propose the quenching time-scales do not depend on the halo mass. Interestingly, they claim that up to half of quenched satellites in massive clusters is the result of quenching in infalling groups, namely, *pre-processing*. Other authors have highlighted the importance of this phenomenon to explain the properties of galaxy populations of intermediate redshift clusters (e.g., Haines et al. 2015, Ogrean et al. 2015). The cluster-centric distances we probe in this work ($\mathcal{R}/R_{200}<0.3$) do not allow the assessment of pre-processing.

In this context, our results favour slow quenching mechanisms (e.g., strangulation) to be dominating the evolution of the observed UVJ-SF cluster core galaxies with $\log_{10}\mathcal{M}_*/M_\odot>10$ throughout the last 8 Gyr. This is because these samples appear to be heavily populated by transition galaxies observed while they quench (Paccagnella et al. 2016). However, we cannot rule out the contribution of fast processes such as RPS to the enhanced fraction of quenched galaxies observed. We also note that our methodology cannot directly select galaxies quenching on short time-scales, such as PSB (e.g., Poggianti et al. 2004, Tran et al. 2007, Muzzin et al. 2014, Paccagnella et al. 2017), as this would require spectral information, which we lack for more than half of our clusters sample.

11 SUMMARY & CONCLUSIONS

We have presented a detailed analysis of the SF activity within 24 massive clusters cores at $0.2 \lesssim z \lesssim 0.9$ targeted by the HLS and CLASH surveys. The deep multi-wavelength photometric dataset on these fields cover the whole rest-frame UV-to-FIR regimes. In particular, we have made use of the CLASH catalogues, which contain photometry measured on *HST* ACS/WFC (F435W, F475W, F606W, F625W, F775W, F814W, and F850LP), WFC3/UVIS (F225W, F275W, F336W, and F390W), and WFC3/IR (F105W, F110W, F125W, F140W, and F160W) imaging. Then, we have combined these catalogues with others built on *Spitzer* IRAC (3.6, 4.5, 5.8, and 8.0 μm) and MIPS (24μm) bands, and *Herschel* PACS (100, and 160 μm) and SPIRE (250, 350, and 500 μm), deblending the former in the position of the CLASH catalogues and selecting the most probable UV/optical counterpart for the sources in the rest MIR and FIR bands. Finally, we have also gathered the spectroscopic information available on these fields, mainly released by CLASH-VLT and GLASS surveys. Consequently, we have derived high quality photometric redshifts (σ_{NMAD}=0.04, and 8% of outliers) fitting the UV-to-NIR photometry with the EAZYcode. We have selected cluster members by applying either a spectroscopic redshift criterion or a probabilistic methodology that takes into account the whole information included in the PDF of the photometric redshift estimation. We have used the z_{phot} derived and the Rainbow Cosmological Database software package to fit, on the one hand, the optical/NIR photometry (CLASH & IRAC), and on the other hand, the FIR photometry (MIPS & *Herschel*). In this way, we have estimated the physical properties of the cluster members such as their $\mathcal{M}_*$ and the rates at which they form stars (as traced by the UV and FIR emission independently). With the aim of building up analogous field samples with which compare the results on clusters, we have applied the same analysis and selection criteria on three CANDELS fields. Finally, we have used samples of SFGs ($\mathcal{M}_* > 10^{10} M_\odot$) selected using the UVJ-diagram (UVJ-SF samples) to evaluate and compare the SF processes in high density environments and the field. Furthermore, we have used samples of galaxies ($\mathcal{M}_* > 10^{10} M_\odot$) detected in the MIR and/or FIR with $\mathcal{SFR}_{\mathrm{TIR}} > 10 M_\odot \mathrm{yr}^{-1}$ (M-FIR samples) to explore the obscured SF activity. Taking advantage of the rich dataset available, we have based our results on the quantification of the total SF, defined as either the sum of the SF traced by the rest-frame UV emission and the FIR, or the un-obscured SF (traced only by the rest-frame UV) corrected for the dust extinction with our own optimized recipe.

The main results and conclusions of our work can be summarized in the following points:

• The SF activity in the inner regions of intermediate-z clusters appears to be suppressed in terms of both the fraction of SFGs and the rate at which they turn gas into stars.

• We derive average fractions of UVJ-SF galaxies a factor $\sim$2 smaller in cluster ($\mathcal{R}/R_{200}$<0.1) than in the field across. The average fraction of M-FIR cluster members ($\mathcal{R}/R_{200}$<0.1) is negligible but compatible with a factor $\sim$2 smaller in clusters.

• We identify increasing trends of $\mathcal{F}_{UVJ-\mathrm{SF}}$ and $\mathcal{F}_{\mathrm{M-FIR}}$

with z, which evolve faster within clusters (β=1.1$\pm$0.6 and β=7.3$\pm$5.8, respectively, at $\mathcal{R}/R_{200}$<0.1) than in the field (β=0.2$\pm$0.3 and β=0.2$\pm$0.5, respectively).

• UVJ-SF cluster members ($\mathcal{R}/R_{200}$<0.1) present $\mathcal{SFR}$ and $s\mathcal{SFR}$ typically $\sim$0.3 dex smaller than UVJ-SF field galaxies. Average $\mathcal{SFR}$ and $s\mathcal{SFR}$ values evolve similarly (within the error bars) in clusters, with β=1.3$\pm$1.0 and β=1.2$\pm$0.9, respectively. The evolution in the field is described by β=2.6$\pm$0.2 and β=2.4$\pm$0.4, respectively. Due to the high $\mathcal{SFR}_{\mathrm{TIR}}$s completeness value given *Spitzer*/MIPS 24μm and *Herschel* imaging used in this study, we can not explore whether is there a different trend between field and clusters dusty SFGs in the average $\mathcal{SFR}$ and $s\mathcal{SFR}$.

• We find increasing SF activity with cluster-centric distance out to $\mathcal{R}/R_{200}$=0.3 in terms of the average $\mathcal{SFR}$ and $s\mathcal{SFR}$ of the UVJ-SF sample. No clear trend is found, however, for the fraction of SFGs.

• We do not find an obvious relationship between SF activity in clusters and the presence of a CC or a BCG forming stars actively.

Our results evidence the impact of the cluster environment on the evolution of its inhabitants and favour a dominant role of physical processes quenching galaxies slowly. The mechanism typically invoked in these cases is strangulation. This process appears to be responsible for the shift of the average $\mathcal{SFR}/s\mathcal{SFR}$ exhibited by SFGs in high density environments since $z \sim 0.9$, which is interpreted as the evidence of the existence of a large population of transition galaxies below the MS, on their way to be quenched. However, we can not rule out the impact of other processes occurring at shorter time-scales, such as RPS, which could be partially responsible for a fraction of the SFGs missing in this clusters.

We release the multi-wavelength photometry, photometric redshifts, and physical properties of the star-forming cluster members associated to this paper through the Rainbow Cosmological Database.

REFERENCES

Abadi M. G., Moore B., Bower R. G., 1999, MNRAS, 308, 947
Abazajian K. N., et al., 2009, ApJS, 182, 543
Abell G. O., 1958, ApJS, 3, 211
Abell G. O., Corwin Jr. H. G., Olowin R. P., 1989, ApJS, 70, 1
Alberts S., et al., 2013, MNRAS, 431, 194
Alberts S., et al., 2014, MNRAS, 437, 437
Alberts S., et al., 2016, ApJ, 825, 72
Annunziatella M., et al., 2014, A&A, 571, A80
Annunziatella M., et al., 2016, A&A, 585, A160
Ashby M. L. N., et al., 2013, ApJS, 209, 22
Ashby M. L. N., et al., 2015, ApJS, 218, 33
Bai L., Rieke G. H., Rieke M. J., Christlein D., Zabludoff A. I., 2009, ApJ, 693, 1840
Baldry I. K., Glazebrook K., Brinkmann J., Ivezić Ž., Lupton R. H., Nichol R. C., Szalay A. S., 2004, ApJ, 600, 681
Baldry I. K., Balogh M. L., Bower R. G., Glazebrook K., Nichol R. C., Bamford S. P., Budavari T., 2006, MNRAS, 373, 469
Baldry I. K., et al., 2012, MNRAS, 421, 621
Balestra I., et al., 2016, ApJS, 224, 33
Balogh M. L., Christlein D., Zabludoff A. I., Zaritsky D., 2001, ApJ, 557, 117
Balogh M. L., et al., 2016, MNRAS, 456, 4364
Barger A. J., Cowie L. L., Wang W.-H., 2008, ApJ, 689, 687
Barro G., et al., 2011a, ApJS, 193, 13
Barro G., et al., 2011b, ApJS, 193, 30
Bell E. F., et al., 2004, ApJ, 608, 752
Bell E. F., et al., 2005, ApJ, 625, 23
Berrier J. C., Stewart K. R., Bullock J. S., Purcell C. W., Barton E. J., Wechsler R. H., 2009, ApJ, 690, 1292
Bertin E., Arnouts S., 1996, A&AS, 117, 393
Biviano A., Fadda D., Durret F., Edwards L. O. V., Marleau F., 2011, A&A, 532, A77
Biviano A., et al., 2013, A&A, 558, A1
Blanton M. R., Roweis S., 2007, AJ, 133, 734
Boselli A., Gavazzi G., 2006, PASP, 118, 517
Boselli A., et al., 2016, A&A, 596, A11
Brammer G. B., van Dokkum P. G., Coppi P., 2008, ApJ, 686, 1503
Brammer G. B., et al., 2011, ApJ, 739, 24
Brodwin M., et al., 2011, ApJ, 732, 33
Brodwin M., et al., 2013, ApJ, 779, 138
Brunner R. J., Lubin L. M., 2000, AJ, 120, 2851
Butcher H., Oemler Jr. A., 1978, ApJ, 219, 18
Butcher H., Oemler Jr. A., 1984, ApJ, 285, 426
Calzetti D., 1997, AJ, 113, 162
Calzetti D., Kinney A. L., Storchi-Bergmann T., 1994, ApJ, 429, 582
Calzetti D., Armus L., Bohlin R. C., Kinney A. L., Koornneef J., Storchi-Bergmann T., 2000, ApJ, 533, 682
Capak P., et al., 2004, AJ, 127, 180
Cava A., et al., 2009, A&A, 495, 707
Chabrier G., 2003, PASP, 115, 763
Chary R., Elbaz D., 2001, ApJ, 556, 562
Cimatti A., et al., 2008, A&A, 482, 21
Coe D., et al., 2012, ApJ, 757, 22
Coenda V., Martínez H. J., Muriel H., 2018, MNRAS, 473, 5617
Cohen J. G., Kneib J.-P., 2002, ApJ, 573, 524
Connor T., et al., 2017, ApJ, 848, 37
Conroy C., Gunn J. E., White M., 2009, ApJ, 699, 486
Cooke E. A., et al., 2016, ApJ, 816, 83
Cooper M. C., et al., 2011, ApJS, 193, 14
Coppin K. E. K., et al., 2011, MNRAS, 416, 680
Cowie L. L., Barger A. J., Hu E. M., Capak P., Songaila A., 2004, AJ, 127, 3137
Dale D. A., Helou G., 2002, ApJ, 576, 159

Darvish B., Mobasher B., Sobral D., Rettura A., Scoville N., Faisst A., Capak P., 2016, ApJ, 825, 113
Darvish B., Mobasher B., Martin D. C., Sobral D., Scoville N., Stroe A., Hemmati S., Kartaltepe J., 2017, ApJ, 837, 16
De Lucia G., et al., 2007, MNRAS, 374, 809
Dickinson M., et al., 2003, Great Observatories Origins Deep Survey (GOODS) Validation Observations, Spitzer Proposal
Domínguez Sánchez H., et al., 2016, MNRAS, 457, 3743
Donahue M., et al., 2015, ApJ, 805, 177
Donahue M., et al., 2016, ApJ, 819, 36
Draine B. T., Li A., 2007, ApJ, 657, 810
Dressler A., 1980, ApJ, 236, 351
Dressler A., et al., 1997, ApJ, 490, 577
Dressler A., Rigby J., Oemler Jr. A., Fritz J., Poggianti B. M., Rieke G., Bai L., 2009, ApJ, 693, 140
Drory N., et al., 2009, ApJ, 707, 1595
Duc P.-A., et al., 2002, A&A, 382, 60
Ebeling H., Edge A. C., Henry J. P., 2001, ApJ, 553, 668
Ebeling H., Barrett E., Donovan D., Ma C.-J., Edge A. C., van Speybroeck L., 2007, ApJ, 661, L33
Ebeling H., Edge A. C., Mantz A., Barrett E., Henry J. P., Ma C. J., van Speybroeck L., 2010, MNRAS, 407, 83
Ebeling H., Ma C.-J., Barrett E., 2014, ApJS, 211, 21
Egami E., et al., 2010, A&A, 518, L12
Eisenhardt P. R. M., et al., 2008, ApJ, 684, 905
Elbaz D., et al., 2011, A&A, 533, A119
Evrard A. E., Metzler C. A., Navarro J. F., 1996, ApJ, 469, 494
Fabian A. C., 1994, ARA&A, 32, 277
Fadda D., Elbaz D., Duc P.-A., Flores H., Franceschini A., Cesarsky C. J., Moorwood A. F. M., 2000, A&A, 361, 827
Fernández-Soto A., Lanzetta K. M., Chen H.-W., Levine B., Yahata N., 2002, MNRAS, 330, 889
Finn R. A., et al., 2010, ApJ, 720, 87
Fioc M., Rocca-Volmerange B., 1997, A&A, 326, 950
Geach J. E., et al., 2006, ApJ, 649, 661
Geller M. J., Hwang H. S., Diaferio A., Kurtz M. J., Coe D., Rines K. J., 2014, ApJ, 783, 52
Gerke B. F., et al., 2007, MNRAS, 376, 1425
Giavalisco M., et al., 2004, ApJ, 600, L93
Girardi M., et al., 2015, A&A, 579, A4
Gómez P. L., et al., 2012, AJ, 144, 79
Grazian A., et al., 2006, A&A, 449, 951
Griffin M. J., et al., 2010, A&A, 518, L3
Grillo C., et al., 2015, ApJ, 800, 38
Grogin N. A., et al., 2011, ApJS, 197, 35
Guglielmo V., Poggianti B. M., Moretti A., Fritz J., Calvi R., Vulcani B., Fasano G., Paccagnella A., 2015, MNRAS, 450, 2749
Gunn J. E., Gott III J. R., 1972, ApJ, 176, 1
Guo Y., et al., 2013, ApJS, 207, 24
Haines C. P., Gargiulo A., La Barbera F., Mercurio A., Merluzzi P., Busarello G., 2007, MNRAS, 381, 7
Haines C. P., et al., 2009, ApJ, 704, 126
Haines C. P., et al., 2013, ApJ, 775, 126
Haines C. P., et al., 2015, ApJ, 806, 101
Haines C. P., et al., 2017, A&A, 605, A4
Hoaglin D. C., Mosteller F., Tukey J. W., 1983, Understanding robust and exploratory data anlysis
Huang J.-S., et al., 2004, ApJS, 154, 44
Huchra J. P., et al., 2012, ApJS, 199, 26
Ilbert O., et al., 2009, ApJ, 690, 1236
Jablonka P., Combes F., Rines K., Finn R., Welch T., 2013, A&A, 557, A103
Jouvel S., et al., 2014, A&A, 562, A86
Kajisawa M., et al., 2009, ApJ, 702, 1393
Karman W., et al., 2015, A&A, 574, A11
Kauffmann G., 1995, MNRAS, 274, 153
Kauffmann G., et al., 2003, MNRAS, 341, 33

Kawinwanichakij L., et al., 2017, ApJ, 847, 134
Kennicutt Jr. R. C., 1998, ARA&A, 36, 189
Kennicutt R. C., Evans N. J., 2012, ARA&A, 50, 531
Kimm T., et al., 2009, MNRAS, 394, 1131
Kocevski D. D., et al., 2011, ApJ, 736, 38
Koekemoer A. M., et al., 2011, ApJS, 197, 36
Larson R. B., Tinsley B. M., Caldwell C. N., 1980, ApJ, 237, 692
Le Fèvre O., et al., 2003, in Iye M., Moorwood A. F. M., eds, Society of Photo-Optical Instrumentation Engineers (SPIE) Conference Series Vol. 4841, Instrument Design and Performance for Optical/Infrared Ground-based Telescopes. pp 1670–1681, doi:10.1117/12.460959
Le Fèvre O., et al., 2004, A&A, 428, 1043
Le Fèvre O., et al., 2015, A&A, 576, A79
Lewis I., et al., 2002, MNRAS, 334, 673
Lin L., et al., 2014, ApJ, 782, 33
Lotz J. M., et al., 2013, ApJ, 773, 154
Lotz J. M., et al., 2017, ApJ, 837, 97
Lupton R., Blanton M. R., Fekete G., Hogg D. W., O'Mullane W., Szalay A., Wherry N., 2004, PASP, 116, 133
Lutz D., et al., 2011, A&A, 532, A90
Madau P., Dickinson M., 2014, ARA&A, 52, 415
Magnelli B., et al., 2013, A&A, 553, A132
Maier C., et al., 2016, A&A, 590, A108
Mann A. W., Ebeling H., 2012, MNRAS, 420, 2120
Marcillac D., Rigby J. R., Rieke G. H., Kelly D. M., 2007, ApJ, 654, 825
Martis N. S., et al., 2016, ApJ, 827, L25
McGee S. L., Bower R. G., Balogh M. L., 2014, MNRAS, 442, L105
Mercurio A., Girardi M., Boschin W., Merluzzi P., Busarello G., 2003, A&A, 397, 431
Meurer G. R., Heckman T. M., Calzetti D., 1999, ApJ, 521, 64
Mignoli M., et al., 2005, A&A, 437, 883
Molino A., et al., 2017, MNRAS, 470, 95
Moore B., Katz N., Lake G., Dressler A., Oemler A., 1996, Nature, 379, 613
Mortlock A., et al., 2015, MNRAS, 447, 2
Moutard T., Sawicki M., Arnouts S., Golob A., Malavasi N., Adami C., Coupon J., Ilbert O., 2018, MNRAS, 479, 2147
Muzzin A., et al., 2014, ApJ, 796, 65
Nantais J. B., et al., 2016, A&A, 592, A161
Nantais J. B., et al., 2017, MNRAS, 465, L104
Nayyeri H., et al., 2017, ApJS, 228, 7
Newman A. B., Treu T., Ellis R. S., Sand D. J., Nipoti C., Richard J., Jullo E., 2013, ApJ, 765, 24
Noeske K. G., et al., 2007, ApJ, 660, L43
Ogrean G. A., et al., 2015, ApJ, 812, 153
Oliver S. J., et al., 2012, MNRAS, 424, 1614
Paccagnella A., et al., 2016, ApJ, 816, L25
Paccagnella A., et al., 2017, ApJ, 838, 148
Pacifici C., Charlot S., Blaizot J., Brinchmann J., 2012, MNRAS, 421, 2002
Papovich C., et al., 2018, ApJ, 854, 30
Patel S. G., Holden B. P., Kelson D. D., Illingworth G. D., Franx M., 2009, ApJ, 705, L67
Pelló R., et al., 2009, A&A, 508, 1173
Peng Y.-j., et al., 2010, ApJ, 721, 193
Pérez-González P. G., et al., 2005, ApJ, 630, 82
Pérez-González P. G., et al., 2008, ApJ, 675, 234
Pérez-González P. G., et al., 2010, A&A, 518, L15
Pérez-González P. G., et al., 2013, ApJ, 762, 46
Pilbratt G. L., et al., 2010, A&A, 518, L1
Poggianti B. M., 2003, Ap&SS, 285, 121
Poggianti B. M., Smail I., Dressler A., Couch W. J., Barger A. J., Butcher H., Ellis R. S., Oemler Jr. A., 1999, ApJ, 518, 576
Poggianti B. M., Bridges T. J., Komiyama Y., Yagi M., Carter D., Mobasher B., Okamura S., Kashikawa N., 2004, ApJ, 601, 197
Poggianti B. M., et al., 2009, ApJ, 693, 112
Poggianti B. M., et al., 2016, AJ, 151, 78
Poggianti B. M., et al., 2017, ApJ, 844, 48
Poglitsch A., et al., 2010, A&A, 518, L2
Polletta M., et al., 2007, ApJ, 663, 81
Popesso P., et al., 2011, A&A, 532, A145
Popping G., Puglisi A., Norman C. A., 2017, MNRAS, 472, 2315
Postman M., et al., 2012, ApJS, 199, 25
Quadri R. F., Williams R. J., Franx M., Hildebrandt H., 2012, ApJ, 744, 88
R Core Team 2017, R: A Language and Environment for Statistical Computing. R Foundation for Statistical Computing, Vienna, Austria, https://www.R-project.org/
Ravindranath S., Ho L. C., 2002, ApJ, 577, 133
Rawle T. D., et al., 2010, A&A, 518, L14
Rawle T. D., et al., 2012a, ApJ, 747, 29
Rawle T. D., et al., 2012b, ApJ, 756, 106
Rawle T. D., et al., 2014, MNRAS, 442, 196
Rawle T. D., et al., 2016, MNRAS, 459, 1626
Renzini A., Peng Y.-j., 2015, ApJ, 801, L29
Rex M., et al., 2010, A&A, 518, L13
Rieke G. H., Alonso-Herrero A., Weiner B. J., Pérez-González P. G., Blaylock M., Donley J. L., Marcillac D., 2009, ApJ, 692, 556
Rodighiero G., et al., 2011, ApJ, 739, L40
Rosati P., et al., 2014, The Messenger, 158, 48
Rumsey C., et al., 2016, MNRAS, 460, 569
Saintonge A., Tran K.-V. H., Holden B. P., 2008, ApJ, 685, L113
Salpeter E. E., 1955, ApJ, 121, 161
Sanders D. B., et al., 2007, ApJS, 172, 86
Santos J. S., Rosati P., Tozzi P., Böhringer H., Ettori S., Bignamini A., 2008, A&A, 483, 35
Santos J. S., et al., 2015, MNRAS, 447, L65
Sargent M. T., Béthermin M., Daddi E., Elbaz D., 2012, ApJ, 747, L31
Schechter P., 1976, ApJ, 203, 297
Schmidt K. B., et al., 2014, ApJ, 782, L36
Schreiber C., Pannella M., Leiton R., Elbaz D., Wang T., Okumura K., Labbé I., 2017, A&A, 599, A134
Scoville N., et al., 2007, ApJS, 172, 1
Shectman S. A., Landy S. D., Oemler A., Tucker D. L., Lin H., Kirshner R. P., Schechter P. L., 1996, ApJ, 470, 172
Sheth R. K., Rossi G., 2010, MNRAS, 403, 2137
Smith R. J., et al., 2010, MNRAS, 408, 1417
Springel V., et al., 2005, Nature, 435, 629
Steinhauser D., Schindler S., Springel V., 2016, A&A, 591, A51
Stroe A., et al., 2015, MNRAS, 450, 646
Sunyaev R. A., Zel'dovich Y. B., 1972, Comments on Astrophysics and Space Physics, 4, 173
Szokoly G. P., et al., 2004, ApJS, 155, 271
Tran K.-V. H., Franx M., Illingworth G. D., van Dokkum P., Kelson D. D., Blakeslee J. P., Postman M., 2007, ApJ, 661, 750
Treu T., et al., 2015, ApJ, 812, 114
Tyler K. D., Rieke G. H., Bai L., 2013, ApJ, 773, 86
Umetsu K., et al., 2014, ApJ, 795, 163
Vanzella E., et al., 2008, A&A, 478, 83
Vulcani B., Poggianti B. M., Finn R. A., Rudnick G., Desai V., Bamford S., 2010, ApJ, 710, L1
Vulcani B., et al., 2011, MNRAS, 412, 246
Vulcani B., et al., 2012, MNRAS, 420, 1481
Vulcani B., et al., 2013, A&A, 550, A58
Vulcani B., et al., 2016, ApJ, 833, 178
Vulcani B., et al., 2017, ApJ, 837, 126
Wang W.-H., Cowie L. L., Barger A. J., Keenan R. C., Ting H.-C., 2010, ApJS, 187, 251

Wetzel A. R., Tinker J. L., Conroy C., van den Bosch F. C., 2013, MNRAS, 432, 336

Whitaker K. E., Kriek M., van Dokkum P. G., Bezanson R., Brammer G., Franx M., Labbé I., 2012a, ApJ, 745, 179

Whitaker K. E., van Dokkum P. G., Brammer G., Franx M., 2012b, ApJ, 754, L29

Whitaker K. E., et al., 2015, ApJ, 811, L12

Wijesinghe D. B., et al., 2012, MNRAS, 423, 3679

Williams R. J., Quadri R. F., Franx M., van Dokkum P., Labbé I., 2009, ApJ, 691, 1879

Wirth G. D., et al., 2004, AJ, 127, 3121

Wittman D., Bhaskar R., Tobin R., 2016, MNRAS, 457, 4005

Wuyts S., et al., 2007, ApJ, 655, 51

Wuyts S., Labbé I., Förster Schreiber N. M., Franx M., Rudnick G., Brammer G. B., van Dokkum P. G., 2008, ApJ, 682, 985

Zitrin A., et al., 2013, ApJ, 762, L30

Zitrin A., et al., 2015, ApJ, 801, 44

van den Bosch F. C., Aquino D., Yang X., Mo H. J., Pasquali A., McIntosh D. H., Weinmann S. M., Kang X., 2008, MNRAS, 387, 79

van der Burg R. F. J., et al., 2013, A&A, 557, A15

van der Burg R. F. J., McGee S., Aussel H., Dahle H., Arnaud M., Pratt G. W., Muzzin A., 2018, preprint, (arXiv:1807.00820)

APPENDIX A: DATA AVAILABLE ON THE CANDELS FIELDS

In the following subsections we briefly enumerate the photometric and spectroscopic data on the CANDELS fields which is used in our analysis.

A1   GOODS-S

We use the multi-wavelength catalogue on the CANDELS/GOODS-S field published by Guo et al. (2013), which combines the CANDELS *HST*/WFC3 F105W, F125W, and F160W bands with data from UV (*U* band from both CTIO/MOSAIC and VLT/VIMOS), optical (*HST*/ACS F435W, F606W, F775W, F814W, and F850LP), and infrared (*HST*/WFC3 F098M, VLT/ISAAC *Ks*, VLT/HAWK-I *Ks*, and *Spitzer*/IRAC 3.6, 4.5, 5.8, 8.0 μm) observations. The catalogue is based on source detection in the WFC3 F160W band. Applying the methodology described in Section 3 we complement the catalogue with MIR photometry in *Spitzer*/MIPS 24 μm and 70 μm from (Pérez-González et al. 2008) and FIR photometry from the GOODS-Herschel (Elbaz et al. 2011) and PEP (Magnelli et al. 2013) surveys, including PACS 100 and 160 μm, and SPIRE 250, 350, and 500 μm. The spectroscopic data are gathered from the VIMOS VLT deep survey (Le Fèvre et al. 2004), Szokoly et al. (2004), the K20 survey (Mignoli et al. 2005), and other surveys such as those carried out by (e.g.) Cimatti et al. (2008), Vanzella et al. (2008). See Guo et al. (2013) for the details.

A2   GOODS-N

The multi-wavelength catalogue used on CANDELS/GOODS-N is built and described by Barro et al. (in prep.) and includes UV to far IR and radio data. In particular, UV data from GALEX (PI C. Martin), ground-based optical data from *U* to *z* bands taken by the *Kitt Peak* telescope and from the *Subaru*/Suprime-Cam

as part of the Hawaii Hubble Deep Field North project (Capak et al. 2004), 25 medium-bands from the GTC SHARDS (Pérez-González et al. 2013) survey, *J*, *H*, and *Ks* imaging from the Subaru MOIRCS deep survey (Kajisawa et al. 2009) and CFHT/WIRCam *Ks* photometry (Lin in prep.); IRAC 3.6, 4.5, 5.8, 8.0 μm maps, maps from Spitzer-GOODS (Dickinson et al. 2003), SEDS (Ashby et al. 2013) and SCANDELS (Ashby et al. 2015); MIPS data from FIDEL (PI: M. Dickinson); Herschel from the GOODS-Herschel (Elbaz et al. 2011) and PEP (Magnelli et al. 2013) surveys, including PACS 100 and 160 μm, and SPIRE 250, 350, and 500 μm. The spectroscopic redshifts used are a compilation based primarily on ACS-GOODS redshift survey (Cowie et al. 2004; Barger et al. 2008), the Team Keck Redshift Survey (Wirth et al. 2004), and the DEEP3 galaxy redshift survey (Cooper et al. 2011).

A3   COSMOS

We use the multi-wavelength catalogue on the CANDELS/COSMOS field published by Nayyeri et al. (2017), which combines the CANDELS *HST*/WFC3 F105W, F125W, and F160W bands with data from *HST*/ACS F606W and F814W, CFHT/MegaPrime in the u^*, g^*, r^*, i^*, and z^* bands, from the *Subaru*/Suprime-Cam in the B, g^+, V, r^+, i^+ and z^+, along with twelve intermediate and two narrow bands (∼4000-8500 Å), from the VLT/VISTA in the Y, J, H and Ks bands, *Mayall*/NEWFIRM J_1, J_2, J_3, H_1, H_2, K, and *Spitzer*/IRAC 3.6, 4.5, 5.8, 8.0 μm bands. Again, we combine this catalogue with MIR photometry in *Spitzer*/MIPS 24 μm and 70 μm from Sanders et al. (2007) and FIR photometry including PACS 100 and 160 μm from PEP program (Lutz et al. 2011), and SPIRE 250, 350, and 500 μm from HerMES (Oliver et al. 2012). Among the spectroscopic surveys gathered we highlight the VIMOS Ultra Deep Survey (Le Fèvre et al. 2015), zCOSMOS (PI: S. Lilly).

APPENDIX B: UV CORRECTION

The ratio of the $\mathcal{L}_{\mathrm{TIR}}$ to $\mathcal{L}_{\mathrm{UV}}$, usually referred as $\mathcal{IRX}$, is tightly related to the dust attenuation in a galaxy. This is because dust absorbs and scatters mainly UV photons obscuring and reddening the galaxy SED at wavelengths ≲1μm. Then, it re-emits the absorbed energy in the IR, at wavelengths ∼1-1000μm. Since the work of Meurer et al. (1999) on local starburst galaxies (i.e., extreme SFGs), the relation between the $\mathcal{IRX}$ and the slope of the UV (β) has been frequently used to estimate the UV dust attenuation of galaxies. In practice, this relation is calibrated for local blue galaxies for which FIR observations is available (e.g., Calzetti 1997, Meurer et al. 1999) and then, it is used to correct the UV luminosity from extinction up to high redshifts (Meurer et al. 1999). However, important deviations from these relations have been observed (e.g.) for galaxies forming stars at a lower rates or at different redshifts. Lately, different studies have explored in detailed the physical origin of variations in the $\mathcal{IRX}$-β relation (e.g., Popping et al. 2017). In this context, we aim at deriving an optimized dust attenuation correction (i.e. $\mathcal{IRX}$-β relation) that we can apply to those star-forming cluster members fainter than our observational limits in MIPS and/or Herschel, and therefore
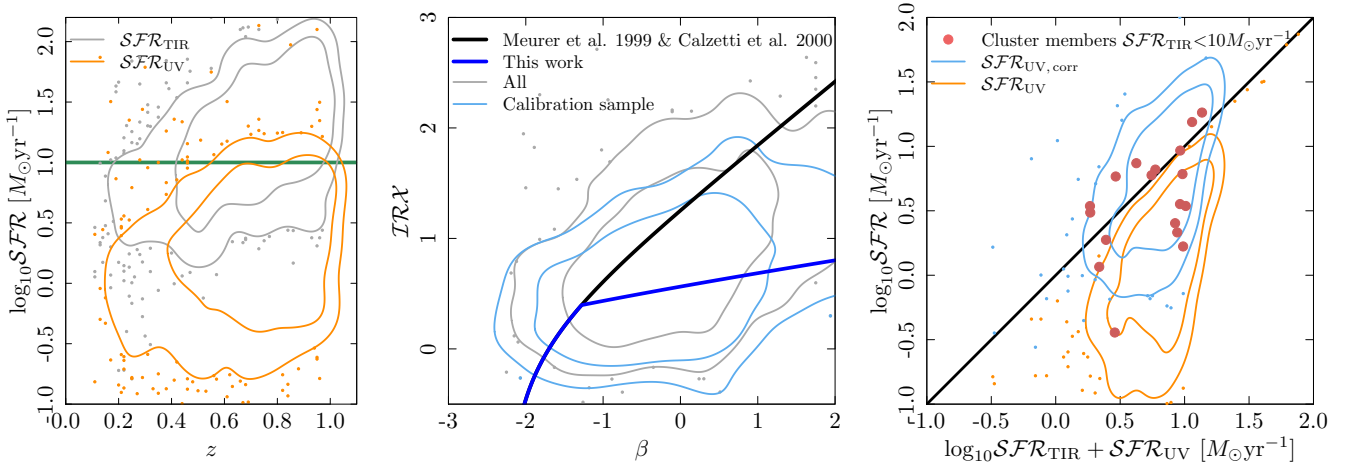
Figure 1. *Left panel*: $\mathcal{SFR}_{\mathrm{TIR}}$ (grey contours) and $\mathcal{SFR}_{\mathrm{UV}}$ (orange contours) versus redshift for all the 1548 M/FIR-detected galaxies in CANDELS fields with UVJ colours corresponding to SFGs, $\log_{10}\mathcal{M}_*/M_\odot>10$, and $0.1< z <1.0$. The green line represents the selection criteria for the selection of the calibration sample. *Central panel*: $\mathcal{IRX}$-β relation for the galaxies in CANDELS fields with UVJ colours corresponding to SFGs, $\log_{10}\mathcal{M}_*/M_\odot>10$, and $0.1< z <1.0$ (grey contours), and the 525 galaxies with $\mathcal{SFR}_{\mathrm{TIR}}<10\,M_\odot\mathrm{yr}^{-1}$ of which the calibration sample is made of (blue contours). We represent our calibration with a blue line. The black line is the $\mathcal{IRX}$-β fit from Meurer et al. (1999) modified with a Calzetti et al. (2000) extinction law to the UV wavelength we consider in our study (2800Å). *Right panel*: Comparison between $\mathcal{SFR}_{\mathrm{TIR}} + \mathcal{SFR}_{\mathrm{UV}}$ and the $\mathcal{SFR}_{\mathrm{UV,corr.}}$ corrected for dust extinction using our own calibration (Equation B1, blue contours). For comparison we show the distribution of values of $\mathcal{SFR}_{UV}$ previous to the dust extinction correction (orange contours). To evaluate the behaviour of our UV correction in the clusters, we represent the comparison between the $\mathcal{SFR}_{\mathrm{TOT}}$ and the $\mathcal{SFR}_{\mathrm{UV,corr.}}$ of the cluster members with $\mathcal{SFR}_{\mathrm{TIR}}<10 M_\odot\mathrm{yr}^{-1}$.

presumably less star-forming than the starbursts on which the calibrations in the literature are defined.

Following a similar approach to Domínguez Sánchez et al. (2016), we basically derive a $\mathcal{IRX}$-β relation for a sample of SFGs which are faint M/FIR emitters. In particular, we take advantage of the deep coverage on CANDELS fields (GOODS and COSMOS) to select a subsample of SFGs fainter than the CLASH+HLS fields observational limits in MIPS and/or *Herschel* bands. We only consider galaxies classified as SFGs using an UVJ-diagram, located in the redshift range between 0.1 and 1.0, and with $\mathcal{M}_*/M_\odot>10$. In Figure 1 (left panel) we display the distribution with redshift of $\mathcal{SFR}_{\mathrm{TIR}}$ and $\mathcal{SFR}_{\mathrm{UV}}$ of these galaxies (obtained following Equation 5 and 6, respectively). The calibration sample includes the 1548 galaxies with $\mathcal{SFR}_{\mathrm{TIR}}<10 M_\odot\mathrm{yr}^{-1}$ (green horizontal line).

Once the sample is defined, we compute the UV slope for each galaxy using a linear interpolation between 1500 Å and 2800 Å in the best-fit templates given by RAIN-BOW (Section 5). The typical uncertainty in the β values is $\sim$20%. Then, we compute their $\mathcal{IRX}$ as the ratio of their $\mathcal{SFR}_{\mathrm{TIR}}$ and $\mathcal{SFR}_{\mathrm{UV}}$. In Figure 1 (central panel) we display the $\mathcal{IRX}$-β space for the whole field sample of M/FIR emitters ($\mathcal{M}_*/M_\odot>10$ and $0.2<z<1.0$; grey contours), and the calibration sample of faint M/FIR emitters (blue contours). Then, we fit the points in the $\mathcal{IRX}$-β plane for our calibration sample with a linear function. We derive the following best fit expression:

$$A_{\mathrm{UV}} = (1.76 \pm 0.04) + (0.20 \pm 0.02)\beta \qquad \text{(B1)}$$

Again, following the approach by Domínguez Sánchez et al. (2016), we apply the Meurer et al. 1999 $\mathcal{IRX}$-β relation

(A_{1600}=4.43 + 1.99β) for β values lower than the point in which our fit intercepts the relation by Meurer et al. (1999), β=-1.7, and Equation B1 for higher β values.

To assess the efficiency of our calibration, we quantify the scatter of the difference between the $\mathcal{SFR}_{\mathrm{TOT}}$ derived as the addition of $\mathcal{SFR}_{\mathrm{TIR}}$ and $\mathcal{SFR}_{\mathrm{UV}}$, and the $\mathcal{SFR}_{\mathrm{TOT}}$ computed as the $\mathcal{SFR}_{\mathrm{UV}}$ corrected for dust extinction for our calibration sample (right panel in Figure 1). The values vary between -0.38 and 0.26 dex with a median of -0.02 dex. Using the calibration by Meurer et al. (1999) instead would have lead to a median absolute deviation of 0.53 dex. Given that we use the calibration built on field galaxies to correct also the $\mathcal{SFR}_{\mathrm{UV}}$ of the cluster members not detected in the M/FIR, we compare how the calibration behaves for those faint M/FIR cluster members ($\mathcal{SFR}_{\mathrm{TIR}}<10 M_\odot\mathrm{yr}^{-1}$). In the right panel of Figure 1, we see that the dust extinction correction behaves similarly in the field and the clusters. For the latter, the median absolute deviation is -0.05 dex, and the differences vary between -0.54 and 0.23 dex.

APPENDIX C: CATALOGUES

This appendix details the entries of the catalogues released.

This paper has been typeset from a TeX/LaTeX file prepared by the author.

Table C1. Multiwavelength photometry

Entry name	Description
object	ID of the source in the parent catalogue. This ID is not the CLASH catalogue ID.
flux	[μJy]
err_flux	[μJy]

Table C2. Flags for the MIPS counterpart identification.

Entry name	Description
object	ID of the source in the parent catalogue.
MIPS_n_counterparts	Total number of (selection band) counterparts candidates for the MIPS24 source.
MIPS_ID_order	ID of the MIPS24 counterpart flagged with the likelihood.
	The most probable counterpart is flagged with a '_1'.
MIPS_order	The order of likelihood of being the right counterpart of the MIPS source.
MIPS_discriminator	Quantity used to determine the counterpart likelihood order.
MIPS_fMIPS24	MIPS24 flux [μJy] used for the MIPS24 counterpart identification.
MIPS_err_fMIPS24	MIPS24 flux error [μJy] used for the MIPS24 counterpart identification.
MIPS_fIRAC80	IRAC80 flux [μJy] used for the MIPS24 counterpart identification.
MIPS_err_fIRAC80	IRAC80 flux error [μJy] used for the MIPS24 counterpart identification.
MIPS_fIRAC36	IRAC36 flux [μJy] used for the MIPS24 counterpart identification.
MIPS_err_fIRAC36	IRAC36 flux error [μJy] used for the MIPS24 counterpart identification.
MIPS_distance	Distance between the MIPS24 source and the counterpart candidate.
MIPS24_snr_cuts	Flag regarding the SNR cuts applied in MIPS24:
	0 no-flux, 1 flux > SNR limit, -1 flux < SNR limit.
n_MIPS24_psf0.25/0.5/1/2	Number of sources in the parent catalogue.
n_MIPS24_wcs0.25/0.5/1/2	Number of sources in the parent catalogue.
n_MIPS_MIPS24_psf0.25/0.5/1/2	Number of MIPS sources within the MIPS24 PSF.
n_MIPS_MIPS24_wcs0.25/0.5/1/2	Number of MIPS sources within the MIPS24 WCS accuracy.
n_IRAC_MIPS24_psf0.25/0.5/1/2	Number of IRAC sources within the MIPS24 PSF.
n_IRAC_MIPS24_wcs0.25/0.5/1/2	Number of IRAC sources within the MIPS24 WCS accuracy.

Table C3. Flags for the PACS counterpart identification.

Entry name	Description
object	ID of the source in the parent catalogue.
PACS_ID_order	ID of the PACS counterpart flagged with the likelihood.
	The most probable counterpart is flaged with a '_1'.
PACS_discriminator	Quantity used to determine the counterpart likelihood order.
PACS_fPACS160	PACS160 flux [μJy] used for the PACS counterpart identification.
PACS_err_fPACS160	PACS160 flux error [μJy] used for the PACS counterpart identification.
PACS_fPACS100	PACS100 flux [μJy] used for the PACS counterpart identification.
PACS_err_fPACS100	PACS100 flux error [μJy] used for the PACS counterpart identification.
PACS_fMIPS24	MIPS24 flux [μJy] used for the PACS counterpart identification.
PACS_err_fMIPS24	MIPS24 flux error [μJy] used for the PACS counterpart identification.
PACS_fIRAC80	IRAC80 flux [μJy] used for the PACS counterpart identification.
PACS_err_fIRAC80	IRAC80 flux error [μJy] used for the PACS counterpart identification.
PACS_fIRAC36	IRAC36 flux [μJy] used for the PACS counterpart identification.
PACS_err_fIRAC36	IRAC36 flux error [μJy] used for the PACS counterpart identification.
PACS_distance	Distance between the PACS and the counterpart candidate.
PACS_order	The order of likelihood of being the right counterpart of the PACS source.
PACS_n_counterparts	Total number of counterparts candidates for the PACS source.
PACS100_snr_cuts	Flag regarding the SNR cuts applied in PACS100:
	0 no-flux, 1 flux > SNR limit, -1 flux < SNR limit.
PACS160_snr_cuts	Flag regarding the SNR cuts applied in PACS160:
	0 no-flux, 1 flux > SNR limit, -1 flux < SNR limit.
n_PACS100_psf0.25/0.5/1/2	Number of sources in the parent catalogue within the PACS100 PSF.
n_PACS160_psf0.25/0.5/1/2	Number of sources in the parent catalogue within the PACS160 PSF.
n_PACS100_wcs0.25/0.5/1/2	Number of sources in the parent catalogue within the PACS100 WCS accuracy.
n_PACS160_wcs0.25/0.5/1/2	Number of sources in the parent catalogue within the PACS160 WCS accuracy.
n_PACS_PACS100_psf0.25/0.5/1/2	Number of PACS sources within the PACS100 PSF.
n_PACS_PACS160_psf0.25/0.5/1/2	Number of PACS sources within the PACS160 PSF.
n_PACS_PACS100_wcs0.25/0.5/1/2	Number of PACS sources within the PACS100 WCS accuracy.
n_PACS_PACS160_wcs0.25/0.5/1/2	Number of PACS sources within the PACS160 WCS accuracy.
n_MIPS_PACS100_psf0.25/0.5/1/2	Number of MIPS sources within the PACS100 PSF.
n_MIPS_PACS160_psf0.25/0.5/1/2	Number of MIPS sources within the PACS160 PSF.
n_MIPS_PACS100_wcs0.25/0.5/1/2	Number of MIPS sources within the PACS100 WCS accuracy.
n_MIPS_PACS160_wcs0.25/0.5/1/2	Number of MIPS sources within the PACS160 WCS accuracy.
n_IRAC_PACS100_psf0.25/0.5/1/2	Number of IRAC sources within the PACS100 PSF.
n_IRAC_PACS160_psf0.25/0.5/1/2	Number of IRAC sources within the PACS160 PSF.
n_IRAC_PACS100_wcs0.25/0.5/1/2	Number of IRAC sources within the PACS100 WCS accuracy.
n_IRAC_PACS160_wcs0.25/0.5/1/2	Number of IRAC sources within the PACS160 WCS accuracy.

Table C4. Flags for the SPIRE counterpart identification.

Entry name	Description
object	ID of the source in the parent catalogue.
SPIRE_ID_order	ID of the SPIRE counterpart flagged with the likelihood.
	The most probable counterpart is flaged with a '_1'.
SPIRE_discriminator	Quantity used to determine the counterpart likelihood order.
SPIRE_fSPIRE500	SPIRE500 flux [μJy] used for the SPIRE counterpart identification.
SPIRE_err_fSPIRE500	SPIRE500 flux error [μJy] used for the SPIRE counterpart identification.
SPIRE_fSPIRE350	SPIRE350 flux [μJy] used for the SPIRE counterpart identification.
SPIRE_err_fSPIRE350	SPIRE350 flux error [μJy] used for the SPIRE counterpart identification.
SPIRE_fSPIRE250	SPIRE250 flux [μJy] used for the SPIRE counterpart identification.
SPIRE_err_fSPIRE250	SPIRE250 flux error [μJy] used for the SPIRE counterpart identification.
SPIRE_fPACS160	PACS160 flux [μJy] used for the SPIRE counterpart identification.
SPIRE_err_fPACS160	PACS160 flux error [μJy] used for the SPIRE counterpart identification.
SPIRE_fPACS100	PACS100 flux [μJy] used for the SPIRE counterpart identification.
SPIRE_err_fPACS100	PACS100 flux error [μJy] used for the SPIRE counterpart identification.
SPIRE_fMIPS24	MIPS24 flux [μJy] used for the SPIRE counterpart identification.
SPIRE_err_fMIPS24	MIPS24 flux error [μJy] used for the SPIRE counterpart identification.
SPIRE_fIRAC80	IRAC80 flux [μJy] used for the SPIRE counterpart identification.
SPIRE_err_fIRAC80	IRAC80 flux error [μJy] used for the SPIRE counterpart identification.
SPIRE_fIRAC36	IRAC36 flux [μJy] used for the SPIRE counterpart identification.
SPIRE_err_fIRAC36	IRAC36 flux error [μJy] used for the SPIRE counterpart identification.
SPIRE_distance	Distance between the SPIRE and the counterpart candidate.
SPIRE_order	The order of likelihood of being the right counterpart of the SPIRE source.
SPIRE_n_counterparts	Total number of counterparts candidates for the SPIRE source.
SPIRE250_snr_cuts	Flag regarding the SNR cuts applied in SPIRE250:
	0 no-flux, 1 flux > SNR limit, -1 flux < SNR limit.
SPIRE350_snr_cuts	Flag regarding the SNR cuts applied in SPIRE350:
	0 no-flux, 1 flux > SNR limit, -1 flux < SNR limit.
SPIRE500_snr_cuts	Flag regarding the SNR cuts applied in SPIRE500:
	0 no-flux, 1 flux > SNR limit, -1 flux < SNR limit.
n_SPIRE250_psf0.25/0.5/1/2	Number of sources in the parent catalogue within the SPIRE250 PSF.
n_SPIRE350_psf0.25/0.5/1/2	Number of sources in the parent catalogue within the SPIRE350 PSF.
n_SPIRE500_psf0.25/0.5/1/2	Number of sources in the parent catalogue within the SPIRE500 PSF.
n_SPIRE250_wcs0.25/0.5/1/2	Number of sources in the parent catalogue within the SPIRE250 WCS accuracy.
n_SPIRE350_wcs0.25/0.5/1/2	Number of sources in the parent catalogue within the SPIRE350 WCS accuracy.
n_SPIRE500_wcs0.25/0.5/1/2	Number of sources in the parent catalogue within the SPIRE500 WCS accuracy.
n_SPIRE_SPIRE250_psf0.25/0.5/1/2	Number of SPIRE sources within the SPIRE250 PSF.
n_SPIRE_SPIRE350_psf0.25/0.5/1/2	Number of SPIRE sources within the SPIRE350 PSF.
n_SPIRE_SPIRE500_psf0.25/0.5/1/2	Number of SPIRE sources within the SPIRE500 PSF.
n_SPIRE_SPIRE250_wcs0.25/0.5/1/2	Number of SPIRE sources within the SPIRE250 WCS accuracy.
n_SPIRE_SPIRE350_wcs0.25/0.5/1/2	Number of SPIRE sources within the SPIRE350 WCS accuracy.
n_SPIRE_SPIRE500_wcs0.25/0.5/1/2	Number of SPIRE sources within the SPIRE500 WCS accuracy.
n_PACS_SPIRE250_psf0.25/0.5/1/2	Number of PACS sources within the SPIRE250 PSF.
n_PACS_SPIRE350_psf0.25/0.5/1/2	Number of PACS sources within the SPIRE350 PSF.
n_PACS_SPIRE500_psf0.25/0.5/1/2	Number of PACS sources within the SPIRE500 PSF.
n_PACS_SPIRE250_wcs0.25/0.5/1/2	Number of PACS sources within the SPIRE250 WCS accuracy.
n_PACS_SPIRE350_wcs0.25/0.5/1/2	Number of PACS sources within the SPIRE350 WCS accuracy.
n_PACS_SPIRE500_wcs0.25/0.5/1/2	Number of PACS sources within the SPIRE500 WCS accuracy.
n_MIPS_SPIRE250_psf0.25/0.5/1/2	Number of MIPS sources within the SPIRE250 PSF.
n_MIPS_SPIRE350_psf0.25/0.5/1/2	Number of MIPS sources within the SPIRE350 PSF.
n_MIPS_SPIRE500_psf0.25/0.5/1/2	Number of MIPS sources within the SPIRE500 PSF.
n_MIPS_SPIRE250_wcs0.25/0.5/1/2	Number of MIPS sources within the SPIRE250 WCS accuracy.
n_MIPS_SPIRE350_wcs0.25/0.5/1/2	Number of MIPS sources within the SPIRE350 WCS accuracy.
n_MIPS_SPIRE500_wcs0.25/0.5/1/2	Number of MIPS sources within the SPIRE500 WCS accuracy.
n_IRAC_SPIRE250_psf0.25/0.5/1/2	Number of IRAC sources within the SPIRE250 PSF.
n_IRAC_SPIRE350_psf0.25/0.5/1/2	Number of IRAC sources within the SPIRE350 PSF.
n_IRAC_SPIRE500_psf0.25/0.5/1/2	Number of IRAC sources within the SPIRE500 PSF.
n_IRAC_SPIRE250_wcs0.25/0.5/1/2	Number of IRAC sources within the SPIRE250 WCS accuracy.
n_IRAC_SPIRE350_wcs0.25/0.5/1/2	Number of IRAC sources within the SPIRE350 WCS accuracy.
n_IRAC_SPIRE500_wcs0.25/0.5/1/2	Number of IRAC sources within the SPIRE500 WCS accuracy.

Table C5. Redshift and properties

Entry name	Description
object	ID of the galaxy in the parent catalogue.
z_phot	EAZY z_{phot}.
z_spec	Spectroscopic redshift.
flag	Quality of the z_{spec}. Values >2 mean reliable.
stellar_mass	Stellar mass in $M_{\odot}$.
L_TIR	Total IR luminosity (8-1000μm) in $L_{\odot}$, from the best-fit template (Draine & Li 2007).
SFR_UV	Star formation rate $[M_{\odot}\mathrm{yr}^{-1}]$ from the rest-frame monochromatic luminosity at 2800 Å.
SFR_UV_corr	Star formation rate $[M_{\odot}\mathrm{yr}^{-1}]$ from the rest-frame monochromatic luminosity at 2800 Å. corrected by extinction using $\mathcal{A}_{\mathrm{UV}}=(1.76\pm0.04)+(0.20\pm0.02)\beta$.
SFR_TIR	Star formation rate $[M_{\odot}\mathrm{yr}^{-1}]$ from the L_TIR.
U	Rest-frame U absolute magnitude from best-fit template.
V	Rest-frame V absolute magnitude from best-fit template.
J	Rest-frame J absolute magnitude from best-fit template.